ABSTRACT

Title of Dissertation: WAVE GENERATION
AND ELECTRON SCATTERING
DURING MAGNETIC RECONNECTION

Hanqing Ma
Doctor of Philosophy, 2026

Dissertation Directed by: Professor James F. Drake
Department of Physics

Magnetic reconnection is a fundamental process in space and astrophysical plasmas that releases magnetic energy and produces energetic particles. The resulting nonthermal electrons and anisotropic distributions provide free energy for kinetic instabilities, which generate magnetic structures and plasma waves that can significantly influence particle dynamics and transport. This dissertation employs particle-in-cell (PIC) simulations to investigate how reconnection-driven kinetic processes generate magnetic structures and waves, and how these self-generated fluctuations regulate energetic electron scattering and transport.

First, two-dimensional PIC simulations with a realistic mass ratio are used to investigate the origin of out-of-plane magnetic fields in magnetic islands (flux ropes) formed during reconnection. Without an initial guide field, reconnection generates a large electron temperature anisotropy inside magnetic islands that drives the Weibel instability, producing strong bipolar out-of-plane magnetic fields with amplitudes reaching $B_z/B_0 \sim 0.4$ with B_0 the amplitude of the reconnecting magnetic

field. The instability relaxes the anisotropy after which island merging regenerates the free energy and re-excites the instability. With a strong guide field ($B_g/B_0 = 0.5$), electron outflows are redirected along separatrices and form a circular current loop around flux ropes. This current enhances the guide field to $B_z/B_0 \sim 1.4$ and can drive the electron Kelvin–Helmholtz instability, further amplifying the magnetic field. These self-generated core fields scatter electrons, reduce temperature anisotropy, and may influence Fermi acceleration during reconnection. The results are consistent with spacecraft observations of enhanced magnetic fields within flux ropes in the magnetotail and solar wind.

Second, PIC simulations are performed to investigate the scattering of electron heat flux by self-generated oblique whistler waves in the context of solar flares. Multiple observations suggest the inhibition of energetic-electron transport and even the confinement of electrons in the flaring region. In the simulations, an initial distribution representing a reconnection-driven electron heat flux excites strong oblique whistler waves together with filamentary Weibel-like structures. These instabilities efficiently scatter electrons, suppress heat flux, and drive the electron distribution toward isotropy. Electron trajectories show that particles with initially large parallel velocities can be scattered to negative parallel velocities. The key parameter is the ratio of the heat-flux drift speed to the electron Alfvén speed, with larger drift speeds producing stronger waves and more effective heat flux suppression. A scaling relation between the scattering rate and drift speed is also derived.

Finally, the role of the 90° pitch-angle scattering barrier is investigated. In quasilinear theory, the pitch-angle diffusion coefficient vanishes at 90°, preventing electrons from being scattered across this boundary. As a result, an electron heat flux evolves into a nearly uniform distribution over pitch angles $0 < \theta < 90^\circ$, while remaining unable to diffuse into the negative parallel-velocity region. Simulations show that this highly anisotropic distribution contains substantial free energy that drives the growth of large-amplitude oblique whistler waves. These waves strongly scatter electrons near

90° pitch angle, enabling a significant fraction of particles to cross the barrier and diffuse to negative parallel velocities. Consequently, the electron distribution evolves toward an approximately isotropic state. These findings provide new insight into the regulation of energetic-electron transport and heat flux in the solar corona, solar wind, and intracluster medium of galaxy clusters.

WAVE GENERATION AND ELECTRON SCATTERING DURING MAGNETIC RECONNECTION

by

Hanqing Ma

Dissertation submitted to the Faculty of the Graduate School of the
University of Maryland, College Park in partial fulfillment
of the requirements for the degree of
Doctor of Philosophy
2026

Advisory Committee:
Professor James Drake, Chair/Advisor
Professor Thomas Antonsen
Professor Christopher Reynolds
Dr. Marc Swisdak
Dr. Matt Landreman

© Copyright by
Hanqing Ma
2026

Acknowledgments

I feel very fortunate to have had Professor James Drake as my advisor. Over the past five years, we have worked together extremely well. Our meetings and conversations were always efficient and fruitful, and his deep insight into physics and consistently high scientific standards have profoundly supported my progress throughout my Ph.D. Whenever my research encountered obstacles, he was always able to offer new ideas and directions. He also provided many opportunities in academia, which greatly broadened my academic experience. I especially appreciate the trust he placed in me and the flexibility he gave me in arranging my time, both of which are rare and valuable. My Ph.D. journey has gone much more smoothly because of his guidance, and I would like to express once again my deepest gratitude to my advisor, Professor James Drake.

I am also sincerely grateful to my co-advisor, Dr. Marc Swisdak. He continuously helped me solve coding and technical problems throughout my research. He has always been patient, insightful, and friendly. Without his support, I could not have completed my research so smoothly.

I would like to thank my colleague and friend, Zhiyu Yin. We maintained a close friendship throughout my Ph.D. journey. He gave me a great deal of help outside of research, and without him my life during graduate school would have been much less enjoyable.

I would also like to thank my colleagues and friends, Anna Fitzmaurice, Gareth Roberg-Clark, Meriem Alaoui Abdallaoui, and Haotian Da, for many helpful discussions. Their companionship and support made both research and daily life more enjoyable. I am grateful to the National Science Foundation and the National Energy Research Scientific Computing Center (NERSC) for their support. This dissertation would not have been possible without them. I would also like to thank the University of Maryland and the Department of Physics for providing a supportive academic environment. The beautiful campus and the friendly and efficient staff members made my graduate experience much

more pleasant.

Most importantly, I would like to thank my parents for their unconditional love and support. They have always believed in me and encouraged me through every challenge. Without their love and constant support, this work would not have been possible.

Table of Contents

Acknowledgments ii

Table of Contents iv

List of Figures vi

Chapter 1: Introduction 1
- 1.1 Magnetic Reconnection . . . 1
  - 1.1.1 Basic Principles . . . 1
  - 1.1.2 Particle Acceleration . . . 4
  - 1.1.3 Reconnection in the Solar Corona and the Magnetosphere . . . 6
- 1.2 The Origin of Strong Core Fields in Flux Ropes in the Magnetosphere . . . 8
  - 1.2.1 Observational Evidence . . . 8
  - 1.2.2 Previous Explanations . . . 9
  - 1.2.3 The Weibel and Electron Kelvin–Helmholtz Instability . . . 10
- 1.3 Inhibition of Energetic Electron Transport in the Solar Corona . . . 13
  - 1.3.1 Observational Evidence . . . 13
  - 1.3.2 Alternative Explanations . . . 16
  - 1.3.3 The Wave–Particle Interaction and Whistler Instability . . . 19
- 1.4 Whistler-Wave Scattering of Energetic Electrons . . . 20
  - 1.4.1 Basic Principles . . . 20
  - 1.4.2 Resonant Interactions . . . 21
  - 1.4.3 The 90 Degree Problem . . . 25
- 1.5 Numerical Method: Particle-in-Cell Simulations . . . 26
  - 1.5.1 Basic Principles . . . 26
  - 1.5.2 Comparison with MHD Simulations . . . 29
- 1.6 Outline of the Thesis . . . 30

Chapter 2: Self-Generation of Core Fields and Electron Scattering in Flux Ropes 31
- 2.1 Background . . . 31
- 2.2 Simulation Setup . . . 32
- 2.3 Simulation Results . . . 33
  - 2.3.1 Zero-Guide-Field Case . . . 33
  - 2.3.2 Strong-Guide-Field Case . . . 38
- 2.4 Discussion and Conclusions . . . 46

Chapter 3: Wave Generation and Energetic Electron Scattering in Solar Flares 50
- 3.1 Background . . . 50
- 3.2 Simulation Setup . . . 51
  - 3.2.1 Initial Distribution . . . 51
  - 3.2.2 Boundary Condition . . . 53

3.3 Simulation Results . . . 54
3.3.1 Wave Excitation . . . 54
3.3.2 Whistler Wave Scattering . . . 58
3.3.3 Reduced Number Density Case . . . 62
3.3.4 Scattering Rate . . . 64
3.4 Discussion and Conclusions . . . 66

Chapter 4: Whistler-Wave Scattering of Energetic Electrons Past 90 Degrees 69
4.1 Background . . . 69
4.2 Simulation Setup . . . 69
4.3 Simulation Results . . . 72
4.3.1 Wave Excitation . . . 72
4.3.2 Electron Scattering Past 90 Degrees . . . 75
4.4 Discussion and Conclusions . . . 77

Chapter 5: Summary and Outlook 80
5.1 Summary of the Main Results . . . 80
5.2 Limitations of the Present Work . . . 82
5.3 Future Directions . . . 83

Bibliography 85

List of Figures

1.1 Schematic illustration of magnetic reconnection . . . 1
1.2 Schematic illustration of Earth's magnetosphere . . . 7
1.3 Observed flux rope with a strong core field . . . 9
1.4 Schematic illustration of the Weibel instability . . . 11
1.5 Schematic illustration of the Kelvin–Helmholtz instability . . . 12
1.6 Observed above-the-looptop hard X-ray source . . . 14
1.7 Schematic illustration of whistler-wave resonant scattering . . . 22
1.8 Cyclotron-resonant scattering of the solar-wind strahl . . . 24
1.9 Schematic illustration of a PIC simulation . . . 27

2.1 Magnetic-field structure in the lower current sheet . . . 33
2.2 Weibel magnetic-field structure and x-directed electron current distribution . . . 34
2.3 Space–time evolution of B_z and electron temperature anisotropy . . . 36
2.4 Evolution of the Weibel field during flux-rope merging . . . 37
2.5 Magnetic field structure in the lower current sheet with a guide field . . . 39
2.6 Electron bulk flows and magnetic field structure . . . 40
2.7 Schematic illustration of the flux-rope separatrix-current mechanism . . . 41
2.8 Space–time evolution of B_z and sheared electron flow . . . 43
2.9 Magnetic-field evolution during magnetic-island merging with a guide field . . . 44
2.10 Scatter plot of electron density versus B_z . . . 45

3.1 Evolution of magnetic-field fluctuations . . . 55
3.2 Magnetic-field structure and space–time evolution of B_z . . . 56
3.3 Power spectrum of B_z . . . 57
3.4 Spatial distribution of electron temperature anisotropy . . . 58
3.5 Final-to-initial ratio of the average y-directed heat flux . . . 59
3.6 Evolution of the electron distribution function . . . 60
3.7 Test electron trajectories . . . 61
3.8 Magnetic-field generation at reduced number density . . . 63
3.9 Evolution of magnetic field fluctuations for different number densities . . . 64
3.10 Average wave–electron scattering rate versus drift speed . . . 66

4.1 Initial electron velocity distribution function . . . 71
4.2 Evolution of magnetic field fluctuations . . . 72
4.3 Magnetic-field structure and space–time evolution of B_z . . . 73
4.4 Hodogram of the magnetic field components . . . 74
4.5 Evolution of the electron velocity distribution function . . . 75
4.6 Comparison of initial and final distributions in the upper and lower velocity planes . . . 77

Chapter 1: Introduction

1.1 Magnetic Reconnection

1.1.1 Basic Principles

Magnetic reconnection is a fundamental plasma process that plays a central role in a wide range of space and astrophysical environments, including the solar corona [1–5], the Earth's magnetosphere [6–10], and the solar wind [11–14]. Through reconnection, magnetic energy is efficiently converted into particle kinetic energy, thermal energy, and bulk flows, accompanied by topological changes of magnetic field lines [15–17].

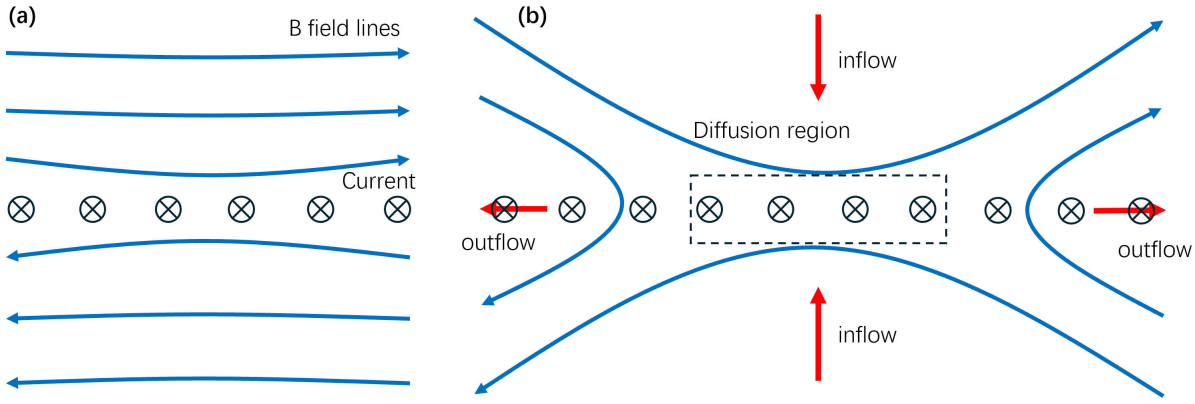


Figure 1.1: Schematic illustration of (a) a typical Harris-type current sheet and (b) the X-line during magnetic reconnection. The blue lines represent magnetic field lines and red arrows are plasma flows.

Figure 1.1 illustrates a typical two-dimensional picture of magnetic reconnection. Panel (a) shows a Harris-type current sheet configuration containing oppositely directed magnetic fields separated by a central thin current sheet [18]. In panel (b), magnetic field lines reconnect at the X-line within the elongated diffusion region as plasma from the upstream region flows inward and newly reconnected field lines are ejected outward by magnetic tension. Due to mass continuity in the elongated current

layer, the reconnection outflow velocity is much larger than the inflow velocity, with the typical outflow speed being on the order of $\sim v_A$ and the inflow speed being on the order of $\sim 0.1 v_A$, where v_A is the Alfvén speed [2, 19–21]. This process produces high-speed outflows together with substantial plasma heating and particle energization. This process, in which a thin current sheet breaks up into a chain of magnetic islands in response to small perturbations, is commonly referred to as the tearing instability, while the corresponding unstable perturbation is known as the tearing mode [22–25].

A key requirement for magnetic reconnection is the breakdown of the "frozen-in condition". In ideal magnetohydrodynamics (MHD), the electric field in the plasma frame satisfies

$$\mathbf{E} + \frac{1}{c}\mathbf{u} \times \mathbf{B} = 0, \tag{1.1}$$

so magnetic field lines are frozen into the plasma and move together with it [26–28]. Under this condition, the magnetic topology is preserved, and field lines cannot change their connectivity. For reconnection to proceed, the frozen-in condition must break down.

Within the diffusion region, additional terms in the generalized Ohm's law become important,

$$\mathbf{E} + \frac{\mathbf{u} \times \mathbf{B}}{c} = \eta \mathbf{J} + \frac{\mathbf{J} \times \mathbf{B}}{nec} - \frac{\nabla \cdot \mathbf{P}_e}{ne} + \frac{m_e}{ne^2}\left[\frac{\partial \mathbf{J}}{\partial t} + \nabla \cdot (\mathbf{u}\mathbf{J} + \mathbf{J}\mathbf{u}) - \frac{1}{ne}\nabla \cdot (\mathbf{J}\mathbf{J})\right]. \tag{1.2}$$

where the terms on the right-hand side represent, respectively, resistive diffusion, the Hall effect, the divergence of the electron pressure tensor, and electron inertial effects. While the Hall term enables ion–electron decoupling, resistive diffusion, electron inertial effects, and the off-diagonal components of the electron pressure tensor can break the frozen-in condition and allow changes in magnetic topology [19, 29–33].

Historically, the earliest theoretical descriptions of reconnection were developed in the resistive MHD framework. The famous Sweet–Parker model [1, 2] described reconnection in an elongated current sheet and established the basic relations between inflow, outflow, and dissipation. However, the reconnection rate predicted by this model is too slow to explain explosive energy release in solar flares and substorms, which became one of the central questions in reconnection research [34–36]. Petschek later proposed a faster reconnection model with standing slow shocks, which provided a possible explanation for rapid energy conversion [3].

Subsequent theoretical, numerical, and observational studies showed that collisionless effects, Hall physics, and kinetic processes play essential roles in enabling fast reconnection in many natural plasmas [19, 30–33]. At scales below the ion inertial length, the ion and electron motions decouple, and the dynamics is fundamentally altered by Hall physics and the associated whistler waves. Because whistler waves have dispersive properties that allow rapid transport of magnetic flux at small scales, the reconnection rate becomes largely insensitive to the specific electron-scale mechanism that breaks the frozen-in condition [19, 30, 33]. A particularly influential milestone in establishing this picture was the Geospace Environmental Modeling (GEM) Magnetic Reconnection Challenge [19], in which full particle, hybrid, Hall MHD, and resistive MHD simulations were compared under the same Harris-sheet configuration. A key result was that all models including the Hall effect produced similarly fast reconnection rates, whereas conventional resistive MHD yielded much slower reconnection unless an artificially enhanced localized resistivity was introduced. These results demonstrated that Hall physics, together with the underlying whistler dynamics, is a key ingredient in fast collisionless reconnection and established an important benchmark for the modern understanding of magnetic reconnection.

In this thesis, reconnection provides the larger physical context for several related problems. There are several comprehensive books and review articles on magnetic reconnection [34–36]. Given

the breadth of the subject, we summarize here only the concepts most relevant to this work.

1.1.2 Particle Acceleration

One of the central consequences of magnetic reconnection is efficient particle acceleration. Key questions in this aspect include: what are the dominant energization mechanisms, where in the reconnection region particles gain most of their energy, how the accelerated particle spectra are formed, and how wave–particle interactions and scattering regulate the transport and further energization of particles [17, 37–39].

In the guiding-center approximation, the main acceleration mechanisms are Fermi acceleration, betatron acceleration, and direct acceleration by a parallel electric field [15,17,40–42]. Fermi acceleration occurs when a particle encounters a dynamically evolving, curved magnetic field. Betatron acceleration describes the energization that results from an increasing magnetic field, which increases the perpendicular energy through conservation of the first adiabatic invariant. However, Fermi acceleration is found to be the dominant mechanism for electron energization in the weak-guide-field regime [15, 17, 40–42]. In this thesis, particular emphasis is placed on Fermi acceleration.

A key feature of reconnection-driven Fermi acceleration is that the energy gain primarily results from motion parallel to the magnetic field and scales as $dE/dt \propto v_{\parallel}^2$ [15, 16]. As a result, electron heating preferentially occurs in the parallel direction, naturally producing temperature anisotropy with $T_{\parallel} > T_{\perp}$.

The strong temperature anisotropy produced by Fermi acceleration can drive kinetic instabilities and, in turn, modify the acceleration process itself. For example, when the pressure anisotropy satisfies

$$P_{\parallel} - P_{\perp} > \frac{B^2}{4\pi}. \tag{1.3}$$

the plasma may become unstable to the firehose instability [43–46]. In this instability, the parallel pressure exceeds the perpendicular pressure by an amount sufficient to overcome magnetic tension, causing magnetic field lines to become unstable and develop kink-like or wave-like deformations. The onset of the firehose instability can reduce the efficiency of Fermi acceleration and thereby limit continued particle energization. This is because the pressure anisotropy reduces the effective magnetic tension force that drives field-line contraction, weakening the Fermi acceleration process [43–46].

Power-law energy spectra are a hallmark of nonthermal acceleration and are of great interest for reconnection studies. They can form when particles undergo repeated Fermi-type acceleration in contracting or merging magnetic structures while also experiencing escape from the main acceleration region [42, 47, 48]. If the acceleration is sufficiently efficient and can be sustained over a broad energy range, the resulting spectrum naturally develops a power-law form. In three-dimensional reconnection, turbulence and chaotic magnetic field lines help particles access multiple acceleration sites, which is important for maintaining such spectra [42, 48].

In practice, accelerated particle distributions are often well described by kappa distributions that extend over a broad energy range [16, 17, 49, 50]. The kappa distribution is especially useful because it approaches a Maxwellian form in the thermal part of the distribution, while exhibiting a power-law-like high-energy tail in the nonthermal regime, which is consistent with flare observations [51–55]. These results indicate that reconnection-accelerated electrons are both strongly nonthermal and highly anisotropic, making wave generation and electron scattering key processes that can regulate their transport.

1.1.3 Reconnection in the Solar Corona and the Magnetosphere

The solar corona and Earth's magnetosphere are two of the most important natural laboratories for investigating magnetic reconnection. The problems studied in this thesis are closely related to magnetic reconnection in both of these environments, so a brief introduction to each is warranted.

Coronal plasmas are typically hot, tenuous, and strongly magnetized, with characteristic temperatures of 10^6–10^7 K, densities of 10^8–$10^{10}\,\mathrm{cm}^{-3}$, magnetic field strengths ranging from a few to several hundred gauss in active regions, and Alfvén speeds on the order of $10^3\,\mathrm{km\,s}^{-1}$. The plasma beta, defined as the ratio of plasma pressure to magnetic pressure, is typically much smaller than unity, with values ranging from 10^{-3} to 10^{-1}. In the solar corona, magnetic reconnection is involved in solar flares, coronal mass ejections, and coronal jets, and is widely regarded as the mechanism responsible for explosive energy release. [1–5, 56–59].

The direct sampling of coronal plasma is currently not possible. Even the Parker Solar Probe (PSP), the closest spacecraft ever to the Sun, only reaches $\sim 10\,R_\odot$ (solar radius) from the solar surface [60]. Therefore, magnetic reconnection in the solar corona is studied primarily through remote sensing observations, including extreme ultraviolet (EUV) and X-ray imaging, spectroscopic measurements, white-light coronagraph observations, and radio diagnostics (e.g., [56,57,61,62]). Since direct measurements of the coronal magnetic field are difficult, the coronal magnetic topology is often inferred through magnetic field extrapolation techniques based on photospheric magnetograms, such as potential-field and nonlinear force-free field reconstructions (e.g., [63–68]). In summary, solar observations provide rich information on the large-scale evolution of reconnection, but the underlying microphysical processes must often be inferred indirectly.

Figure 1.2 illustrates the structure of Earth's magnetosphere and its interaction with the solar

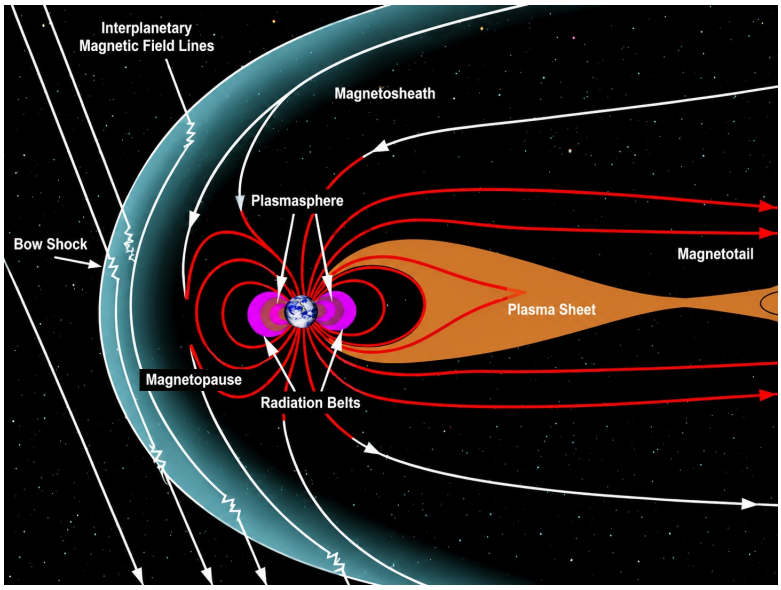


Figure 1.2: Schematic illustration of Earth's magnetosphere and its interaction with the solar wind, showing the bow shock, magnetopause, and magnetotail structures.

wind. Magnetic reconnection can occur both at the dayside magnetopause and within the magnetotail plasma sheet, where reconnection plays a central role in solar wind–magnetosphere coupling and particle acceleration [6–10]. Typical parameters in the magnetotail plasma sheet include densities of $\sim$ 0.01–1 cm^{-3}, ion temperatures of $\sim$ 1–10 keV, magnetic field strengths of $\sim$ 10–30 nT, and Alfvén speeds up to 1000 $\mathrm{km\,s}^{-1}$. The plasma beta is typically of order 10^{-1}. In contrast to the solar corona, the near-Earth magnetosphere can be probed directly by spacecraft, allowing in situ measurements of fields, wave activity and particle distributions. Over the past several decades, many probes and satellites, such as ISEE, Geotail, Cluster, THEMIS, and the Magnetospheric Multiscale (MMS) mission, have been launched to investigate Earth's magnetosphere.

1.2 The Origin of Strong Core Fields in Flux Ropes in the Magnetosphere

1.2.1 Observational Evidence

Magnetic islands and flux ropes are common structures produced during magnetic reconnection [40,69–73]. In two-dimensional configurations, reconnection often generates closed magnetic structures known as magnetic islands, which can move, contract and merge. In three dimensions, the corresponding structures are generally referred to as flux ropes, which consist of twisted magnetic field lines wrapped around a central axis. These structures play an essential role in particle acceleration during reconnection [16, 37, 39, 40, 47].

Observations frequently report strong out-of-plane magnetic fields in the center of magnetic islands during reconnection events, often accompanied by enhanced fluxes of energetic electrons [69, 72–82]. In the following context, the term "core magnetic field" refers specifically to the out-of-plane magnetic field. These magnetic structures are typically identified by their bipolar in-plane magnetic field together with an enhanced axial, or core, magnetic field near their centers.

On the other hand, flux ropes or plasmoids are also widely observed in many eruptive solar phenomena. They have been seen rising above flare loops, often preceding the onset of CMEs [58, 83–86]. Similar structures have also been detected propagating along bright white-light rays trailing CMEs [87, 88] or above helmet streamers [89]. In addition, plasmoids are commonly observed in coronal jets [90–92], and have been identified through subarcsecond imaging spectroscopy in UV bursts in the lower solar atmosphere [93]. More recently, enhanced core fields have been documented during island merger at the heliospheric current sheet close to the sun [94].

Because the direct measurement of the core fields in flux ropes in remote environments is not

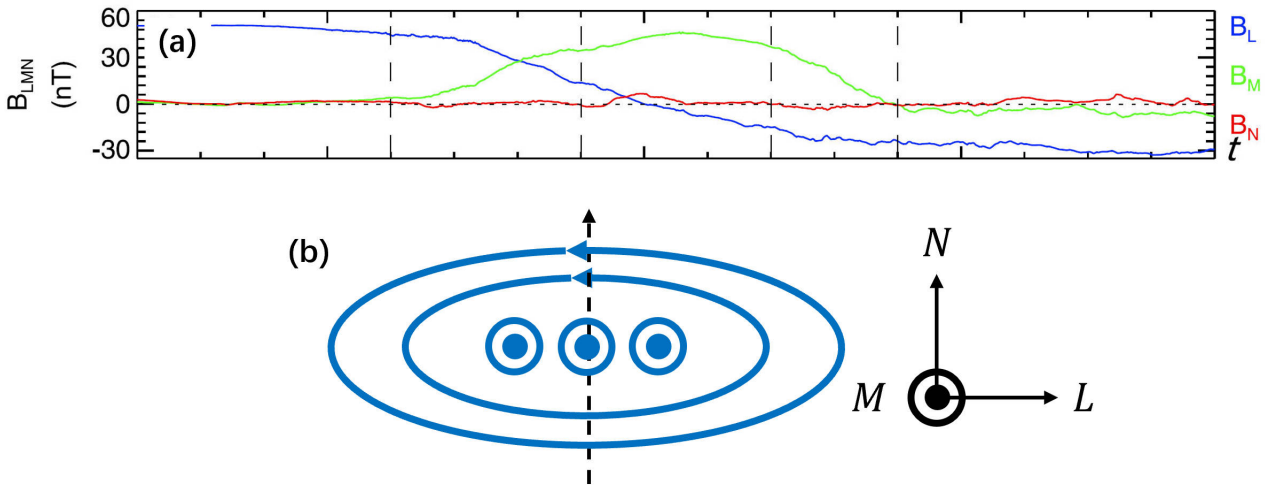


Figure 1.3: (a) Example of an observed flux rope, adapted from [82], showing the characteristic bipolar signature in B_L and an enhanced core magnetic field B_M near its center. (b) Schematic illustration of the flux rope geometry. The blue arrows represent magnetic field lines within the magnetic island, while the dashed black arrow indicates the observer.

feasible, establishing the generation mechanisms for enhanced core fields in flux ropes where *in situ* measurements are possible is essential. Understanding how these strong core fields are generated is important for interpreting both the magnetic structure and the particle dynamics of reconnecting plasmas.

1.2.2 Previous Explanations

The physical origin of the strong core fields in flux ropes remains an open question. In early studies, Scholer interpreted enhanced core fields in the framework of a bursty reconnection model [95–97], while Karimabadi carried out hybrid reconnection simulations and attributed the large core fields to Hall-generated currents [98].

In the past, the formation of a core field inside magnetic islands has often been attributed to the compression of the initial guide field during island contraction and merging associated with the loss of

internal plasma [70, 99–102]. In this interpretation, reconnection produces closed magnetic structures that trap an initial out-of-plane magnetic flux. As the island contracts, this flux is concentrated into a smaller cross section, leading to an increase in the core magnetic field. The amplification can be further enhanced if plasma is lost from the island interior by motion parallel to the axis of a finite length flux rope. The associated reduction in thermal pressure allows additional compression of the structure.

1.2.3 The Weibel and Electron Kelvin–Helmholtz Instability

1.2.3.1 The Weibel Instability

The Weibel instability, first identified by Weibel [103] and also referred to as the filamentation instability, is an electromagnetic instability driven by velocity-space anisotropy. In the Weibel instability, the unstable mode is typically non-oscillatory ($\omega \sim 0$), with a wave vector predominantly perpendicular to the direction of the temperature anisotropy. Although the instability can be derived rigorously from kinetic theory, a simple physical picture of its mechanism is illustrated in Figure 1.4. In panel (a), the electron distribution has a higher temperature in the horizontal direction, corresponding to an anisotropic velocity distribution. Small sinusoidal magnetic field perturbations deflect electrons and lead to the formation of spatially separated current filaments, as shown in panel (b). These current filaments generate magnetic fields that further enhance the original perturbations, resulting in the growth of the filamentary magnetic fields.

Since its discovery, the Weibel instability has been studied extensively through theoretical analysis, numerical simulations, and laboratory experiments with applications to astrophysical systems (e.g., [104–109]). By converting the free energy stored in velocity-space anisotropy into magnetic fluctuations,

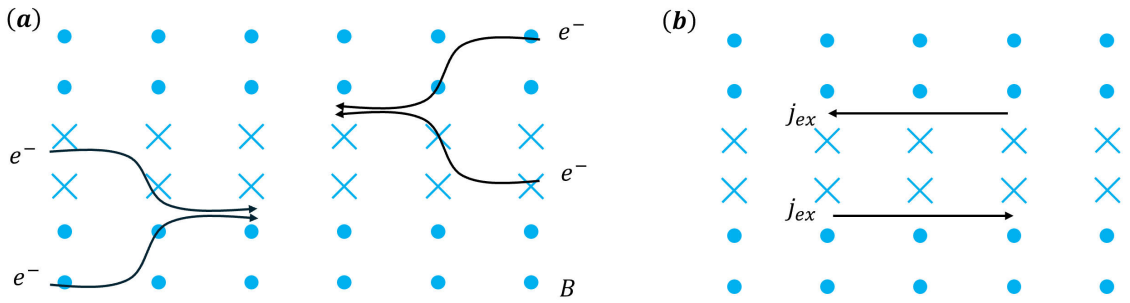


Figure 1.4: Schematic illustration of the Weibel instability driven by an anisotropic velocity distribution. (a) Small magnetic field perturbations deflect electrons into spatially separated current filaments. (b) These current filaments generate magnetic fields that reinforce the original perturbations, leading to the growth of the instability.

the Weibel instability is widely regarded as an important mechanism for magnetic-field generation in space and astrophysical plasmas [110]. It has also been proposed as a possible mechanism for suppressing heat transport [111, 112].

In the context of magnetic reconnection, the Weibel instability is naturally expected to arise because reconnection efficiently accelerates electrons and produces strong temperature anisotropies. Particle-in-cell simulations have demonstrated that reconnection outflows naturally develop strong electron temperature anisotropies that can excite the Weibel instability [113]. However, it has also been suggested that even a weak guide field ($\sim 0.1\,B_0$) could suppress the instability [113]. Alternative mechanisms for Weibel-induced magnetic-field generation associated with electron inflow into the current sheet have been proposed [114]. In addition, studies of electron–positron (pair) reconnection have shown that the Weibel instability can grow robustly and help to maintain fast reconnection by broadening the current layer [115, 116]. Together, these results demonstrate that the Weibel instability can be a crucial element of current-layer dynamics in magnetic reconnection, although its effectiveness and dominance may depend sensitively on plasma conditions such as the guide-field strength.

1.2.3.2 The Electron Kelvin–Helmholtz Instability

The Kelvin–Helmholtz instability (KHI) is a shear-flow-driven instability that develops at the interface between two fluids or plasmas with different flow velocities. A small perturbation of the interface can extract energy from the velocity shear and grow into rolled-up vortex structures, as shown in Figure 1.5.

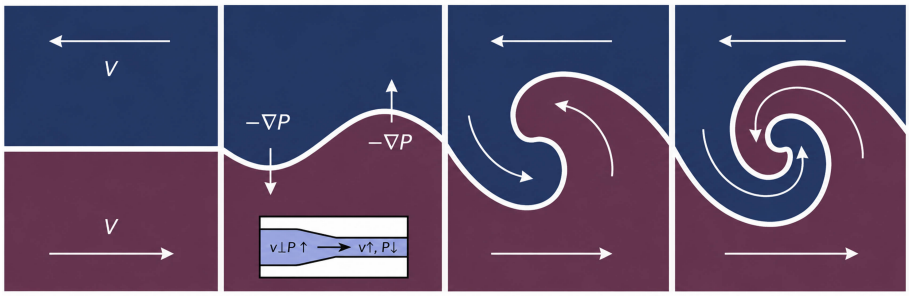


Figure 1.5: Schematic illustration of the Kelvin–Helmholtz instability. Owing to a Bernoulli-like effect, the pressure decreases at the crest and increases at the trough of the perturbed interface, causing the perturbations to grow and the interface to roll up into vortices.

In ordinary fluids, this process is commonly associated with waves and vortices at shear layers. In plasmas, however, the instability is modified by magnetic fields, compressibility, and kinetic effects. In particular, a magnetic field component parallel to the flow tends to suppress the instability [117, 118]. The KHI is therefore especially important at plasma boundaries where strong velocity shear coexists with magnetic and density gradients, such as planetary magnetopauses, the solar wind, the solar corona, and astrophysical jets [23, 118, 119].

The electron Kelvin–Helmholtz instability (EKHI) is a shear-flow-driven instability that develops when strong velocity gradients arise in electron flows. In collisionless plasmas, electron-scale shear layers or narrow electron jets formed over kinetic length scales can become unstable to the EKHI, generating vortex-like structures, localized electric and magnetic field fluctuations, and turbulence. In

magnetic reconnection, such strong electron shear flows commonly develop in the outflow region and along separatrix or current-layer boundaries, making reconnecting plasmas particularly susceptible to the EKHI [120, 121]. Simulations have shown that the instability can distort current layers, generate multiple vortices, enhance turbulence, and even trigger secondary magnetic reconnection [120–122]. These effects demonstrate that the EKHI may play an important role in restructuring the current layer and modifying electron transport in reconnecting plasmas.

1.3 Inhibition of Energetic Electron Transport in the Solar Corona

1.3.1 Observational Evidence

1.3.1.1 Looptop Hard X-ray Sources

The hard X-rays observed during solar flares are generally believed to be produced by the bremsstrahlung radiation from very energetic electrons [123–125]. After being accelerated to nonthermal energies during magnetic reconnection, these electrons propagate along magnetic field lines and interact with denser plasma in the lower corona or chromosphere, where they are decelerated by Coulomb collisions with ions and emit hard X-rays in the process. The soft X-rays are produced through a similar bremsstrahlung mechanism, but originate primarily from thermal electrons in hot flare plasma. In general, hard X-rays are associated with electrons of energies $\sim$ 20–100 keV, whereas soft X-rays typically correspond to energies of $\sim$ 1–10 keV.

In addition to the footpoint hard X-ray sources located in the lower corona, observations have commonly revealed the existence of looptop hard X-ray sources, which are situated at or distinctly above the top of the soft X-ray flaring loops [57, 126–129]. An example of such observations is shown

in Figure 1.6. Increased detection sensitivity indicates that the above-the-looptop hard X-ray emission is likely a common feature of all flares [130].

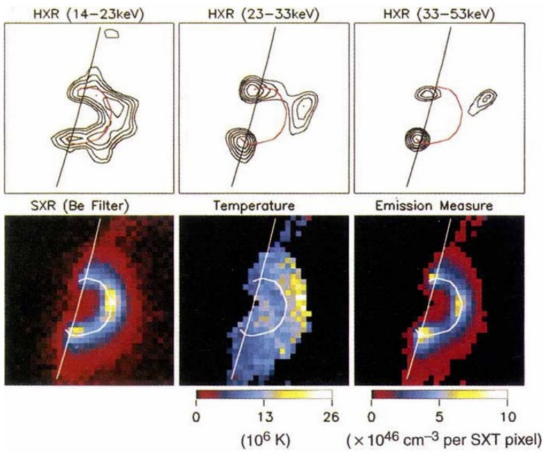


Figure 1.6: Example of Hard X-ray (top row) and soft X-ray (bottom row) images of the flare. Adapted from [57].

During solar flares, magnetic reconnection accelerates electrons to energies exceeding 100 keV, more than three orders of magnitude higher than the typical thermal energy of the ambient corona [131–133]. However, the reconnection region has a characteristic size of only $\sim 10^4$ km [51, 129, 134, 135], corresponding to a free-streaming escape time of approximately 1 s. This is substantially shorter than the observed electron energization timescale, inferred from the rise time of hard X-ray emission, which is typically on the order of minutes [130, 136, 137]. Therefore, without an effective mechanism to suppress particle transport or confine energetic electrons within the acceleration region, electrons would escape before being accelerated to the observed high energies.

Further, imaging spectroscopy observations have shown that the energetic electron flux inferred at the looptop can exceed the precipitation rate at the footpoints by factors of $\sim$ 1.7–8 during the impulsive phase of solar flares [128]. These observations suggest that a significant fraction of accelerated electrons remain confined within coronal loops rather than freely streaming into the chromosphere [128].

1.3.1.2 Looptop Microwave Sources

Solar microwave emission is primarily produced by gyrosynchrotron radiation from nonthermal electrons spiraling around coronal magnetic field lines [138–140]. As a result, microwave radiation serves as an important diagnostic of the motion of energetic electrons on coronal magnetic fields. Similar to looptop hard X-ray sources, observations have frequently revealed nonthermal microwave sources located near and above the looptop region where magnetic reconnection is driving particle energy gain (e.g., [141–144]). The presence of these coronal microwave sources implies that a substantial population of energetic electrons remains confined within the flare region, rather than rapidly escaping along magnetic field lines.

The observed looptop microwave emission also places important constraints on the electron pitch-angle distribution. The pitch angle α is defined as $\cos\alpha = v_{\parallel}/v$. Previous studies have shown that electron distributions with enhanced populations near pitch angles of 90° can significantly increase the coronal gyrosynchrotron emission [140]. Since gyrosynchrotron radiation is produced by electrons gyrating around magnetic field lines and therefore requires a substantial perpendicular velocity component, some physical process must scatter or redistribute electron energy from the parallel direction, where it is driven during reconnection, into perpendicular motion.

1.3.1.3 The Long Cooling-Time Problem

Another long-standing problem in solar flare physics is the unexpectedly long cooling time of hot coronal plasma. In the classical picture, the high temperatures reached in flare plasmas should result in highly efficient field-aligned conductive energy losses. However, observations have shown that soft X-ray flare loops and post-flare coronal loops often persist much longer than predicted by classical

conductive cooling models based on Spitzer thermal conduction (e.g., [145–151]). For example, detailed comparisons between soft X-ray and Hα post-flare loops have shown cooling times from ~ 10 minutes in the early phase to ~ 40 minutes in the later phase of flare evolution [152]. By contrast, the classical Spitzer conductive cooling time, $\tau \sim 3nkL^2/\kappa_{\parallel}$, where $\kappa_{\parallel} \propto T^{5/2}$ is the parallel conductivity, predicts much shorter cooling times on the order of only tens of seconds. This discrepancy implies that additional physical processes must either suppress the effective thermal transport or sustain prolonged energy release in the corona.

Although the coronal plasma cooling problem primarily concerns thermal electrons, it is closely related to the confinement of nonthermal electrons responsible for hard X-ray and microwave emission. Both problems ultimately involve the regulation and suppression of electron transport in the corona. Mechanisms capable of reducing thermal conduction may also scatter or confine energetic nonthermal electrons, and vice versa. Understanding how electron transport operates across both thermal and nonthermal energy ranges is therefore essential for understanding particle energy gain in flares as well as long-lived looptop hard X-ray and microwave sources.

1.3.2 Alternative Explanations

These observational and theoretical considerations have motivated several proposed mechanisms for the confinement and scattering of energetic electrons in the corona.

1.3.2.1 Magnetic Trapping

One possibility is magnetic trapping, in which the converging magnetic field geometry near the loop footpoints naturally forms a magnetic mirror, allowing energetic electrons to remain confined

near the coronal loop-top region. However, efficient magnetic mirroring requires electrons to possess sufficiently large perpendicular velocities. In contrast, simulations of magnetic reconnection have shown that the primary energy gain during the acceleration process is parallel to the ambient magnetic field [15, 40, 41]. Therefore, efficient confinement requires an additional scattering process capable of redistributing electron energy from the parallel to the perpendicular direction.

1.3.2.2 Termination Shock

Another proposed mechanism involves reconnection-driven termination shocks [153–156]. In solar flares, magnetic reconnection generates high-speed outflows that can become super-magnetosonic and collide with the underlying closed flare loops. As the outflow is abruptly decelerated and compressed, a fast-mode termination shock can form near the looptop region [153, 154, 156]. Simulations have shown that such reconnection outflows can generate a termination shock together with a concave-shaped magnetic structure below the shock front [156]. This magnetic configuration can act as a magnetic trap that confines energetic electrons near the loop top, allowing particles to encounter the shock multiple times and undergo further acceleration.

1.3.2.3 Double Layer

Another possible mechanism is the formation of a highly localized electrostatic potential structure, or double layer (DL) [157–159]. In this scenario, hot electrons escaping from the coronal acceleration region generate a return current. The relative drift between the return-current electrons and the background ions drives streaming instabilities, which subsequently produce a DL with a strong localized electric field. The associated electrostatic potential drop can reflect and decelerate electrons propagating away

from the looptop region, thereby reducing the electron heat flux and partially suppressing energetic electron transport. PIC simulations have shown that such DLs can substantially extend the confinement time of energetic electrons in coronal sources [157–159]. However, the effectiveness of confinement by a DL depends on the magnitude of the electrostatic potential drop, which scales approximately with the hot electron temperature T_{eh} [158, 159]. Since $T_{eh} \ll m_e c^2$, the resulting potential drop is generally insufficient to confine the highest-energy nonthermal electrons responsible for hard X-ray and microwave emission.

1.3.2.4 Turbulence

Plasma turbulence refers to a chaotic state of plasma motion characterized by fluctuations in plasma velocity, density, electric fields, and magnetic fields over a broad range of spatial and temporal scales. In turbulent plasmas, energy is transferred nonlinearly from large scales to progressively smaller scales, where it can eventually be dissipated through kinetic processes. Plasma turbulence is ubiquitous in both laboratory and astrophysical plasmas, including the solar wind, the solar corona, planetary magnetospheres, and magnetic reconnection regions. In reconnection systems, turbulence can distort current layers, enhance particle scattering and transport, and contribute to plasma heating and particle acceleration.

Another proposed mechanism for the suppression of electron transport and heat conduction is plasma turbulence [160–162]. Turbulent fluctuations can alter magnetic field topology, enhance field-line wandering, and increase electron pitch-angle scattering, thereby reducing the efficiency of free streaming along the large-scale magnetic field [162–164]. As a result, turbulence can reduce the effective thermal conductivity and suppress the escape of energetic electrons from the acceleration

region. Studies of turbulent reconnection further suggest that turbulence is a natural ingredient of high-Reynolds-number astrophysical plasmas and can strongly modify both reconnection and transport processes [164]. However, numerical modeling indicates that the turbulence generated during reconnection must persist well beyond the impulsive phase to fully explain the observations [162].

1.3.3 The Wave–Particle Interaction and Whistler Instability

Pitch-angle scattering associated with wave–particle interactions driven by kinetic instabilities is another candidate mechanism for electron scattering during magnetic reconnection [165–172]. A wide variety of waves and instabilities can develop in reconnection regions, including lower-hybrid waves, whistler waves, upper-hybrid waves, ion-acoustic waves, and anisotropy-driven instabilities such as the firehose instability [168, 173]. These waves and turbulent fluctuations can strongly modify reconnection dynamics by enhancing particle scattering and diffusion, regulating energy conversion, and contributing to plasma heating [168, 173].

Among these processes, whistler-wave scattering has been proposed as a promising mechanism for suppressing electron transport in flare-like plasmas [169–172]. The basic physical mechanisms underlying whistler-wave scattering will be discussed in more detail in the next section. Particle-in-cell simulations have been carried out to study energetic electrons escaping from a reconnection-driven energy-release region [172]. In their model, the escaping energetic electrons generated a strong field-aligned heat flux together with a cold return-current beam, which drove large-amplitude oblique whistler waves and electron acoustic waves. These waves efficiently scattered energetic electrons, increased their perpendicular velocity, reduced the parallel heat flux, and significantly shortened the electron mean free path. The authors suggested that such wave–particle interactions may help confine

energetic electrons within flare acceleration regions and explain the long confinement times inferred from hard X-ray observations.

1.4 Whistler-Wave Scattering of Energetic Electrons

1.4.1 Basic Principles

Whistler waves are right-hand-polarized electromagnetic waves with frequencies between the ion and electron cyclotron frequencies [26, 27, 174]. They are referred to as whistler waves because, in Earth's magnetosphere, their dispersive propagation causes high-frequency components to travel faster than low-frequency components, producing a characteristic descending tone, or "whistle," in radio observations. Whistler waves are common in a wide range of space plasmas, including the solar corona, magnetosphere, and intracluster medium (ICM) (e.g., [175–179]). Whistler-wave scattering is regarded as one of the primary mechanisms regulating the transport and loss of energetic particles [180–184].

Whistler waves can propagate either parallel or obliquely with respect to the background magnetic field. In the case of parallel whistlers, the wave vector is parallel to the magnetic field, and the wave is predominantly a transverse right-hand polarized electromagnetic mode with little or no parallel electric field. As a result, particle scattering is mainly mediated through cyclotron resonances. In contrast, oblique whistlers propagate at a finite angle to the background magnetic field and possess a finite parallel electric field component. This allows not only cyclotron resonances, but also Landau resonances, making oblique whistlers particularly effective at pitch-angle scattering, electron diffusion, and heat-flux suppression in collisionless plasmas.

In the cold-plasma limit under the condition $v_{Ae} \ll c$, the whistler dispersion relation is [26, 185]

$$\omega = \frac{|k_\parallel| k d_e^2}{1 + k^2 d_e^2} \Omega_e, \tag{1.4}$$

or equivalently,

$$\frac{v_{ph}}{v_{Ae}} = \frac{k d_e}{1 + k^2 d_e^2}, \tag{1.5}$$

where ω is the wave frequency, $k_\parallel$ is the parallel component of the wave vector, d_e is the electron skin depth, Ω_e is the electron cyclotron frequency, v_{Ae} is the electron Alfvén speed, and $v_{ph} = \omega / k_\parallel$ is the parallel phase speed. Since v_{ph} reaches a maximum value of $0.5\, v_{Ae}$ at $k d_e = 1$, the characteristic phase speed of whistler waves is of order v_{Ae}.

1.4.2 Resonant Interactions

The wave–particle interactions are governed by the resonance condition

$$\omega - k_\parallel v_\parallel - n \Omega_e = 0 \tag{1.6}$$

where $v_\parallel$ is the particle velocity parallel to B_0 and n is an integer [26, 185]. Here, $n = 0$ corresponds to the Landau resonance, while $n = 1$ and $n = -1$ correspond to the normal and anomalous cyclotron resonances, respectively.

According to quasilinear theory, resonant particles diffuse in velocity space along curves of constant energy in the wave frame. In this picture, the diffusive flux is tangent to circles centered at $v_\parallel = v_{ph}$:

$$\left(v_\parallel - v_{ph}\right)^2 + v_\perp^2 = \text{constant} \tag{1.7}$$

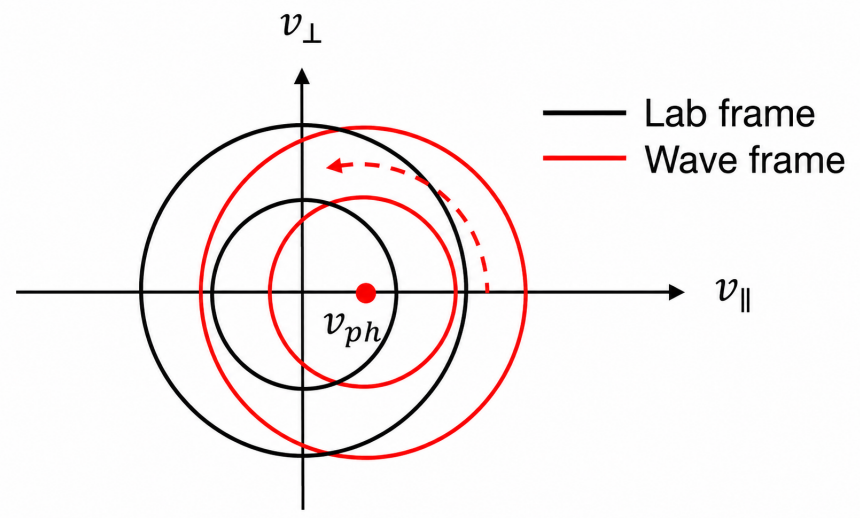


Figure 1.7: Schematic illustration of resonant scattering by whistler waves. The dashed line indicates the diffusion path of resonant particles in velocity space along a circle centered on v_{ph}.

Figure 1.7 provides a schematic illustration of Equation 1.7. In the wave frame, the particle energy is conserved, whereas in the laboratory frame particles can lose energy to the growing wave. A necessary condition for wave growth is $0 < v_{ph} < v_0$, where v_0 is the mean drift speed associated with the electron distribution [186]. Strong scattering can produce horn-like structures or perpendicular bumps in the velocity distribution at resonant velocities [172, 187–189].

As the wave amplitude increases, the resonance widths broaden and may eventually overlap [169,181,189]. Once resonance overlap occurs, particle motion becomes diffusive rather than periodic, allowing electrons that initially have small pitch angles to scatter across a broad range of pitch angles, even beyond $90°$.

The resonance width describes the range of particle velocities over which a wave can effectively interact with resonant particles through wave–particle interactions. Although resonance conditions such as $\omega - k_\parallel v_\parallel - n\Omega_e = 0$ are often written as exact equalities, finite-amplitude waves can interact with particles within a finite velocity interval around the resonant velocity. In general, larger wave

amplitudes correspond to broader resonance widths and therefore more efficient particle scattering or trapping.

In realistic plasmas, however, the wave field often consists of a broad spectrum of modes with different wavevectors, frequencies, and propagation angles. Since each wave mode satisfies the resonance condition at a different resonant velocity, multiple resonance regions can exist simultaneously in velocity space. When the resonance widths become sufficiently broad, neighboring resonances may begin to overlap. In this regime, particle trajectories can become stochastic rather than periodic, leading to enhanced diffusion and strong pitch-angle scattering. This process, commonly referred to as resonance overlap, is believed to play an important role in turbulent plasmas and in the suppression of energetic-electron transport in collisionless reconnection systems.

The distinction between parallel and oblique whistlers is particularly important for electrons with $|v_\parallel/v_{the}| \ll 1$. For parallel whistlers, the wave electric field is primarily transverse and there is little or no parallel electric field. As a result, the dominant interaction occurs through cyclotron resonance [190],

$$v_{\parallel\mathrm{res}} = \frac{\omega - \Omega_e}{k_\parallel} = -\frac{v_{Ae}}{(1 + k_\parallel^2 d_e^2) k_\parallel d_e}, \tag{1.8}$$

so that electrons with small parallel velocities can resonate only with short-wavelength whistlers satisfying $k_\parallel d_e \gg 1$, where the wave power is typically weak. Consequently, low-$v_\parallel$ electrons are not efficiently scattered by parallel whistlers.

In contrast, oblique whistlers possess a finite parallel electric field, allowing electrons to interact through Landau resonance,

$$v_{\parallel\mathrm{res}} = \frac{\omega}{k_\parallel} = \frac{k d_e v_{Ae}}{1 + (k d_e)^2}, \tag{1.9}$$

which can involve long-wavelength modes with $k d_e \ll 1$. Therefore, provided that sufficient wave

power exists at long wavelengths, oblique whistlers can efficiently scatter electrons with small parallel velocities.

Here, it is worth mentioning the heat-flux suppression by oblique whistler waves in the fast solar wind, where recent studies have provided a detailed picture of the underlying resonant scattering mechanisms. In the solar wind, the electron heat flux is primarily carried by the "strahl" component, a field-aligned beam-like population of suprathermal electrons. Observations demonstrate that the strahl gradually broadens, i.e., its pitch-angle width increases with heliocentric distance, and may evolve into the more isotropic halo population through pitch-angle scattering processes [191–193], although alternative interpretations have also been proposed [194–196]. Since Coulomb collisions are weak in the fast solar wind, wave–particle interactions driven by kinetic instabilities are believed to play a significant role in regulating electron transport and heat flux.

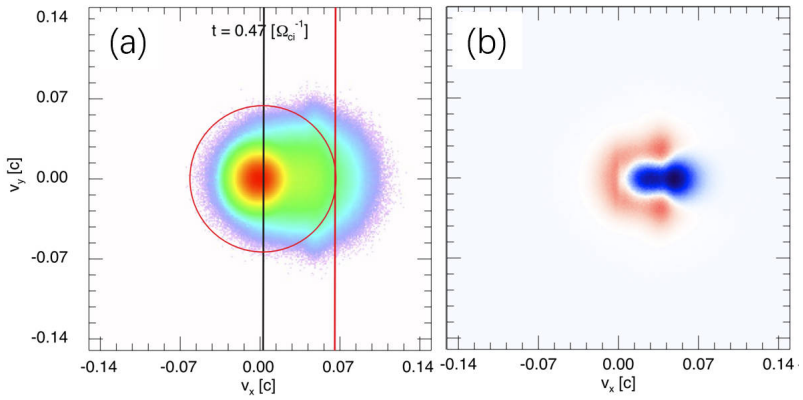


Figure 1.8: (a) Electron velocity distribution. Black and red lines indicate the locations of the $n = 0$ (Landau) and $n = -1$ (anomalous cyclotron) resonances, while the circle shows the electron diffusion path associated with the $n = -1$ resonance interaction. (b) Temporal variation of the distribution function, where red indicates an increase and blue indicates a decrease in phase-space density. Adapted from [197].

Particle-in-cell simulations have shown that, under typical solar-wind conditions, the counter-streaming core–strahl electron distribution can excite oblique whistler heat-flux instabilities [186, 197–200]. Figure 1.8 shows an example of such simulation results from [197]. In the early stage of the

instability, oblique whistler waves scatter strahl electrons through the $n = -1$ cyclotron resonance, causing electrons to diffuse toward higher perpendicular velocities and broadening the pitch-angle distribution. As the instability evolves, the finite parallel electric field associated with oblique whistlers also enables $n = 0$ Landau resonances, which further redistribute electrons along the parallel direction and contribute to the formation of a more isotropic halo population. The simulations further showed that quasi-parallel whistler waves can develop at later times and continue to isotropize the suprathermal electrons. These results indicate that oblique and parallel whistler waves can work together to suppress electron heat flux and regulate energetic-electron transport in weakly collisional plasmas.

1.4.3 The 90 Degree Problem

An important issue in wave–particle scattering theory is the so-called "90 Degree Problem" [201–207]. The pitch angle $\alpha = 90^\circ$ corresponds to particles with nearly zero parallel velocity. In conventional quasilinear theory, the pitch-angle diffusion coefficient decreases strongly near $\alpha = 90^\circ$, making it difficult for particles to scatter across 90° and become fully isotropized.

This problem is particularly important for energetic-electron transport, cosmic-ray propagation, and heat-flux suppression in weakly collisional plasmas. A key requirement for strong transport inhibition is that electrons be scattered over a broad range of pitch angles with respect to the ambient magnetic field. This raises a long-standing question: can whistler waves efficiently scatter electrons across 90°? If not, the vanishing of the diffusion coefficient near 90° may cause particles to accumulate near this pitch angle and form an effective transport barrier that limits further isotropization and transport suppression. This possibility motivates the study of whether such a barrier can persist and whether whistler waves can overcome it and scatter electrons beyond 90°.

Recent studies suggest that nonlinear interactions, resonance overlap, and oblique whistler waves with finite parallel electric fields may enhance scattering near $\alpha \approx 90^\circ$ and help overcome the 90 degree barrier. The nature of this problem has been investigated in a variety of plasma environments. PIC simulations of energetic-electron transport in solar flares [167, 172] and of strahl scattering in the solar wind [197] suggest that oblique whistlers can scatter electrons beyond 90° through nonlinear wave–particle interactions. In Earth's bow shock, observations similarly indicate that nonthermal electrons can be scattered beyond 90° by whistler waves [208]. In Earth's radiation belts, large-amplitude electromagnetic ion cyclotron waves can scatter relativistic electrons across 90° through cyclotron resonance, leading to precipitation losses [209–213]. These studies collectively suggest that nonlinear scattering across 90° is a generic feature of sufficiently strong wave activity.

PIC simulations further show that flare-driven heat flux can self-generate strong whistler turbulence that scatters electrons toward larger perpendicular velocities and suppresses their escape from the acceleration region [167,172]. By contrast, studies of high-β intracluster-medium plasmas have argued that weak turbulence and large system sizes can maintain an effective transport barrier near 90° [190].

1.5 Numerical Method: Particle-in-Cell Simulations

1.5.1 Basic Principles

In this thesis, the main numerical tool is the particle-in-cell (PIC) simulation method, which is widely used in plasma physics to study kinetic scale phenomena beyond the scope of fluid models [214–217]. All PIC simulations presented in this thesis are carried out using the code `p3d` [218].

In the PIC approach, a plasma is represented by a large number of computational particles, each of which corresponds to many physical particles with the same charge-to-mass ratio. These

computational particles are often referred to as superparticles. Figure 1.9(a) illustrates the basic structure of a PIC simulation. The particles move continuously under the influence of self-consistent electromagnetic fields. The fields are defined on a spatial grid and evolved according to Maxwell's equations, while the particles are advanced using the relativistic Newton–Lorentz equation of motion. In this way, the PIC method self-consistently couples particle dynamics to the evolution of electric and magnetic fields.

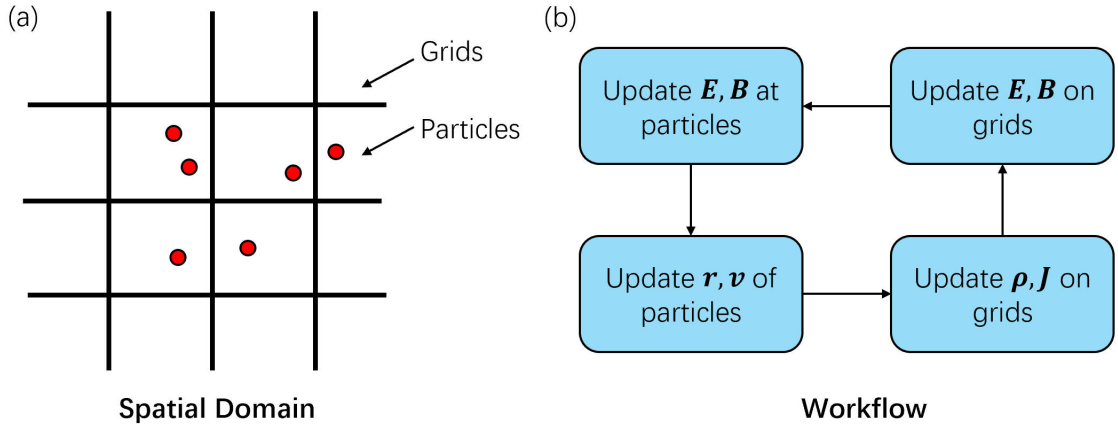


Figure 1.9: (a) Schematic illustration of the spatial distribution of particles and grids in a PIC simulation. (b) A typical four-step PIC workflow.

Figure 1.9(b) shows a standard PIC calculation cycle. First, the charge and current carried by the particles are deposited onto the grid. Next, Maxwell's equations are solved on the grid to update the electric and magnetic fields. The updated fields are then interpolated from the grid back to the particle positions. Finally, the particle velocities and positions are advanced in time using the Lorentz force. Repeating this cycle allows the simulation to follow the simultaneous evolution of particle distributions and electromagnetic fluctuations. Additional numerical details involved in the PIC procedure, such as particle–grid interpolation schemes, numerical differentiation methods, and parallel communication strategies, are beyond the scope of this introduction and will not be discussed here.

An important numerical constraint in explicit PIC simulations is that the time step and grid

spacing must satisfy the Courant–Friedrichs–Lewy (CFL) condition,

$$u\Delta t < \Delta x, \tag{1.10}$$

where u is a characteristic particle speed, typically taken to be the thermal speed or Alfvén speed, Δt is the time step, and Δx is the grid spacing. In addition, the numerical resolution must be sufficient to capture the relevant plasma scales. In practice, this requires the time step to be small enough to resolve the plasma and cyclotron frequencies, and the grid spacing to be fine enough to resolve the Debye length and the electron gyroradius [214, 215], i.e.,

$$\Delta t < \omega_{pe}^{-1},\ \omega_{ce}^{-1}, \tag{1.11}$$

and

$$\Delta x < \lambda_D,\ \rho_e, \tag{1.12}$$

where ω_{pe} and ω_{ce} are the electron plasma frequency and electron cyclotron frequency, respectively, λ_D is the Debye length, and ρ_e is the electron gyroradius.

An important advantage of the PIC method is that it naturally captures kinetic-scale physics, especially anisotropy-driven plasma instabilities and wave–particle interactions. These processes are central to the problems studied in this thesis. The main limitation of the PIC method is that the required spatial and temporal resolution can make simulations computationally expensive, especially for large system sizes and long evolution times. For example, in a coronal plasma with a density of $n_e \sim 10^9\,\mathrm{cm}^{-3}$, the electron inertial length is only $d_e \sim 17\,\mathrm{cm}$, while a typical coronal structure can have a macroscopic size of order 10^4–$10^5\,\mathrm{km}$. Resolving such a system from electron kinetic

scales to global coronal scales would therefore require more than 10^8 grid cells in a single spatial direction, far beyond the capability of fully kinetic simulations. As a result, PIC simulations usually employ reduced system sizes, reduced mass ratios, or other normalized parameters while attempting to preserve the essential kinetic physics.

1.5.2 Comparison with MHD Simulations

Magnetohydrodynamics (MHD) is another widely used numerical framework in plasma physics [215, 219–221]. In MHD, the plasma is treated as a conducting fluid described by macroscopic quantities such as density, bulk velocity, pressure, and magnetic field. Instead of following individual particles, MHD evolves fluid variables and electromagnetic fields at large scales.

A major advantage of MHD simulations is their relatively low computational cost, so that they can describe plasma behavior over large spatial and temporal scales. They are therefore well suited for studying the formation of current sheets, the global topology of magnetic fields, and large-scale plasma flows. However, since MHD is based on fluid moments, it cannot fully resolve the velocity distribution function or self-consistently capture kinetic-scale processes such as wave–particle interactions and the growth of electron-scale instabilities.

Between single-fluid MHD and fully kinetic PIC methods, there also exist intermediate approaches, such as Hall MHD or hybrid simulations, but these approaches still cannot resolve electron-scale physics as accurately as PIC simulations. The problems studied in this thesis fundamentally require a kinetic description and therefore motivate the use of PIC simulations.

1.6 Outline of the Thesis

This thesis is organized as follows. Chapter 1 provides the general introduction and physical background. Chapters 2, 3, and 4 present the results of three peer-reviewed publications that form the core of this thesis [167, 222, 223]. Chapter 5 provides a summary and outlook.

Chapter 2 is adapted from [223] and presents particle-in-cell simulations of magnetic reconnection that investigate the generation of core magnetic fields in flux ropes together with the associated electron scattering processes. This chapter is primarily related to the topics discussed in Sections 1.1, 1.2, and 1.5. Both the zero-guide-field and strong-guide-field regimes are examined, and the results show that the Weibel instability and the electron Kelvin–Helmholtz instability are the dominant mechanisms in the respective regimes.

Chapter 3 is adapted from [167] and studies wave generation and energetic-electron scattering in solar flares, corresponding mainly to the topics discussed in Sections 1.3, 1.4, and 1.5. This chapter investigates how anisotropic flare-like electron distributions can drive strong oblique whistler waves and how these waves subsequently scatter energetic electrons and suppress electron transport.

Chapter 4 is adapted from [222] and investigates the problem of whistler-wave scattering of energetic electrons across 90° pitch angle, corresponding primarily to the topics discussed in Sections 1.3, 1.4, and 1.5. This chapter addresses the long-standing question of whether a persistent 90° pitch-angle barrier can inhibit efficient electron scattering and transport suppression.

Finally, Chapter 5 summarizes the main results of the thesis and highlights the physical connections among the three studies. It also discusses the primary limitations of the present work and outlines several directions for future research.

Chapter 2: Self-Generation of Core Fields and Electron Scattering in Flux Ropes

2.1 Background

As discussed in Section 1.2, magnetic islands and flux ropes are common structures produced during magnetic reconnection and are central to energy conversion, particle acceleration, and transport. Observations in the magnetotail and magnetopause frequently reveal strong out-of-plane magnetic fields within the cores of these structures (e.g. [72, 77, 78, 81, 82]). Similar structures are also widely observed in solar eruptive phenomena such as flares, coronal mass ejections, and jets [83, 84, 87, 88, 91, 92]. Despite their ubiquity, the physical origin of these strong core magnetic fields and their impact on particle acceleration remain poorly understood.

Previous studies have mainly attributed strong core-field generation to the compression of an initial guide field during island contraction, possibly aided by plasma depletion within the island interior and the associated reduction of thermal pressure [70, 99–102]. Other studies have interpreted the core field in terms of Hall currents during reconnection [95–98]. Although these mechanisms may provide plausible explanations under certain conditions, they do not fully account for the development of strong core fields in the absence of an initial guide field [72]. Furthermore, they fail to explain observations of core fields whose polarity is opposite to that of the surrounding guide field [78, 224].

Kinetic effects are especially important because magnetic reconnection naturally generates strong electron temperature anisotropy. The resulting anisotropic distribution provides free energy for instabilities such as the Weibel instability [103, 225] and the electron Kelvin–Helmholtz instability [120, 122], both of which can produce filamentary magnetic fields [226–229]. These self-generated magnetic fields can contribute directly to the core magnetic field, enhancing electron scattering and reducing reconnection-driven energization. Thus, the formation of core magnetic fields is closely connected to the transport

and acceleration of energetic electrons during magnetic reconnection.

In this chapter, we use two-dimensional particle-in-cell simulations with a realistic proton-to-electron mass ratio to investigate the self-generation of core magnetic fields in reconnecting magnetic islands. We consider both the zero-guide-field and strong-guide-field regimes. Particular attention is given to the roles of the Weibel instability, separatrix electron currents, the electron Kelvin–Helmholtz instability, and island merging in generating and maintaining strong out-of-plane magnetic fields, as well as to the implications of these fields for electron scattering.

2.2 Simulation Setup

The proton-to-electron mass ratio is $m_i/m_e = 1836$, with the term "ion" in this work referring exclusively to protons. The simulation domain contains two Harris-type current sheets, with the initial magnetic field specified as $B_x(y) = B_0 \left[\tanh\big((y - 0.25\,l_y)/w_0\big) - \tanh\big((y - 0.75\,l_y)/w_0\big) - 1\right]$, where w_0 is the half-width of the current sheet. We choose $w_0 = 0.012d_i \approx 0.5d_e$, where $d_i = c/\omega_{pi}$ is the ion inertial length and $\omega_{pi} = (4\pi n_i e^2/m_i)^{1/2}$ is the ion plasma frequency. The system size is $l_x = 2l_y = 15.36d_i$ and periodic boundary conditions are applied in both directions. We first carry out a simulation with no initial guide field and subsequently introduce an initial guide field, $B_z = B_g$, to examine its influence on the system. Both electrons and ions are initialized with Maxwellian velocity distributions. To maintain an equilibrium configuration, the density profile is given by $n_e = n_i = [\,\mathrm{sech}^2((y - 0.25\,l_y)/w_0) + \mathrm{sech}^2((y - 0.75\,l_y)/w_0)\,]/(2T) + n_0$. The simulation time step is $dt = 10^{-5}\Omega_i^{-1}$, $v_{Ai} = B_0/\sqrt{4\pi n_0 m_i} \approx 0.01c$, and $\beta = 8\pi n_0 T/B_0^2 \approx 0.05$. The simulation uses 500 particles per species per cell and employs a grid of 6144 by 3072 cells.

2.3 Simulation Results

2.3.1 Zero-Guide-Field Case

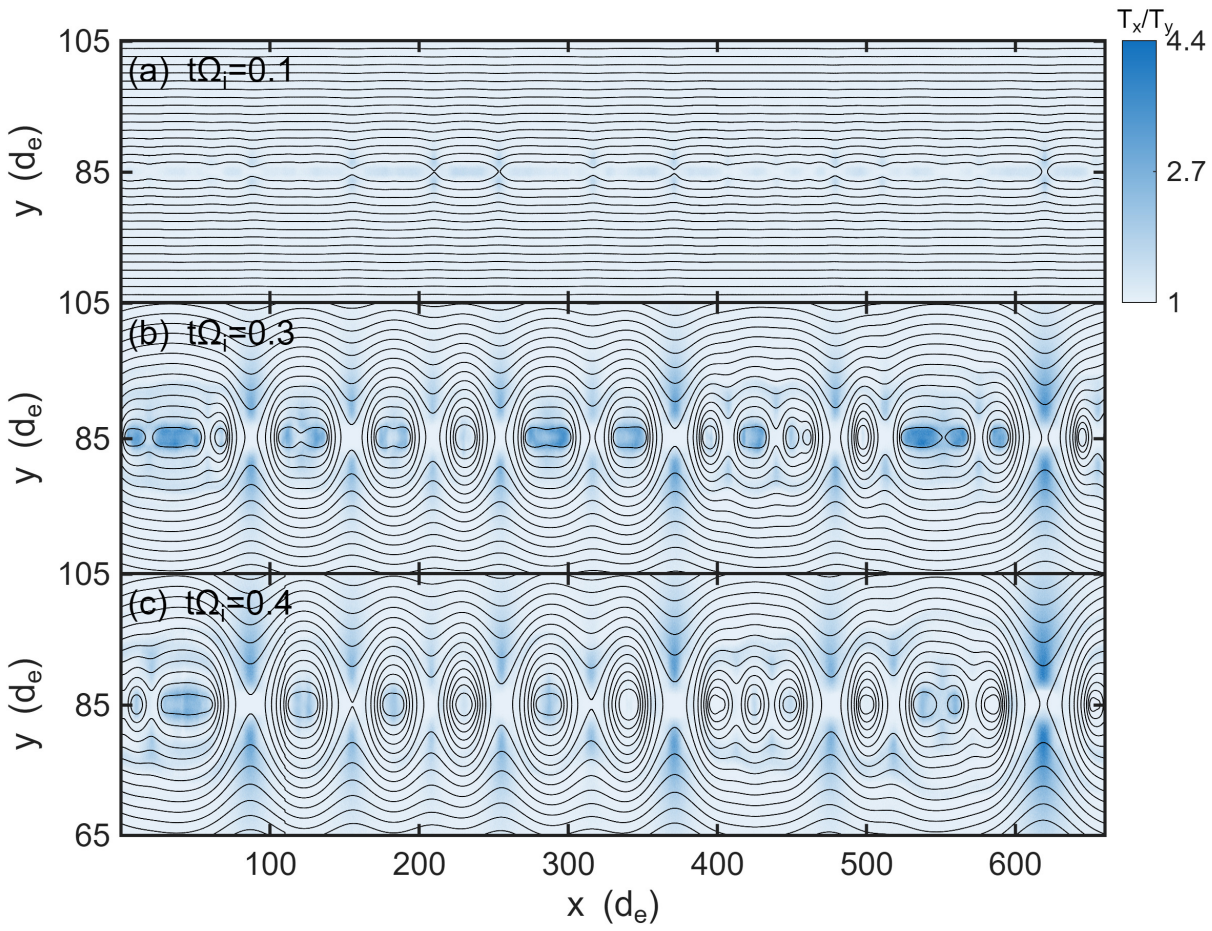


Figure 2.1: Structure of the lower current sheet (the simulation domain contains two current sheets) at (a) $t\Omega_i = 0.1$, (b) $t\Omega_i = 0.3$ and (c) $t\Omega_i = 0.4$. Black lines denote magnetic field lines and the color scale shows the electron temperature anisotropy T_x/T_y.

Figure 2.1 shows the dynamics in the lower current sheet. In panel (a), anti-parallel magnetic field lines break and reconnect, forming multiple X-lines, with magnetic islands developing between them. The increase in temperature anisotropy upstream of the X-lines arises from the conservation of the magnetic moment μ. In panel (b), electrons are accelerated at the X-lines, and the resulting

outflows produce strong temperature anisotropies inside the islands, reaching $T_x/T_y \sim 4.5$. This strong anisotropy triggers the Weibel instability within the region where B_x is small. In panel (c), the anisotropy inside the islands is substantially reduced due to the scattering from the instability, with $T_x/T_y \sim 1$. Compared with panel (b), the islands also broaden in the y direction.

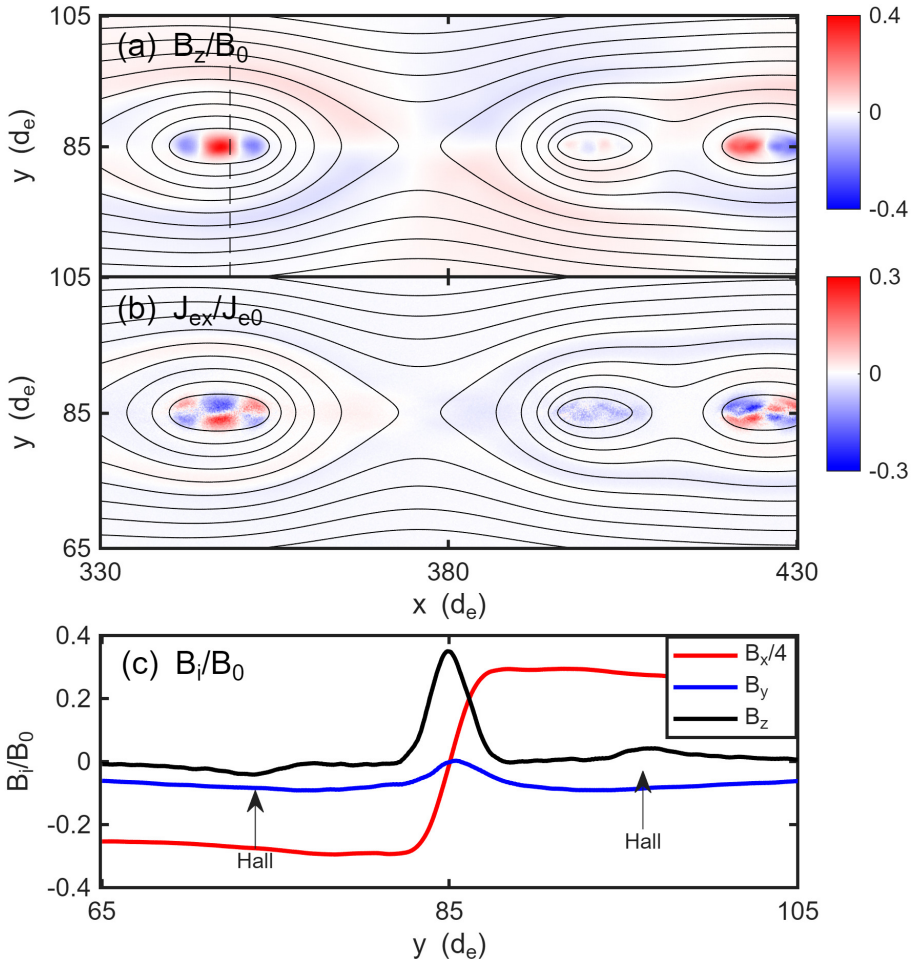


Figure 2.2: (a) Out-of-plane magnetic field B_z at $t\Omega_i \approx 0.37$. Black contours indicate magnetic field lines. (b) The x-direction electron current J_{ex} at the same time. The electron current is normalized by $J_{e0} = en_0v_{Ae}$ where v_{Ae} is the electron Alfvén speed. (c) Magnetic field components along the vertical dashed line in (a). The perturbations due to the usual Hall field are indicated.

Figure 2.2 shows a zoomed-in view around a reconnection site. In panel (a), the Weibel instability at the island center generates strong out-of-plane magnetic fields with amplitudes reaching $B_z/B_0 \sim$

0.4, greatly exceeding the quadrupolar Hall magnetic field. The resulting B_z alternates in sign along the x direction, while only a single wavelength develops in the y direction. In principle, linear theory predicts that the wave vector of the Weibel instability is oriented along the y direction, i.e., perpendicular to the direction of temperature anisotropy, leading to the formation of multiple magnetic filaments [103, 230, 231]. In the present simulation, however, the growth of Weibel modes in the y direction is constrained by the narrow width of the current sheet ($\sim 0.5\, d_e$), which is bounded on both sides by regions of strong B_x, the ambient magnetic field. For the same reason, no clear Weibel signatures are observed upstream of the X-line, even in the presence of strong temperature anisotropy.

Figure 2.2(b) shows enhanced electron fluxes inside the magnetic island, where the electron current exhibits a crossover pattern. This current structure is consistent with the spatial variation of the Weibel-generated magnetic fields along the x direction. These bipolar out-of-plane magnetic structures therefore result from the Weibel instability rather than from compression of the ambient magnetic field. In contrast, the ion flow (not shown), with J_{ix}/J_{e0} ranging from -0.08 to 0.08, does not participate in the instability.

Figure 2.2(c) shows the variations of the magnetic-field components along a vertical cut (indicated by the dashed line in panel (a)) through the magnetic island. The out-of-plane magnetic field B_z exhibits a pronounced peak at the island center, where B_x reverses sign. In contrast, the Hall magnetic field appears in regions displaced from the island center, with an amplitude that is significantly smaller than that of the Weibel-generated B_z. It is worth noting that, for a horizontal cut through the island, B_z exhibits multiple bipolar peaks at locations where B_y reverses sign. Similar signatures have been reported in magnetotail observations. For example, Cluster measurements of the structure of a magnetic island reveal a peak in the cross-tail magnetic field in the island core and a peak in the total magnetic-field magnitude at the same location [72]. There was no ambient guide field in these

observations so the large guide field did not result from the compression of an ambient guide field. Further discussion of this event is presented later, following an exploration of the role of the guide field.

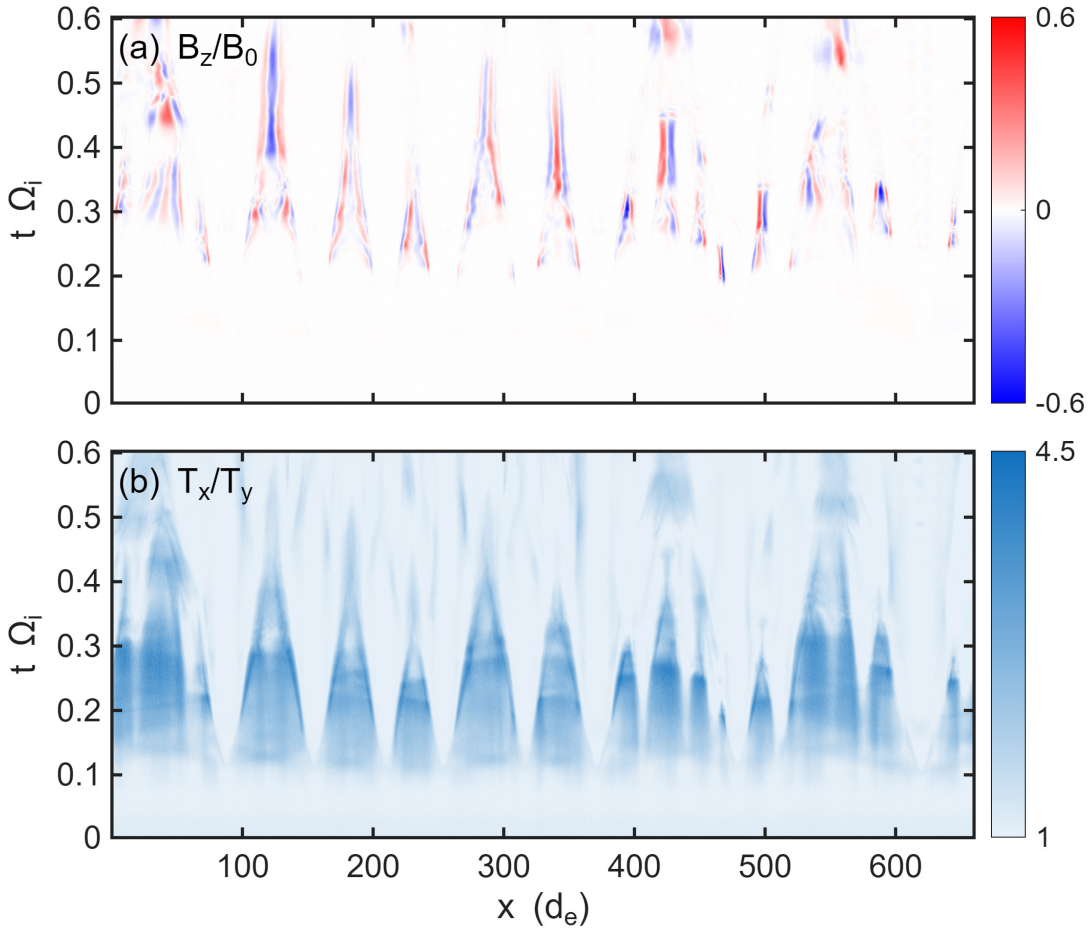


Figure 2.3: Space–time plot of the out-of-plane magnetic field B_z and electron temperature anisotropy T_x/T_y in the center of the lower current sheet.

Figure 2.3 shows the time evolution of the out-of-plane magnetic field B_z and the electron temperature anisotropy T_x/T_y at the center of the lower current sheet. The anisotropy begins to develop at $t\Omega_i \approx 0.15$ as electrons are accelerated by reconnection. Shortly thereafter, at $t\Omega_i \approx 0.2$, an enhancement of B_z emerges as the Weibel instability is triggered by the growing anisotropy. The clear one-to-one temporal correspondence between the anisotropy and the growth of B_z confirms that

the Weibel instability is responsible for generating the strong out-of-plane magnetic field in the island center. The anisotropy starts to decrease at $t\Omega_i \approx 0.3$ as a result of pitch-angle scattering by the Weibel-generated fields. As the anisotropy is reduced and the instability drive weakens, the B_z signal decays. A magnetic-island merging event occurs near $d_e \approx 450$ at $t\Omega_i \approx 0.3$. Following this merger, the anisotropy reappears with a reduced amplitude at $t\Omega_i \approx 0.5$, accompanied by a renewed increase in B_z around $t\Omega_i \approx 0.6$. This sequence demonstrates that island coalescence regenerates temperature anisotropy, which again drives the growth of the Weibel instability and the associated generation of the out-of-plane magnetic-field.

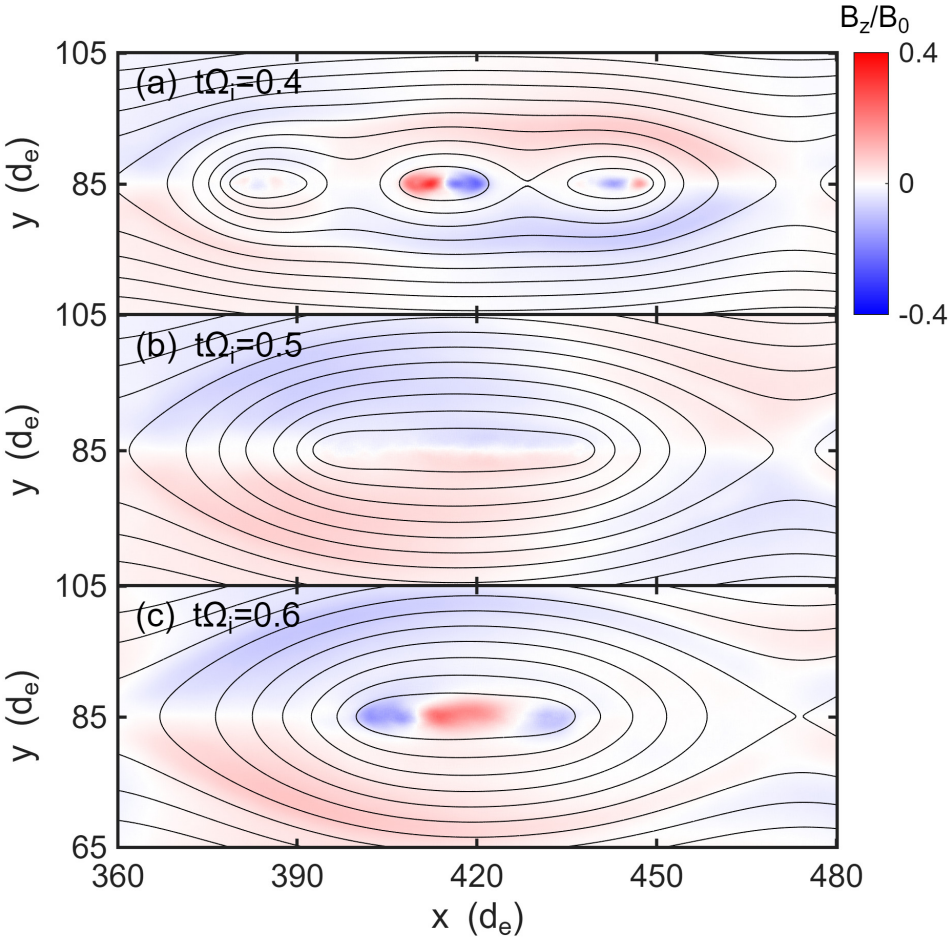


Figure 2.4: Weibel evolution during flux-rope merging. Black contours denote magnetic field lines, and the color scale shows the out-of-plane magnetic field B_z/B_0.

Figure 2.4 shows the impact of island on Weibel generated fields. The three smaller islands in panel (a) coalesce into a larger island in panel (b). During this process, the initial B_z structures shown in panel (a) dissipate and partially cancel. Island merging leads to the re-emergence of temperature anisotropy as magnetic field lines contract in the x direction [70, 71, 232, 233]. The regenerated anisotropy excites the Weibel instability again, as shown in panel (c), although the resulting B_z amplitude is weaker than that produced during the initial reconnection phase in panel (a). This merging process highlights that island dynamics play a critical role in regenerating anisotropy and sustaining Weibel activity well beyond the onset of reconnection. Thus, strong out-of-plane magnetic-field signatures may persist longer than expected as a result of island merging as the release of magnetic energy continues.

Since the strength of the initial guide field is expected to play an important role, we have varied this parameter. For weaker guide fields ($B_g/B_0 \sim 0.2$), the peak anisotropy is reduced because the guide field suppresses reconnection-driven electron acceleration [234–236]. The bipolar magnetic-field structure produced by the Weibel instability remains significant, but is shifted by the presence of the guide field: both the minimum and maximum values of the out-of-plane magnetic field are offset by the guide field, while their difference remains approximately unchanged. The next section presents simulation results with a uniform strong guide field ($B_g/B_0 = 0.5$) applied throughout the entire simulation domain.

2.3.2 Strong-Guide-Field Case

Figure 2.5 shows the structure of the lower current sheet in the simulation with an initial guide field $B_g/B_0 = 0.5$. During the early phase of reconnection, shown in panel (a), enhanced out-of-plane

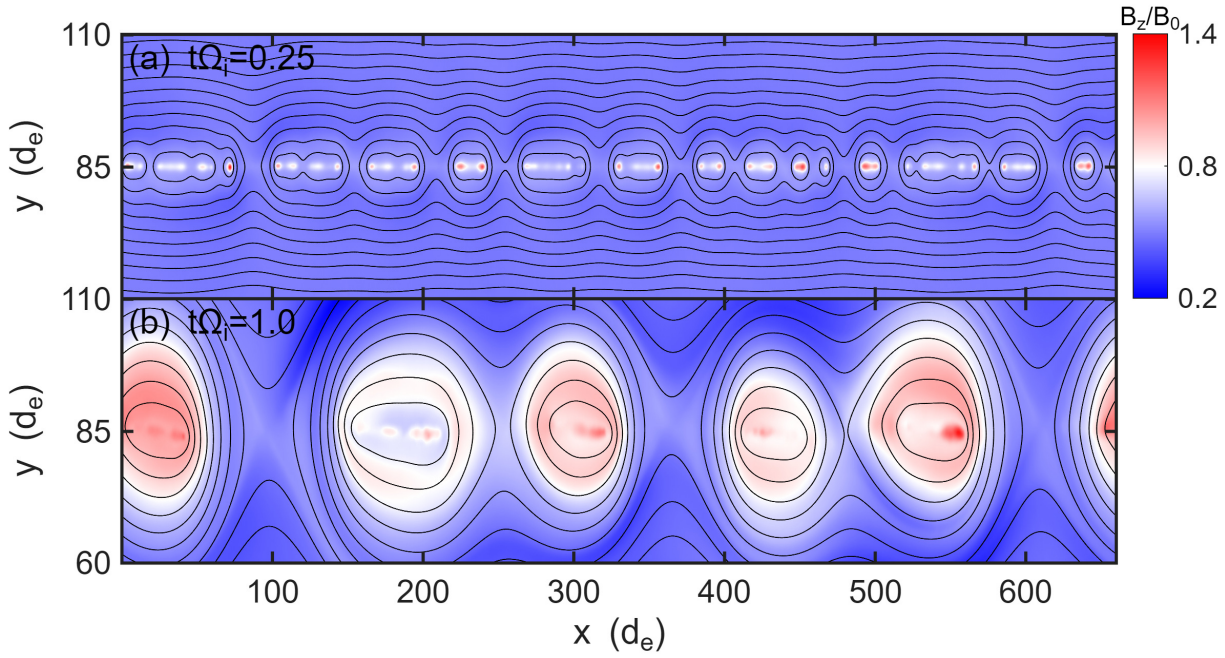


Figure 2.5: The lower current sheet at (a) $t\Omega_i = 0.25$ and (b) $t\Omega_i = 1$ in a simulation with an initial guide field $B_g/B_0 = 0.5$. Black contours denote magnetic field lines, and the color scale shows the out-of-plane magnetic field B_z/B_0.

magnetic fields appear inside the magnetic islands. This enhancement is strongest near the ends of the island, with amplitudes reaching $B_z/B_0 \sim 1$. These B_z enhancements are unidirectional and aligned with the initial guide field. The enhanced out-of-plane magnetic-field structures are generated by the flux-rope separatrix currents and electron Kelvin–Helmholtz instability.

At the end of the simulation, shown in panel (b), island merging produces larger magnetic islands with sizes of $\sim 2\,d_i$ in the x direction. The islands are also significantly broadened in the y direction, extending well beyond the initial current-sheet width. The resulting islands exhibit a two-layer structure in B_z, with a localized peak field of $B_z/B_0 \sim 1.4$ at the center and a broader outer region of weaker fields, still exceeding the ambient guide-field strength, with $B_z/B_0 \sim 0.8$. The mechanism that produces these flux rope core fields is discussed later.

Figure 2.6 shows the electron bulk velocity v_{ex} and out-of-plane magnetic field in a representative

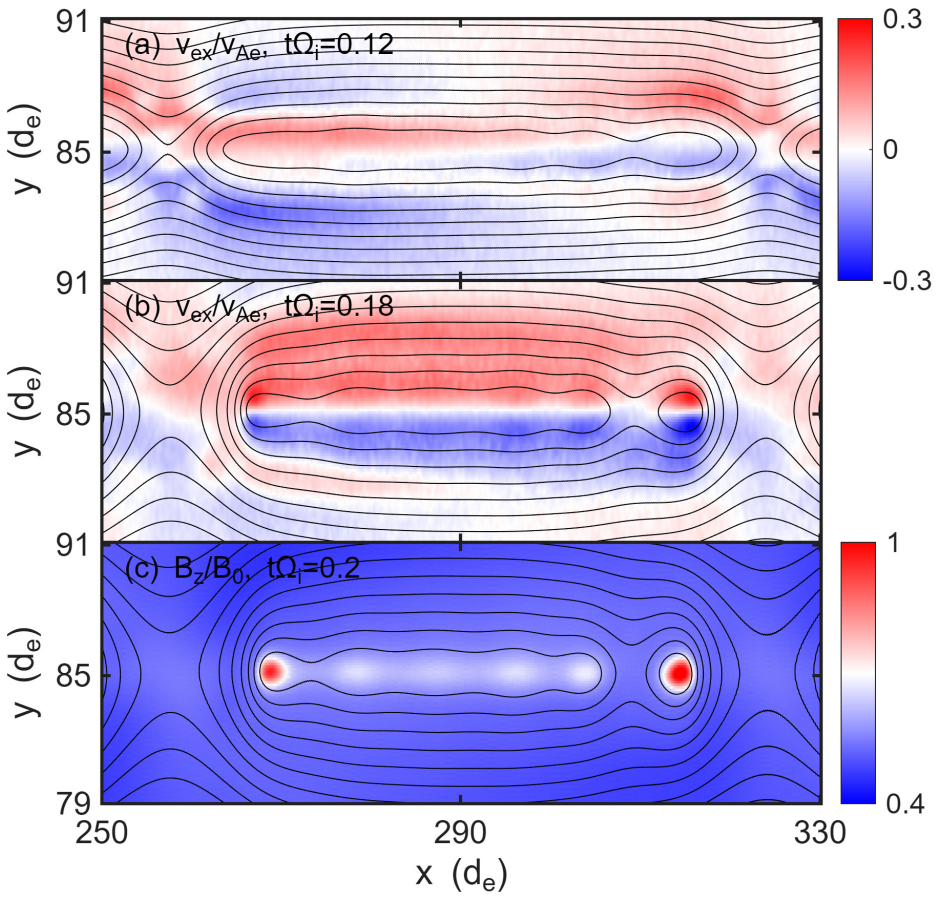


Figure 2.6: Electron bulk flows in the x direction, v_{ex}/v_{Ae}, between two X-lines at (a) $t\Omega_i = 0.12$ and (b) $t\Omega_i = 0.18$. (c) The out-of-plane magnetic field B_z/B_0 distribution at $t\Omega_i = 0.2$.

magnetic island. During the early phase of reconnection, shown in panel (a), electrons originating from the left X-line move in the positive x direction along the upper separatrix, while those from the right X-line move in the negative x direction along the lower separatrix. This deflection produces a velocity shear within the magnetic island, with flow speeds comparable to v_{Ae}. As shown in panel (b), the electrons from the adjacent x-lines combine to form a closed current loop. Near the island center, the velocity shear triggers the electron Kelvin–Helmholtz instability, which fragments the initial current layer. Two dominant current loops form near the two ends of the island, while several

weaker circular currents develop within the island interior. All current loops rotate counterclockwise, generating out-of-plane magnetic fields aligned with the initial guide field. Panel (c) shows the intense B_z generated by these current loops, with the strongest peaks located near the two X-lines and weaker peaks appearing near the island center.

Figure 2.6 corresponds to a case in which the two X-lines are sufficiently separated, allowing the electron Kelvin–Helmholtz instability to fully develop. If the two X-lines are sufficiently close to each other, as in the case shown in Figure 2.5(a) at $x \sim 500\, d_e$, only a single strong B_z peak is formed. It is worth noting that the circular currents generate an out-of-plane magnetic field that enhances the initial guide field at the island center, whereas outside the island the magnetic field associated with these currents is opposite to the guide field, leading to a weaker surrounding guide field so that the net magnetic flux is conserved. These enhanced magnetic-field structures arise from counter-streaming, sheared electron flows and the electron Kelvin–Helmholtz instability, rather than from compression of the ambient guide field.

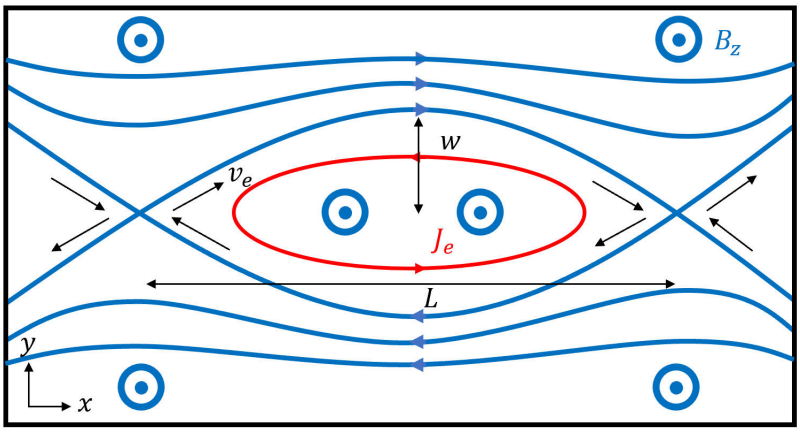


Figure 2.7: Cartoon diagram illustrating how the flux-rope separatrix current enhances the core magnetic field. Blue lines denote magnetic field lines, and the out-of-plane magnetic field B_z is represented by blue circles. Black arrows indicate electron velocities, and red arrows denote the electron current.

In Figure 2.7 we present a schematic illustrating the electron motion within the flux rope and the

associated enhancement of the core magnetic field. The current around the x-line flows into the plane and hence the electrons flow out of the plane and get accelerated by the reconnection electric field. Near the left x-line, and just inside of the flux rope, the magnetic field points out-of-the-plane and towards the x-line near the lower separatrix and out-of-the-plane and away from the x-line near the upper separatrix. Thus, the electrons within the flux rope flow towards the x-line inside the lower separatrix and away from the x-line inside the upper separatrix. These flows near the left x-line combine with corresponding flows at the right x-line to form a closed current loop inside the island. We refer to this current loop as the flux-rope separatrix current. The resulting current generates an out-of-plane magnetic field aligned with the guide field, thereby enhancing the magnetic field in the island core. The enhancement in the guide field is boosted in the present simulations because of the realistic mass ratio. The electron separatrix flows are comparable in magnitude to the electron Alfvén speed, as can be seen in Figure 2.6. The time separation between Figures 2.6(a) and (b) is only $0.06\Omega_i^{-1}$. Even during this short time interval the electron currents localized around the two adjacent x-lines were able to combine into a single current loop within the flux rope.

We can also estimate the condition under which the separatrix-current mechanism can operate. The basic geometry is shown in the sketch in Figure 2.7. The key question is whether the separatrix current can close to form a current loop within the island as the island grows. The time for the separatrix current to travel from an X-line to an adjacent X-line a distance L away is $t_1 \sim L/v_{Ae}$, where v_{Ae} is the characteristic velocity of electrons on separatrices. The growth time of an island is $t_2 \sim w/0.1v_{Ai}$, where the characteristic reconnection rate is $0.1v_{Ai}$ and w is the island width. Requiring the current to traverse the island in a time that is less than the characteristic island growth time implies that $t_1 < t_2$, which yields the condition $L < 10w\sqrt{m_i/m_e}$. This condition suggests that the separatrix currents can close to enhance the core magnetic field even in very large islands.

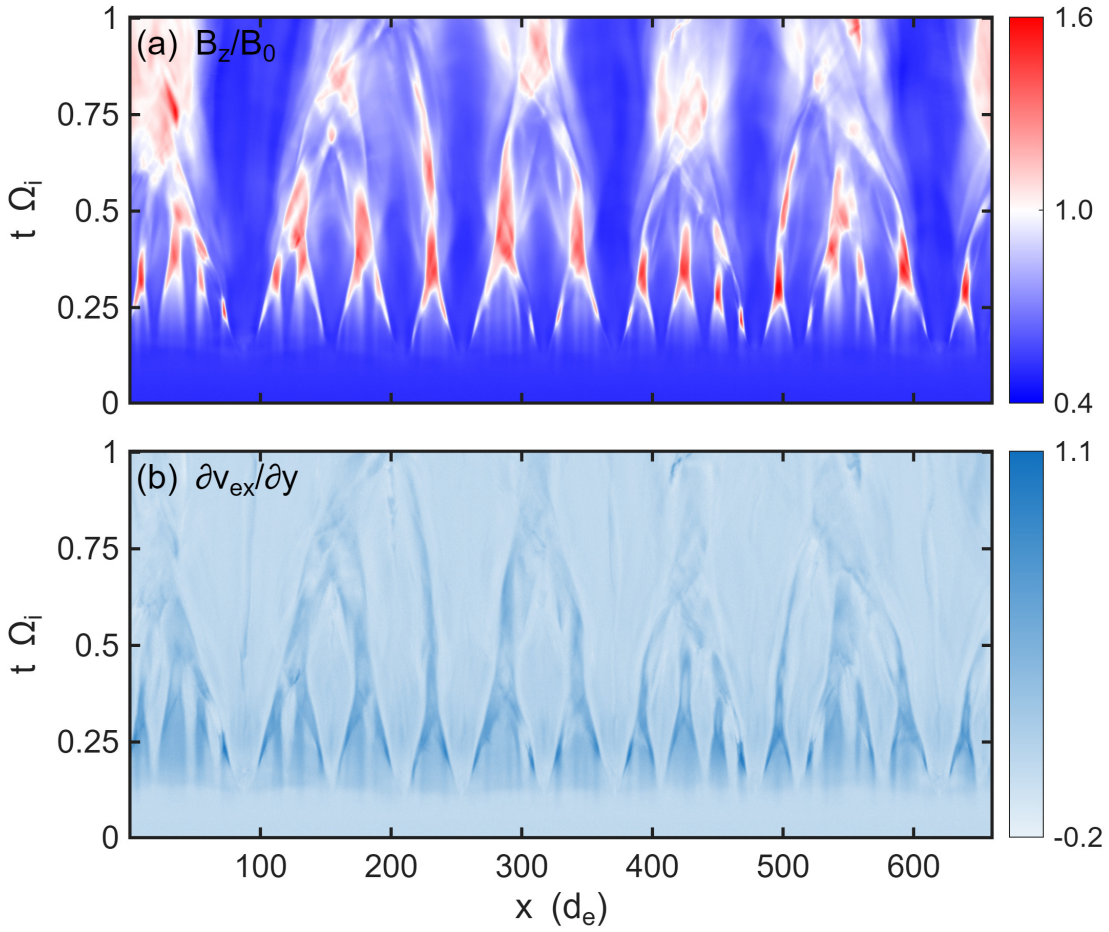


Figure 2.8: Space—time plot of the out-of-plane magnetic field B_z/B_0 and $\partial v_{ex}/\partial y$ at the center of the lower current sheet with guide field $B_g/B_0 = 0.5$. The quantity $\partial v_{ex}/\partial y$ is normalized by v_{Ae}/d_e and is a measure of the sheared electron flow in the core of the islands.

Figure 2.8 shows the space–time evolution of the out-of-plane magnetic field B_z and the electron current gradient $\partial v_{ex}/\partial y$ at the center of the lower current sheet. The quantity $\partial v_{ex}/\partial y$ measures the velocity shear across the current sheet and is calculated by averaging the slope near the current-sheet center. A clear one-to-one correspondence between B_z and the current gradient is observed, indicating that the enhancements of the out-of-plane magnetic field are produced by the electron velocity shears. The electron temperature anisotropy (not shown) is reduced in this case because the guide field suppresses reconnection-driven electron energization [234–236]. Despite the weaker

temperature anisotropy, the peak B_z is significantly enhanced compared with the zero-guide-field case, reaching values approximately three times larger than the initial guide-field strength. The space–time plot further indicates that the dominant growth of B_z occurs during island-merging events starting from $t\Omega_i \approx 0.3$. After $t\Omega_i \approx 0.7$, the out-of-plane magnetic field saturates and remains largely stable at a level of $B_z/B_0 \sim 1$.

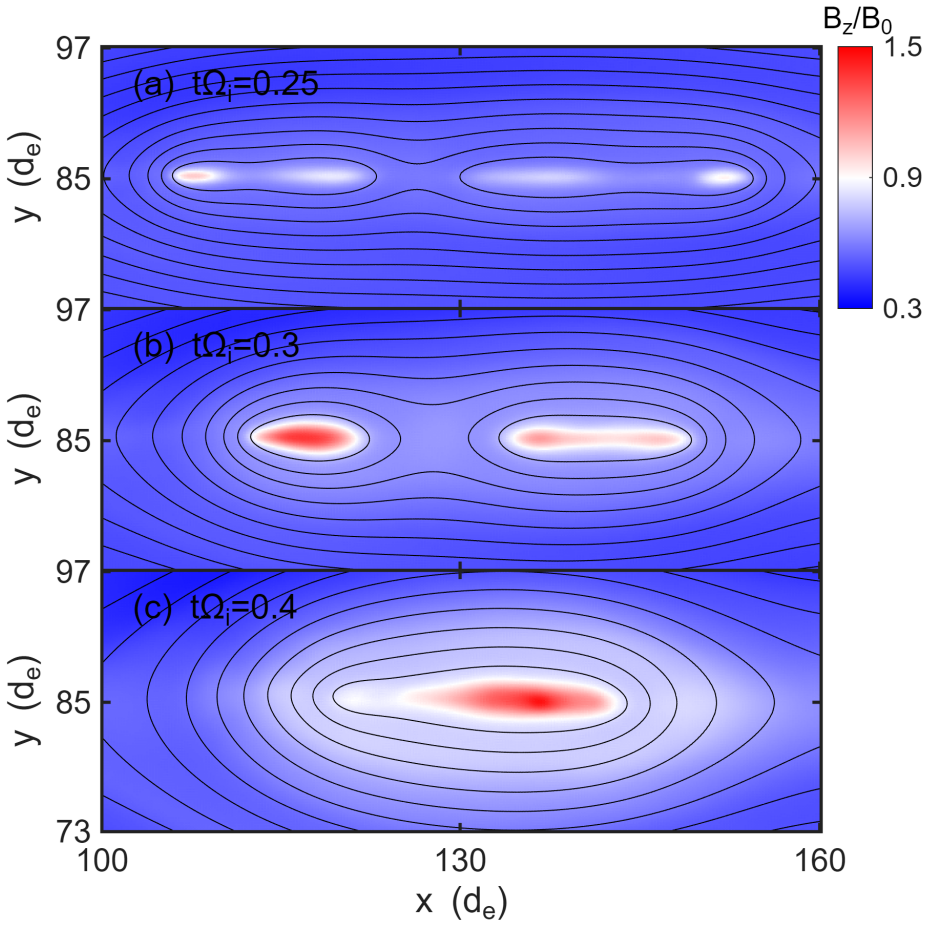


Figure 2.9: Magnetic island merging with an initial guide field $B_g/B_0 = 0.5$. Black contours denote magnetic field lines, and the color scale shows the out-of-plane magnetic field B_z/B_0.

Figure 2.9 shows an example of magnetic-island merging in the presence of a guide field. From panel (a) to panel (b), the two islands contract in the x direction, accompanied by a progressive increase

in the out-of-plane magnetic field B_z. From panel (b) to panel (c), the two islands merge into a single larger island, and the amplitude of B_z reaches values of approximately $1.5\,B_0$.

An important question is whether the enhancement of B_z in the simulation results from either separatrix currents or compression, a topic that has been discussed in the past [70, 99–102]. In Figure 2.10, we present the relationship between B_z and electron density before and after island merging. If compression controlled the enhancement in B_z, the plasma density and B_z should increase by comparable amounts. The data clearly reveals that the electron density does not increase by an amount that is comparable to the enhancement of the out-of-plane magnetic field. In addition, calculations of $\boldsymbol{\nabla}\cdot\mathbf{v}$ do not show a significant compression during island growth and merging. We therefore emphasize that the strong enhancement of B_z observed here is not simply a consequence of compression of flux ropes as suggested in earlier studies [70, 99–102], but rather results from the generation of electron separatrix currents.

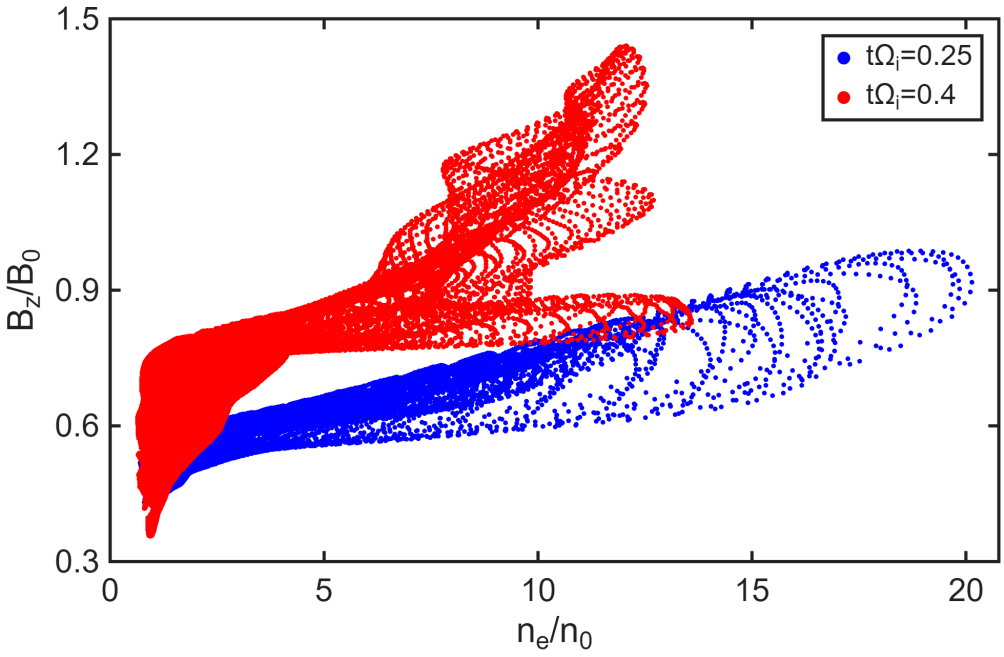


Figure 2.10: Scatter plot of electron density versus B_z corresponding to panels (a) and (c) of Figure 2.9. Data points are sampled from the entire panels and smoothed.

From a theoretical perspective, the magnetic flux B_z within a flux rope is conserved in a collisionless system. This can be demonstrated by integrating the z-component of Faraday's law of induction along any closed magnetic field line within the flux rope, which shows that the rate of change of the enclosed flux is given by the line integral of the parallel electric field along the field line. During reconnection, the parallel electric field is nonzero primarily near X-lines and along separatrices connected to them, but is essentially negligible within the interior of flux ropes, so the enclosed B_z flux remains approximately constant. Consequently, when two magnetic islands merge into a single flux rope, the total B_z flux in the final structure is equal to the sum of the fluxes of the initial islands, a result that again follows directly from Faraday's law of induction.

2.4 Discussion and Conclusions

We performed two-dimensional particle-in-cell simulations with a realistic ion–electron mass ratio to investigate the formation of out-of-plane magnetic field inside flux ropes/magnetic islands during reconnection. In the absence of a guide field, strong temperature anisotropy develops in the reconnection exhaust and triggers the Weibel instability, which generates bipolar out-of-plane magnetic fields along the current sheet within the magnetic islands. In contrast, when a strong guide field is present, the electron outflows are deflected by the guide field to form flux-rope separatrix currents, a circular current loop wrapping the flux rope, which generates an out-of-plane magnetic field that reinforces the initial guide field. The extended sheared flow near the center of the flux rope becomes unstable to the electron Kelvin–Helmholtz instability, leading to the formation of localized rings of electron current and associated regions of enhanced magnetic field B_z. Island merging further helps to sustain and, in some cases, amplify the core magnetic field. These self-generated magnetic-

field structures constitute an important element of reconnection dynamics and are expected to play a key role in scattering energetic electrons during reconnection.

The rate of reconnection-driven particle acceleration, which is dominated by Fermi reflection, is proportional to a particle's velocity parallel to the magnetic field. Consequently, scattering processes that transfer energy from the parallel to the perpendicular direction can modify reconnection-driven energy gain. In our simulations, the instability-driven out-of-plane magnetic fields strongly scatter the electron outflows, leading to a substantial increase in the perpendicular velocity. Such scattering is therefore expected to inhibit the energy gain during island merging.

Although this paper focuses primarily on two limiting cases, $B_g = 0$ and $B_g/B_0 = 0.5$, we also performed a series of simulations with intermediate guide-field strengths. In all cases, we observed the growth of strong out-of-plane magnetic fields B_z near the centers of magnetic islands. As discussed previously, the dominant mechanism responsible for B_z generation is the Weibel instability for $B_g = 0$, whereas the flux-rope separatrix currents and electron Kelvin–Helmholtz instability dominate for $B_g/B_0 = 0.5$. A key difference between these two cases is the direction of the enhanced out-of-plane magnetic field (see Figures 2.2(a) and 2.5(a)), which is rooted in the direction of the electron current (see Figures 2.2(b) and 2.6(b)). The transition between these two regimes is not sharp. For intermediate and weak guide-field strengths (e.g., $B_g/B_0 \sim 0.2$), the guide field acts as a perturbation to the electron outflow, and both mechanisms appear to operate simultaneously. These results suggest that the development of a strong peak in B_z within magnetic islands is a universal feature of magnetic reconnection. Such features provide valuable insight into the structure of electron-scale outflows and are signatures of the electron scattering that occurs when accelerated particles are ejected into growing magnetic islands.

Magnetic flux tubes are frequently observed to possess strong core magnetic fields that are

comparable to, or even exceed, the strength of the ambient guide field [78–82]. Traditionally, the enhancement of the core magnetic field has been interpreted as a consequence of flux-tube compression associated with the loss or evacuation of internal plasma [70, 99–102]. These interpretations are primarily based on magnetohydrodynamic or hybrid simulations, which do not fully capture electron-scale dynamics or the effects of kinetic micro-instabilities. In contrast, our PIC simulations, enabled by the use of the realistic proton-to-electron mass ratio, explicitly resolve electron dynamics and reveal the importance of electron-scale processes in generating and sustaining strong core magnetic fields. These results provide a new perspective on the origin of enhanced core fields in flux ropes and suggest that kinetic effects may play a more significant role than previously recognized.

We further suggest that this core-field self-generation mechanism may also operate in flux ropes in other astrophysical environments. In the solar corona, flux ropes are frequently observed in current layers during solar flares and coronal mass ejections [83, 86, 92]. Flux rope merger is the dominant mechanism for particle acceleration during reconnection [16, 232, 237, 238]. It is now also well established from simulations that a strong guide field suppresses particle energy gain by weakening Fermi reflection [16,41]. Thus, a mechanism that enhances the guide magnetic field in the cores of the flux ropes produced during reconnection will suppress particle energy gain during flare energy release.

Recent data from the Parker Solar Probe revealed multiple reconnecting current sheets embedded within the reconnection exhaust of a large-scale heliospheric current sheet (HCS) [94]. These current sheets exhibit clear signatures of reconnection and have been interpreted as merging flux ropes. The small magnetic shear angles (27°–81°) in these merging events indicated that the guide fields at the merging sites were much greater than the ambient guide field upstream of the main exhaust. The enhancement of the out-of-plane magnetic field in the HCS has been interpreted as arising from compression within magnetic flux ropes. Our proposed mechanism suggests an alternative origin for

this enhancement of the guide magnetic field.

One important consideration for observations is that a flux rope can propagate after its formation [239, 240]. A flux rope may form in a region with a finite guide field and subsequently move into a location with little or no guide field. Therefore, the strength of the ambient guide field outside the flux rope should not necessarily be interpreted as the guide field experienced during its formation. In addition, as shown in Figures 2.2(a) and 2.5(a), there are valleys between adjacent magnetic-field peaks. If a spacecraft trajectory passes through such a valley, it may not detect a strong out-of-plane magnetic field even though a significant guide field might be present at another location within the flux rope. These factors should be taken into careful consideration when comparing simulation results with observations.

The initial current sheet width used in these simulations is relatively narrow, on the order of d_e. In space plasmas, the current sheet thickness can vary substantially and a width of $\sim d_e$ represents the lower bound inferred from magnetotail observations [81, 241–243]. However, as shown in Figures 2.4 and 2.5, the magnetic islands significantly broaden at later times, reaching widths of order d_i for which proton dynamics become important. Even in these larger scale flux ropes the enhancement of the out-of-plane magnetic field remains pronounced. We also tested a case with an initial current sheet width of $2d_e$, with the result being a delayed reconnection onset and a weaker, but still significant, core field.

Chapter 3: Wave Generation and Energetic Electron Scattering in Solar Flares

3.1 Background

As discussed in Section 1.3, observations of above-the-looptop hard X-ray sources and microwave gyrosynchrotron emissions, together with theoretical estimates, indicate that energetic electrons are not simply accelerated and then allowed to escape freely along coronal magnetic fields [51, 57, 142]. Instead, some combination of trapping and scattering must operate to reduce electron transport and sustain a substantial population of energetic electrons in the coronal source region.

Among the candidate mechanisms, wave–particle interactions driven by kinetic instabilities are particularly attractive. Reconnection energization naturally produces strongly anisotropic electron distributions with $T_{\parallel} > T_{\perp}$. Such distributions contain free energy that can drive oblique whistler waves, which scatter electrons in pitch angle, isotropize distribution and inhibit heat flux [172, 244, 245]. Previous studies have demonstrated that flare-like electron populations can self-generate strong whistler turbulence and undergo substantial pitch-angle scattering [172]. At the same time, several important questions remain open. The long-term evolution of the turbulence under continuous heat-flux driving remains poorly understood. In particular, it is unclear what the key parameters are that control wave growth and scattering efficiency.

In this chapter, we investigate the generation of oblique whistler waves by anisotropic flare-driven electron distributions and their role in regulating energetic-electron transport. Using 2D PIC simulations, we examine how a continuously driven heat flux excites oblique whistler waves and Weibel-like instabilities, how these fluctuations scatter electrons and suppress the heat flux, and how the resulting transport inhibition depends on plasma parameters. We derive a scaling for the scattering rate and assess the influence of the heat-flux-carrying population density. These results provide a

framework for evaluating whether self-generated turbulence can explain the confinement of energetic electrons inferred from observations.

3.2 Simulation Setup

3.2.1 Initial Distribution

There is an initial uniform magnetic field $\mathbf{B} = B_0\hat{\mathbf{y}}$ threading the plasma, so that the y direction is regarded as the parallel direction and x and z are the perpendicular directions. The initial electron distribution function represents a reconnection-driven energetic electron heat flux and consists of two components. The first component is a bi-kappa distribution with a heat flux in the positive v_y direction:

$$f_\kappa\left(v_\parallel, v_\perp\right) = \frac{n_0}{\left(\pi\kappa\right)^{3/2}\theta_\parallel\theta_\perp^2}\frac{\Gamma\left(\kappa+1\right)}{\Gamma\left(\kappa-\frac{1}{2}\right)}\left[1+\frac{v_\parallel^2}{\kappa\theta_\parallel^2}+\frac{v_\perp^2}{\kappa\theta_\perp^2}\right]^{-(\kappa+1)}\Theta\left(v_\parallel\right) \tag{3.1}$$

where n_0 is the electron density, Γ is the gamma function, κ is a parameter that tunes the steepness of the nonthermal tail of the distribution, and $\theta_n^2 = v_{th,n}^2\left(\kappa-3/2\right)/\kappa$ is the effective thermal speed, where $v_{th,n}^2 = 2T_n/m_e$ is the regular thermal speed, T_n is the temperature in the n-direction, m_e is the electron mass and $\Theta\left(v_\parallel\right)$ is the Heaviside step function.

The second component is a drifting Maxwellian distribution that represents the cold return current beam (moving against B_0)

$$f_M\left(v_\parallel, v_\perp\right) = \frac{n_0}{\pi^{3/2}v_T^3\left[1+\mathrm{erf}(v_b/v_c)\right]}\exp\left\{-\left[\left(v_\parallel+v_b\right)^2+v_\perp^2\right]/v_c^2\right\}\Theta\left(-v_\parallel\right) \tag{3.2}$$

where $v_c^2 = 2T_c/m_e$ is the cold thermal speed, v_b is a beam drift speed that ensures initial zero current,

and the error function $\mathrm{erf}(v_b/v_c)$ makes the density of hot and cold particles equal.

For parameters, we chose κ = 4, $T_y = 20T_c = 40T_x$, $v_{th,y}/v_{Ae} = \sqrt{2}$, $c/v_{Ae} = 5$, $\beta_y = 8\pi n_0 T_y/B_0^2$ = 2. The simulation domain lengths are $L_y = 163.84\, d_e$ and $L_x = L_y/4$, where $d_e = c/\omega_{pe}$ is the electron skin depth, and $\omega_{pe} = (4\pi n_0 e^2/m_e)^{1/2}$ is the electron plasma frequency. The simulation time step is $dt = 0.008\Omega_e^{-1}$, where $\Omega_e = eB_0/m_e c$ is the electron cyclotron frequency. Ions are initialized with a Maxwellian distribution of temperature $T_i = T_c$, and do not play an important role due to the large mass ratio m_i/m_e = 1600. The simulation uses 560 particles per species per cell and has a grid of 1024 by 4096 cells.

This distribution choice is motivated by flare observations [51–55] that suggest a power-law distribution of nonthermal electrons in the energy-release and electron acceleration region. It is worth emphasizing that, despite half of the initial distribution being modeled as a kappa distribution, the nonthermal population represents only a minor fraction of the kappa, and hence the overall, distribution. The fraction of nonthermal particles is explicitly calculated following Eq. (3.3).

While this is a relatively high β for the corona, specific flare observations show a hard X-ray source β of approximately 1 [51]. Recent simulation results also demonstrate that magnetic reconnection can drive the outflow to a marginal firehose state in which $\beta_\parallel - \beta_\perp \approx 2$ [16]. When the high energy tail of an anisotropic kappa distribution with $\kappa = 4$ is scattered to an isotropic one, particle number conservation implies the resulting energy spectral index will be 4.5 because the isotropic distribution occupies a larger phase space ($E^{0.5}$) than the anisotropic one ($E^{-0.5}$). This value is consistent with the results of a statistical study of flare parameters, which found that the spectral index value is around 4 based on a single power law fit [53]. Additionally, the large value of $T_\parallel/T_\perp$ is motivated by 3D PIC simulations of reconnection showing $P_\parallel/P_\perp$ approximately equal to 100 [246].

To determine the nonthermal β, we separate the kappa distribution into a combination of a

Maxwellian component and a nonthermal component, where the temperature of the Maxwellian component (T_M) is related to the kappa distribution temperature (T_κ) by the equation $T_M = (\kappa - 1.5)\, T_\kappa/\kappa$ [52]. [52] define the number density of the Maxwellian component (N_M) by requiring it to match the differential flux of the kappa distribution at energy T_M. The result is

$$N_M = n_0 \exp(1) \left(\frac{1}{\kappa}\right)^{\frac{3}{2}} \frac{\Gamma(\kappa+1)}{\Gamma\left(\kappa - \frac{1}{2}\right)} \left[1 + \frac{1}{\kappa}\right]^{-(\kappa+1)} \tag{3.3}$$

The density of the nonthermal component for the parameters under consideration can be calculated as $N_{NT} \approx 0.2 n_0$. The nonthermal energy density is calculated with the energy relation $n_0 T_\kappa = N_M T_M + N_{NT} T_{NT}$ with $T_\kappa \approx T_\parallel/3$. The resulting nonthermal beta is 0.17, which is slightly larger than the observed value of around 0.1 near the flare looptop [59], but quite close to the 0.16 of another observation [247].

3.2.2 Boundary Condition

Due to the initial distribution function (the total of equations (3.1) and (3.2)), the heat flux moves upwards in the box while a cold return current moves downwards. We set a boundary source to continuously inject heat flux into the system in order to drive the system to a steady state. Electrons that encounter the top boundary are reinjected at the bottom of the box with random positions and new velocities that satisfy the kappa flux distribution

$$f_{\kappa f}\left(v_\parallel, v_\perp\right) = \frac{2(\kappa-1)}{\pi\kappa\left(\theta_\parallel \theta_\perp\right)^2} v_\parallel \left[1 + \frac{v_\parallel^2}{\kappa\theta_\parallel^2} + \frac{v_\perp^2}{\kappa\theta_\perp^2}\right]^{-(\kappa+1)} \Theta\left(v_\parallel\right) \tag{3.4}$$

where θ_n^2 and other parameters are the same as the initial kappa distribution in Eq. (3.1). The kappa flux distribution models particles escaping from a source. Similarly, when electrons hit the bottom

boundary, they are re-injected at the top of the box with random positions and new velocities that satisfy the drift Maxwellian distribution with identical parameters as in the initial distribution. The boundary condition in the x direction is periodic and ions, which are essentially only a charge-neutralizing background, simply follow periodic boundary conditions in all directions. The electromagnetic boundary conditions are set to be periodic in both the parallel and perpendicular directions.

The ratio v_d/v_{Ae}, with v_d the heat flux drift speed, here defined as the mean parallel speed of the heat flux (see equations 3.1 and 3.4), is expected to be a key parameter controlling the degree to which the electron distribution is in resonance with the excited waves. In the simulations presented here we vary this parameter by changing the density n_0.

3.3 Simulation Results

3.3.1 Wave Excitation

The initial distribution drives magnetic fluctuations unstable in the system. Figure 3.1 shows the box-averaged magnetic field fluctuation $\langle B_z^2 \rangle$ versus time for different values of v_d/v_{Ae}, where v_d is the mean parallel drift speed of the heat flux (Eq. (3.1)). The magnetic fluctuations grow rapidly, reach a peak value and, after a short decay, again grow slowly until flattening to a steady state at late time. The magnetic fluctuations reach larger amplitude for higher drift speeds, where more electrons have a velocity greater than the whistler phase speed and are therefore able to drive the waves.

In Figure 3.2 we show the structure of the out-of-plane magnetic fluctuations and corresponding space–time plot for $v_d/v_{Ae} = 1.06$. Shown in Fig. 3.2(a) is the growth phase when the large anisotropy of the initial distribution excites the Weibel and produces filaments that fill the box along the heat flux direction. The spacing of these filaments along the y direction is around d_e. The magnetic structure

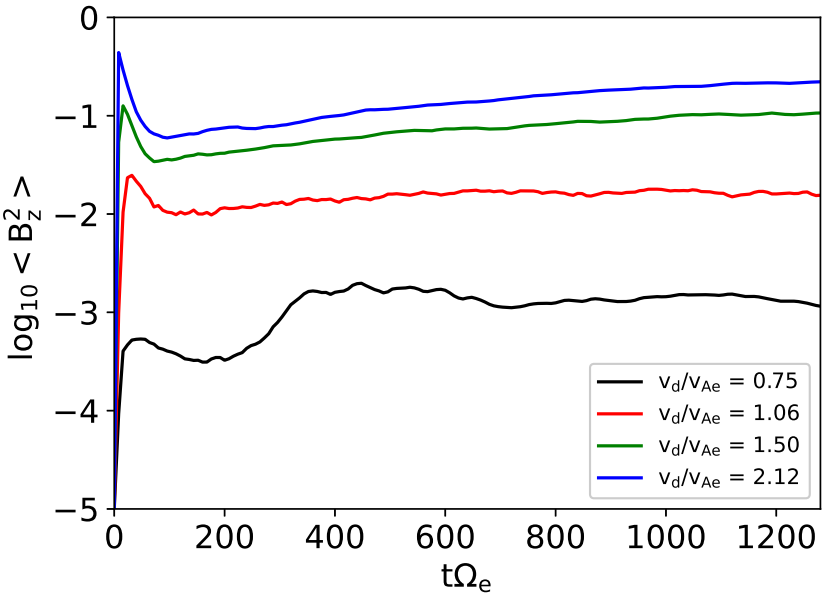


Figure 3.1: The evolution of the box-averaged out-of-plane magnetic field fluctuations for different cases of v_d/v_{Ae}, where v_d is the mean parallel drift speed of the heat flux and v_{Ae} is the electron Alfvén speed.

of these filaments, with the wavevector $\mathbf{k}$ transverse to $\mathbf{B}$ and the magnetic perturbation dominantly in the z direction, matches the expected structure of a Weibel instability that is driven by the strong parallel heat flux. Such Weibel-like structures are soon replaced by larger-amplitude oblique whistler waves that propagate at angles of roughly 70° from the parallel direction, as shown in Figure 3.2(b). The whistlers are excited by the fan instability, which is driven by the $n = -1$ anomalous cyclotron resonance (see Eq. (1.6)) with the tail of the electron distribution. Figure 3.2(b) corresponds in time to the initial peak in the wave amplitude in Figure 3.1, so the initial peak and subsequent decay phase of the fluctuations should be associated with the drive from the initial distribution function. Figure 3.2(c) is at the time when the red curve in Figure 3.1 begins to flatten. Oblique whistler waves with normal angles around 45° are excited at the bottom of the box by heat flux injection and propagate upward. Filaments oriented along the y direction, which are excited by the Weibel instability, are also observed near the lower boundary; however, they occupy only a limited region near the lower boundary of the

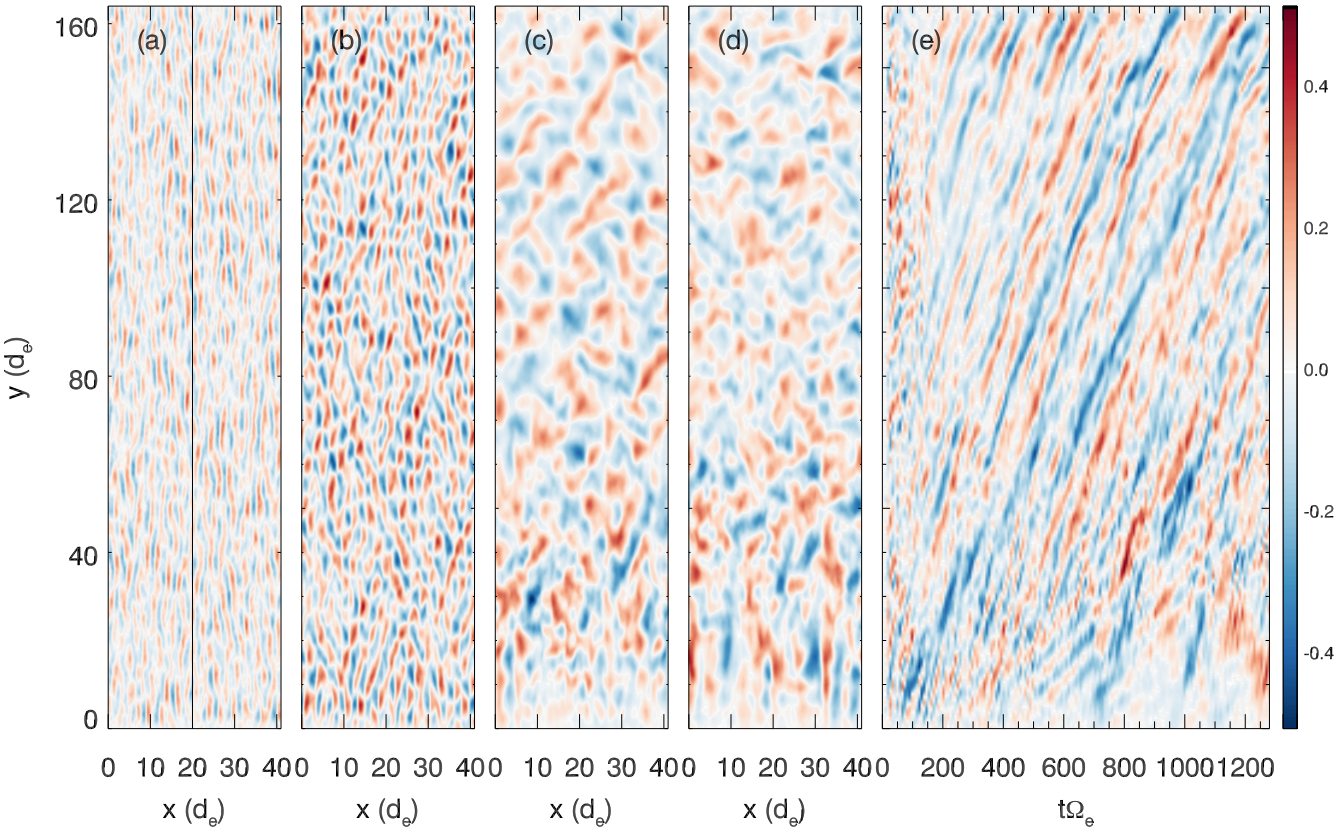


Figure 3.2: For the case with $v_d/v_{Ae} = 1.06$ two dimensional plots of the out-of-plane magnetic field B_z at (a) $t\Omega_e = 15$, (b) $t\Omega_e = 30$, (c) $t\Omega_e = 500$. and (d) $t\Omega_e = 1200$. Shown in (e) is the space–time diagram $(t - y)$ of B_z. The black line in (a) is where the space–time plot data shown in panel (e) is taken.

simulation domain. Figure 3.2(d) is taken at the end of the simulation and appears similar to panel (c), showing that the system has reached a steady state.

Shown in Fig. 3.2(e) is a space–time plot of B_z, where the data are collected from a strip extending over the entire y range of the domain at a fixed x position (vertical black line in Figure 3.2(a)). The initial peak-and-decay phase of the magnetic field fluctuation appears as a transient period before $t\Omega_e$ = 100, after which upward-moving whistler waves appear throughout the entire box. After around $t\Omega_e$ = 100, the bottom boundary continuously generates upward-moving whistler waves, showing that the instability from heat flux injection is responsible for the fluctuations at late

time. The phase speed of the whistler waves remains nearly constant across most of the domain at approximately $0.16v_{Ae}$, representing a substantial fraction of the electron Alfvén speed. According to the dispersion relation (Eq. 1.5), the maximum phase speed is $0.5v_{Ae}$.

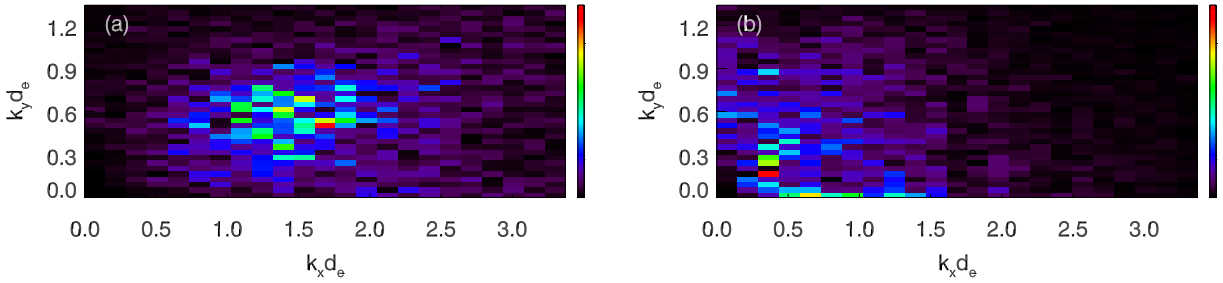


Figure 3.3: Power spectrum of the out-of-plane magnetic field B_z from the simulation in Figure 3.2 at: (a) $t\Omega_e = 30$ (see Fig. 3.2(b)); and (b) $t\Omega_e = 1200$ (see Fig. 3.2(d)).

Figure 3.3 shows the power spectrum of the out-of-plane magnetic field for the simulation shown in Fig. 3.2. Figure 3.3(a) corresponds to the oblique whistler waves induced by the initial distribution (see Fig. 3.2(b)), exhibits peaks around $k_x d_e \sim 1.5$ and $k_y d_e \sim 0.6$, and shows power extending over a broad range of wave numbers. The wave normal angle for the highest-amplitude mode is around 70°, but the range of wave numbers indicates the coexistence of several oblique waves with slightly different phase speeds. The parallel phase speed $\sim 0.5V_{Ae}$ measured in Figure 3.2(b) corresponds to $kd_e \sim 1$ from the dispersion relation of Eq. (1.4), a value consistent with the power spectrum in Fig. 3.3(a). In the steady state, there are two peaks in the power spectrum, as shown in Figure 3.3(b). One is the oblique mode centered around $k_x d_e \sim 0.3$ and $k_y d_e \sim 0.2$, which corresponds to the oblique whistler wave. The other is a perpendicular mode centered around $k_x d_e \sim 0.6$ and $k_y d_e = 0$, which arises from the filaments appearing near the bottom boundary of Figure 3.2(d). The parallel phase speed $\sim 0.2V_{Ae}$ measured at the end of the simulation gives $kd_e \sim 0.1$ from the dispersion relation of Eq. (1.4), which is consistent with Figure 3.3(b).

3.3.2 Whistler Wave Scattering

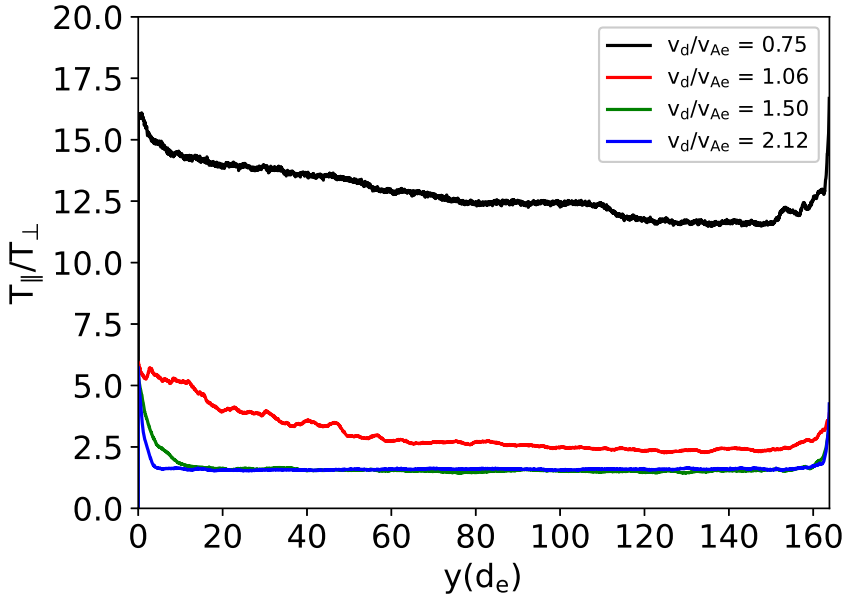


Figure 3.4: Ratio of the parallel electron temperature T_{eyy} to the perpendicular temperature $(T_{exx} + T_{ezz})/2$ of the total distribution at the end of the simulation for different values of v_d/v_{Ae}, where v_d is the mean parallel drift speed of the heat flux and v_{Ae} is the electron Alfvén speed.

Figure 3.4 shows the temperature anisotropy averaged over x versus distance y at the end of the simulations for different drift speeds. The higher drift speed cases (red, green and blue curves) exhibit roughly the same anisotropy at $y = 0$ as the systems have lost all information regarding the $t = 0$ initial conditions, while the slower drift speed case (black curve) is still affected by the initial distribution due to the weakness of the scattering. As a result, the anisotropy remains large. For higher drift speeds (green and blue curves), the temperature anisotropy decreases quickly with distance from the boundary and reaches a minimum value around 1.5. The final distribution is more isotropic at larger value of y because the injected electrons must propagate some distance into the domain before the waves are able to isotropize them. For the slower drift speed case (black curve), the anisotropy remains large due to the small amplitude of the waves, resulting in a correspondingly weak level of

scattering.

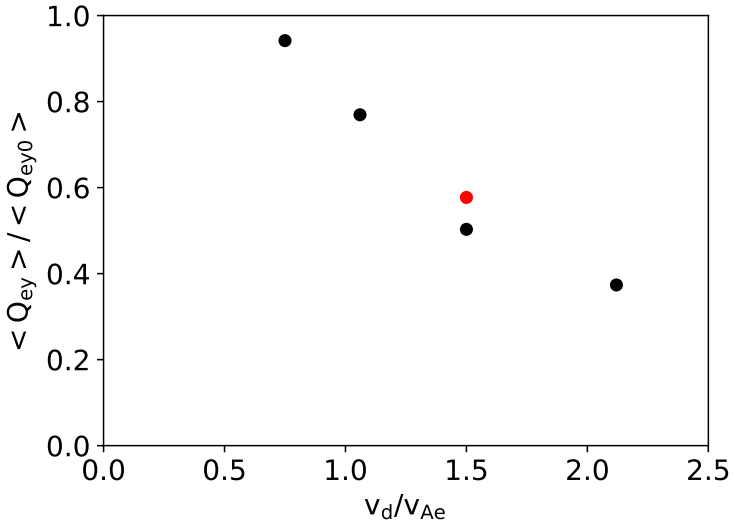


Figure 3.5: Ratio of final to initial y-directed average heat flux for different values of v_d/v_{Ae}, where v_d is the mean parallel drift speed of the heat flux and v_{Ae} is the electron Alfvén speed. The red point corresponds to a case in which 25% of electrons, rather than 50%, are found in the kappa distribution (Eq. (3.1)) at $t = 0$, while the remaining 75% are in the drifting Maxwellian distribution (Eq. (3.2)).

Shown in Figure 3.5 is the ratio of the final to initial average y-directed heat flux for different drift speeds. The red point corresponds to a case where 25% of electrons, rather than 50%, initially satisfy the kappa distribution (Eq. (3.1)), while the remaining 75% are from the drifting Maxwellian distribution (Eq. 3.2)). In this case, all other distribution function parameters remain unaltered, with the exception of a reduction in the drift speed (see Eq. 3.2) that is necessary for current balance. In this case the density of nonthermal electrons carrying the heat flux is significantly reduced [52, 53, 128]. The heat flux at steady state decreases with increasing drift speed, reaching a minimum value around 40% of the initial heat flux for the highest drift speed. Notably, the reduced kappa density case (red point) does not significantly impact the reduction of the heat flux.

The electron velocity-space distribution functions of Fig. 3.6 demonstrate the impact of the scattering of electrons by the wave activity. Shown in panels (a-c) are distributions from the end of

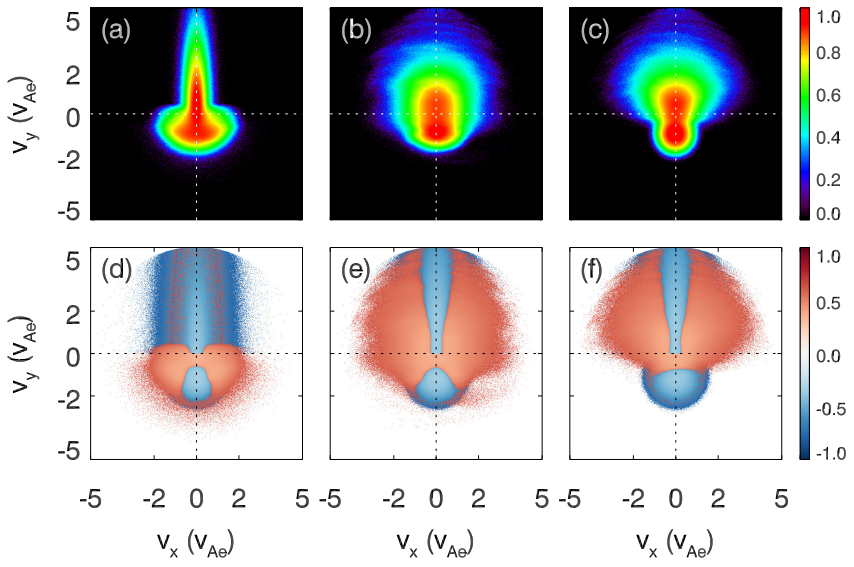


Figure 3.6: Electron distribution functions in $v_x - v_y$ phase space at the end of the simulation of Figure 3.2 at different y positions in the box. The sampling area of each position is the entire x range and 1% of the total y range. Shown in panels (a-c) are the electron velocity distribution functions on a logarithmic scale near the bottom, middle and top of the box, corresponding to positions at 0%, 80% and 99% of the total y range, respectively. Panels (d-f) are comparisons to the initial distribution, $\log\left(|f_{end} - f_{ini}|\right) \mathrm{sgn}\left(f_{end} - f_{ini}\right)$, at the same positions, where sgn is the sign function.

simulation at different positions in the box. Figure 3.6(a), from the bottom of the simulation domain, is a kappa-like distribution in the upper half of the panel because of heat flux injection at the bottom boundary. The return current in the negative v_y plane is broadened in the v_x direction, due to scattering by whistler waves through the cyclotron resonance. In the upper half of the box, shown in Fig. 3.6(b), the total distribution has become nearly isotropic. The upward moving electrons have been strongly scattered. There is no obvious horn-like structure, which is likely a consequence of the overlap of several resonance circles [189] and is implied by the broad range of wave numbers shown in Figure 3.3. At the top of the box, panel (c), the cold current injection from the top boundary produces a beam feature in the negative v_y component, while the positive v_y distribution is even more isotropic than in panel (b). Panels (d-f) show the difference between the final and initial distributions at the respective

positions. Panel (d) shows that the return current has been heated, and in panels (e,f) the decrease in the parallel heat flux and the significant increase in the perpendicular velocity are direct evidence of the scattering of the nonthermal electrons by whistler waves.

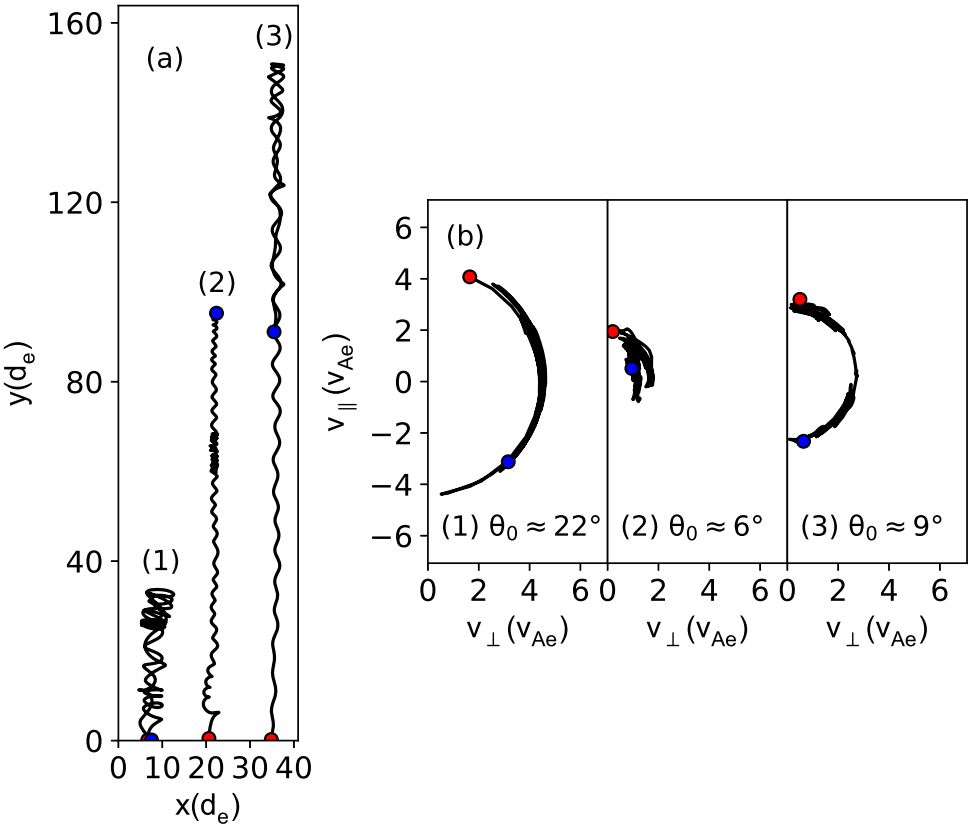


Figure 3.7: (a) Electron trajectories in the $x - y$ plane for the strong drift case with $v_d/v_{Ae} = 2.12$. Three electron trajectories are shown with red dots indicating the starting positions and blue dots the end positions. The trajectories are from the middle of the simulation (around $t\Omega_e = 900$). (b) Electron velocity trajectories correspond to the three cases in panel (a) in $v_\parallel - v_\perp$ space. Red dots indicate the starting positions and blue dots are the end of the trajectories. θ_0 gives the initial pitch angle.

Shown in Fig. 3.7 are the self-consistent trajectories of several electrons in the $x-y$ and $v_\parallel - v_\perp$ planes, extracted from the particle-in-cell simulation with $v_d/v_{Ae} = 1.50$. The electrons all start from the bottom boundary with initial parallel velocities significantly greater than their perpendicular velocities and so are typical of electrons carrying the heat flux. In panel (a), the waves in the system are strong enough to completely reverse the direction of the electrons (they are scattered past 90^o

in pitch angle). In panel (b), the trajectories of case (1) and (3) exhibit diffusion along a nearly complete semi-circle (see Eq. (1.7)) and scatter over 90 degrees in pitch angle, reversing their direction along the ambient magnetic field. The particle in case (2) also scatters past 90 degrees but reveals a more complex trajectory as it moves from a larger to a smaller radius in velocity space. The trajectories demonstrate that the reduction of electron parallel velocity is accompanied by an increase of perpendicular velocity. Thus, the scattering of whistler waves has significant consequences: it directly inhibits the heat flux while at the same time boosting the potential for magnetic trapping by increasing the pitch angle. Both effects will boost the confinement of energetic electrons in flares.

3.3.3 Reduced Number Density Case

Shown in Fig. 3.8 is the structure of the out-of-plane magnetic fluctuations at the end of the simulations for the reduced number density case and the corresponding baseline run (both with $v_d/v_{Ae} = 1.50$). The initial peak and decay phases are similar to Figure 3.4 (a-b) with features such as the initial filament and subsequent oblique whistler mode, and therefore we omit those times here for simplicity. For the case with equal number densities carrying the heat flux and return current in Fig. 3.8(a), the filament structure from the Weibel instability forms at the bottom of the domain and extends upward, threading the entire system. In Fig. 3.8(b), where the number density of electrons carrying the heat flux is reduced, the Weibel instability is weaker and filaments only extend to the middle of the box before they are replaced by oblique whistler waves.

Shown in Fig. 3.9 is the time evolution of the box-averaged magnetic fluctuation energy $\langle B_z^2 \rangle$ for the base case with $v_d/v_{Ae} = 1.50$ and the case with reduced number density carrying the heat flux (corresponding to the red point in Fig. 3.5 and Fig. 3.8 panel (b)). When the initial heat flux is

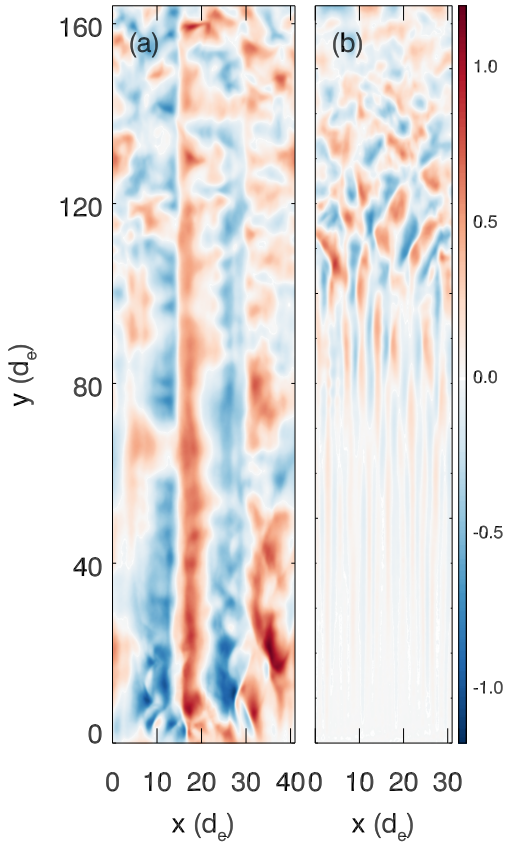


Figure 3.8: Two dimensional plots of the out-of-plane magnetic field B_z at $t\Omega_e = 1280$. In (a) the normal setup with $v_d/v_{Ae} = 1.50$ (as shown in Figs. 3.1 and 3.4) and in (b) the case with the reduced number density carrying the heat flux.

reduced by half (with the same drift speed), the wave energy before $t\Omega_e$ = 400 is small due to the reduced population of electrons available to drive the instability. Eventually the slowly growing waves reach finite amplitude and the fluctuation level flattens around $t\Omega_e$ = 800. The late time value of the wave amplitude is only modestly reduced from that of the base case, demonstrating that strong oblique whistler waves can be excited even when the number density of the electrons carrying the heat flux is reduced.

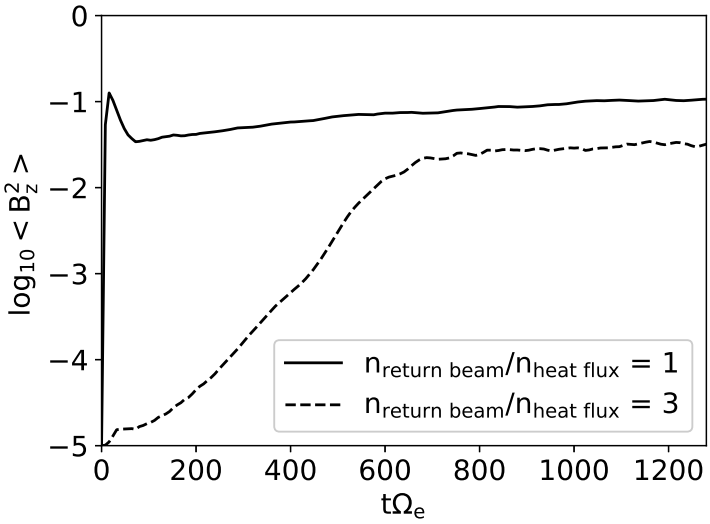


Figure 3.9: Box-averaged out-of-plane magnetic fluctuation amplitude B_z^2 as a function of time for the simulation with the reduced number density of electrons carrying the heat flux (dashed curve) and the corresponding base case (solid curve). Both have $v_d/v_{Ae} = 1.50$.

3.3.4 Scattering Rate

We now compute the wave-particle scattering rate that leads to the reduction in electron anisotropy and examine its scaling with parameters. There is no single such formalism for determining the rate because of the nonlinear nature of different scattering processes (e.g., weak scattering as described by quasilinear theory versus trapping in finite amplitude waves) [248]. For example, [249] used quasilinear theory to determine the scattering rate of the whistler anisotropy instability while others have approximated the scattering due to the proton cyclotron instability by finding the maximum exponential decay rate of the temperature anisotropy [248, 250]. Here we use the Lorenz scattering operator, which describes electrons scattering off a stationary center, to model the relaxation of the temperature anisotropy in the simulations and to deduce the scattering rate. The Lorenz operator is give by

$$\left(\frac{\partial f_e}{\partial t}\right)_e = \frac{\nu_e}{2}\frac{\partial}{\partial \xi}\left(1-\xi^2\right)\frac{\partial}{\partial \xi} f_e \tag{3.5}$$

where $\xi = \cos\theta$ and ν_e is the electron scattering rate. By taking moments of this equation to determine the rate of relaxation of the temperature anisotropy of the electron velocity distribution, we obtain a formula for ν_e,

$$\nu_e = \frac{dR/dt}{2 - R - R^2} \tag{3.6}$$

where $R = T_\parallel/T_\perp$ is the temperature anisotropy of the total electron distribution. We use this equation to model the relaxation of the temperature anisotropy near the low boundary of the simulation domain that is shown at late time in Fig. 3.4. The anisotropy profile has reached a steady state so the total time derivative in Eq. (3.6) reduces to the convective derivative

$$\nu_e = v_y \frac{\partial R/\partial y}{2 - R - R^2}, \tag{3.7}$$

where v_y is a constant equal to the heat flux drift speed at the lower boundary. The temperature anisotropy curves in Fig. 3.4 were smoothed with a Gaussian filter and the calculated scattering rates were averaged over the ranges of $0 \lesssim y \lesssim 80d_e, 0 \lesssim y \lesssim 60d_e, 0 \lesssim y \lesssim 10d_e, 0 \lesssim y \lesssim 4d_e$, for the cases of drift speed $v_d/v_{Ae} = 0.75$, 1.06, 1.50, and 2.12, respectively. In Fig. 3.10 we plot the wave-particle scattering rate for electron anisotropy reduction from the four simulations (Fig. 3.1). For the weakest drift case $v_d/v_{Ae} = 0.75$, the scattering rate is very small $\left(\sim 10^{-4}\Omega_e\right)$, while for larger drift cases the scattering rates are significantly larger, growing to $\sim 6 \times 10^{-2}\Omega_e$. The figure reveals that the scattering rate scales as a linear function of v_d/v_{Ae}, the ratio of the drift speed to electron Alfvén

speed, above a threshold given by $v_d/v_{Ae} \sim 1$.

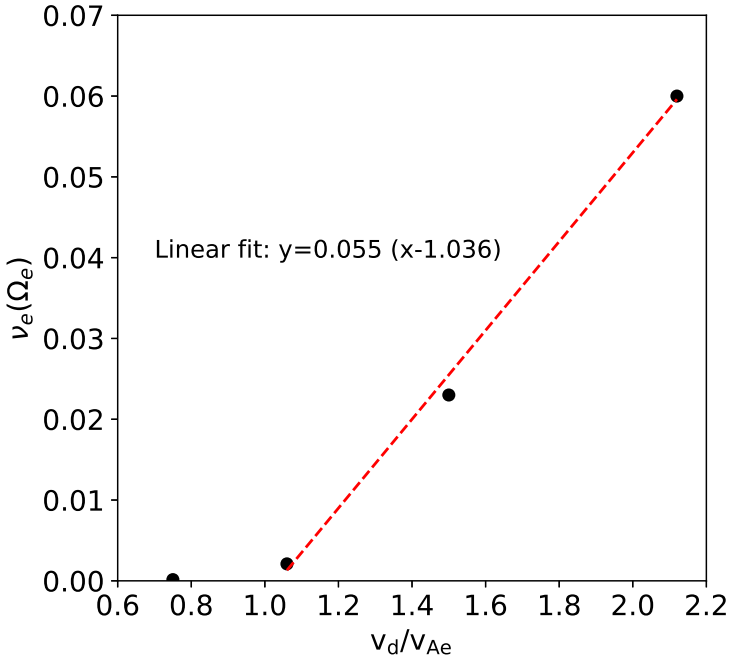


Figure 3.10: The averaged wave-electron scattering rate at late time for the four runs in Fig. 3.1 as a function of v_d/v_{Ae}, the ratio of mean parallel drift speed of heat flux to electron Alfvén speed. The scattering rate is calculated from Eq. (3.7) and is averaged over the ranges of $0 \lesssim y \lesssim 80d_e, 0 \lesssim y \lesssim 60d_e, 0 \lesssim y \lesssim 10d_e, 0 \lesssim y \lesssim 4d_e$ for the drift speeds $v_d/v_{Ae} = 0.75$, 1.06, 1.50, and 2.12, respectively. The red dashed line shows a linear fit to the data above the threshold $v_d/v_{Ae} \approx 1$.

3.4 Discussion and Conclusions

Observations and theory imply that there is suppression of the transport of energetic electrons during solar flares. We have explored pitch-angle scattering by oblique whistler waves and Weibel-driven disturbances as a mechanism for reducing the electron heat flux. The energetic electron heat flux escaping from a flare-like system excites strong oblique whistler waves through the anomalous cyclotron resonance. These waves pitch-angle scatter the electrons on a rapid timescale of hundreds of electron cyclotron periods, suppressing the heat flux and increasing the perpendicular velocities

of electrons. At high mean drift speeds compared with v_{Ae} the nonthermal electrons can also drive the Weibel instability. The resulting scattering mechanisms can operate under the generic conditions of reconnection-driven electron energization and can reduce the field-aligned electron energy flux by up to a factor of two. Of greater significance is that this scattering process increases the energetic electrons' perpendicular velocity so that the electrons will more effectively mirror and can be trapped in the large-scale magnetic fields of the flare energy release region. This scattering mechanism can therefore suppress the escape of electrons from the energy release regions of flares, which is required for them to reach the relativistic velocities documented in observations.

In previous simulations treating whistler waves in flares, the fluctuations damp out after scattering is complete and the heat flux from the initial electron distribution is reduced [172]. In contrast, in the current simulations the oblique whistler waves and Weibel perturbations are maintained in a steady-state due to the continual injection of heat flux from the boundary. This mimics the continued energy release from reconnection during flares. Such a setup represents a more physically reasonable set of initial conditions and avoids the influence of arbitrary discontinuities in the initial distribution function, giving more confidence to the interpretation of the final results. We suggest, on the basis of the present simulations, that oblique whistler waves and Weibel disturbances can grow to large amplitude during flares and scatter electrons to reduce their heat flux.

Although our model was designed to study the transport of energetic electrons in flares, the model is relevant to any $\beta \sim 1$, weakly collisional plasmas with high heat flux due to the presence of nonthermal electrons. Astrophysical applications might include accretion disc coronae [251–253]. Scattering by oblique whistlers of the solar wind strahl into the halo population is currently under active investigation [186, 198, 254]. Observations at 1AU have shown that the pitch angle widths of strahl in the presence of whistler mode waves are up to 12° larger than that in the absence of whistler

waves [255]. Large-amplitude, oblique whistlers that would limit the electron heat flux have been detected in the solar wind [256,257], in the magnetosphere [258], and in flares [259]. Simulations show that oblique whistler waves excited by the strahl component under solar wind conditions can scatter the strahl distribution into the halo and reduce the strahl-carried heat flux [187, 197]. Our simulations are focused on the flare system, where the electron heat flux is much greater than in the case of the solar wind strahl. Nevertheless, our model clarifies the mechanism for scattering of energetic electrons by whistlers that is also active in the strahl scattering problem.

Chapter 4: Whistler-Wave Scattering of Energetic Electrons Past 90 Degrees

4.1 Background

As discussed in Section 1.4, an important issue in wave–particle scattering theory is the so-called "90 Degree Problem." Strong inhibition of energetic-electron transport in the corona requires scattering over a broad range of pitch angles with respect to the ambient magnetic field. However, in conventional quasilinear theory, the pitch-angle diffusion coefficient vanishes near 90°, making it difficult for particles to scatter across this angle and become fully isotropized. As a result, the 90° pitch angle can act as an effective scattering barrier that limits further transport suppression and particle confinement. Whether this barrier can persist is therefore central to understanding the effectiveness of whistler-mediated scattering in weakly collisional plasmas.

In this chapter, we use particle-in-cell simulations to show that a pileup of energetic electrons near 90° itself provides a substantial source of free energy and can excite strong oblique whistler waves. These waves can resonate with electrons having $v_\parallel \approx 0$ and scatter them into the negative-$v_\parallel$ regime, thereby eliminating the 90° barrier. This simulation provides evidence from a new perspective that a scattering barrier at 90° cannot survive in a real system.

4.2 Simulation Setup

The context of the present simulations of electron scattering is the transport of energetic electrons in solar flares. The system is initialized with a uniform background magnetic field $B_y = B_0$ so the y direction is taken to be the parallel direction in the discussion that follows. The initial electron velocity distribution in our simulation is taken to be uniform across the domain and consists of a two-component distribution: an upward heat flux and a downward return current. The upward heat flux

consists of an isotropic kappa distribution in which electrons have already been significantly scattered in pitch angle in the positive velocity space but have been halted by a hypothetical 90-degree barrier:

$$f_\kappa\left(v_\parallel, v_\perp\right) = \frac{n_0}{\left(\pi\kappa\right)^{3/2}\theta_\parallel\theta_\perp^2}\frac{\Gamma\left(\kappa+1\right)}{\Gamma\left(\kappa-\frac{1}{2}\right)}\left[1+\frac{v_\parallel^2}{\kappa\theta_\parallel^2}+\frac{v_\perp^2}{\kappa\theta_\perp^2}\right]^{-(\kappa+1)}\Theta\left(v_\parallel\right) \tag{4.1}$$

where Γ is the gamma function, Θ is the Heaviside step function, n_0 is the electron density, κ is a parameter that controls the steepness of the nonthermal tail of the distribution, $\theta_n^2 = v_{th,n}^2\left(\kappa-3/2\right)/\kappa$ is the effective thermal speed, $v_{th,n}^2 = 2T_n/m_e$ is the regular thermal speed, T_n is the temperature in the n-direction and m_e is the electron mass.

The current associated with the heat flux is balanced by a colder plasma flowing from the hot to the cold reservoir. The development of such a return current has been documented in earlier simulations of energetic electron injection into a colder background plasma relevant to flare energy release [157]. The return current in the initial distribution is modeled as a Maxwellian distribution drifting in the negative $v_\parallel$ direction:

$$f_M\left(v_\parallel, v_\perp\right) = \frac{n_0}{\pi^{3/2}v_T^3\left[1+F_{erf}(v_d/v_c)\right]}\exp\left\{-\left[\left(v_\parallel+v_d\right)^2+v_\perp^2\right]/v_c^2\right\}\Theta\left(-v_\parallel\right) \tag{4.2}$$

where $v_c^2 = 2T_c/m_e$ is the thermal speed of the return current, v_d is a drift speed that ensures the total initial distribution has zero current, and the error function F_{erf} ensures the densities of the heat flux and the return current are equal. The parameters used in the distribution functions are: κ = 4, $T_\parallel = T_\perp = 20T_c$, $\beta_\parallel = 2$ where β is the ratio of plasma thermal pressure to magnetic pressure, $c/v_{Ae} = 10$ and $v_d/v_{Ae} = 3/\sqrt{2}$.

Figure 4.1 shows the initial electron velocity distribution function, characterized by an energetic

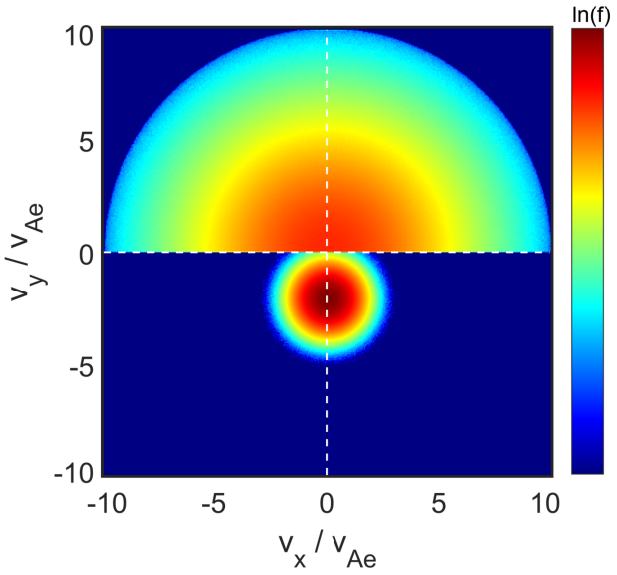


Figure 4.1: Log plot of the initial electron velocity distribution functions in the $v_y - v_x$ plane. The distribution function is integrated over v_z and is derived from the entire simulation domain. Unless otherwise stated, the y direction is equivalent to the parallel direction.

semi-circular kappa distribution in the positive $v_\parallel$ domain and a cold beam distribution in the negative $v_\parallel$ domain. The heat flux is scattered into a uniform distribution with pitch angles $0 < \theta < 90°$, but the scattering is stopped by the $90°$ barrier. Again, the form of the cold return current beam is supported by a prior study [157] where the cold return current was self-generated by the injection of hot plasma into a cold background. This setup, which is similar to previous studies featuring a strong heat flux and a return beam [167, 172], can represent energetic particle outflow from magnetic reconnection-driven solar flares. Simulations [16] have shown that reconnection can drive the energetic outflow to a marginal firehose state where $\beta_\parallel - \beta_\perp > 2$. The parameter v_d/v_{Ae}, a key factor in our system for wave instability and scattering efficiency, falls within a reasonable range of observational data. Our value for β is too low to properly descibe electron transport in the intracluster medium (ICM) [169, 171, 179, 190, 244]. However, a drift speed above the electron Alfvén speed is the regime of interest for the ICM.

The dimensions of the simulation domain are $L_y = 2L_x = 81.92\ d_e$ and the time step is $0.008\Omega_e^{-1}$. Ions are initialized with a cold Maxwellian distribution with temperature T_c, and do not play an important role due to the large assumed mass ratio, m_i/m_e = 1600. The simulation uses 560 particles per species per cell and has a grid of 1024 by 2048 cells. We adopt periodic boundary conditions in both directions.

4.3 Simulation Results

4.3.1 Wave Excitation

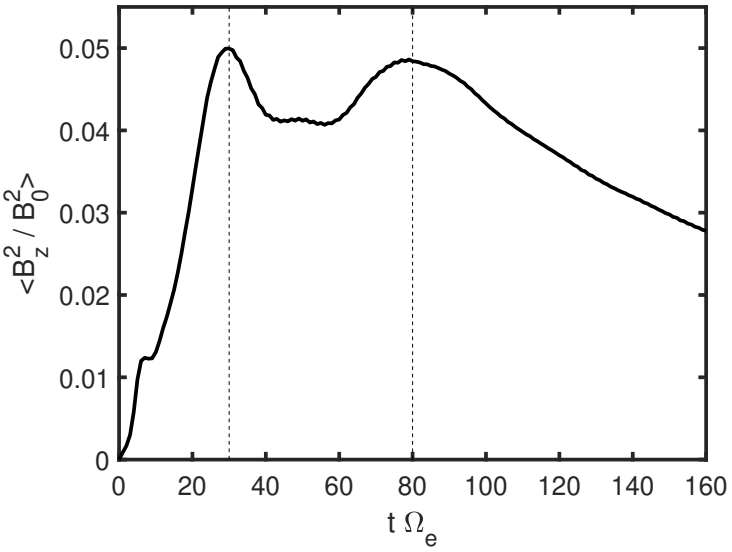


Figure 4.2: Box-averaged out-of-plane magnetic fluctuation amplitude B_z^2/B_0^2 as a function of time. Two dashed lines mark the peaks at $t\Omega_e \sim 30$ and $t\Omega_e \sim 80$, which are the times corresponding the plots in Figure 4.3(a) and (b).

The initial distribution (see Figure 4.1) drives the system unstable and amplifies magnetic fluctuations. Figure 4.2 shows the time evolution of the box-averaged out-of-plane magnetic field variance $\langle B_z^2/B_0^2\rangle$, which serves as an overall indicator of wave activity in the system. The fluctuations grow exponentially at the beginning and reach a short-lived plateau at $t\Omega_e \sim 10$. 2D images of B_z at this moment (not

shown here) reveal an oblique mode with a very short wavelength ($\sim 0.1d_e$). Because this mode is smaller in amplitude and transient in time, its impact on particle scattering can be neglected. The magnetic fluctuations reach their first peak at $t\Omega_e \sim 30$, decrease slightly to form another plateau, and then grow again to reach a second peak at $t\Omega_e \sim 80$. Corresponding 2D images at these times are shown in Figure 4.3(a) and (b). After the second peak, the fluctuations decay slowly. A similar two-peak pattern in magnetic fluctuation has been observed in previous studies [170, 172].

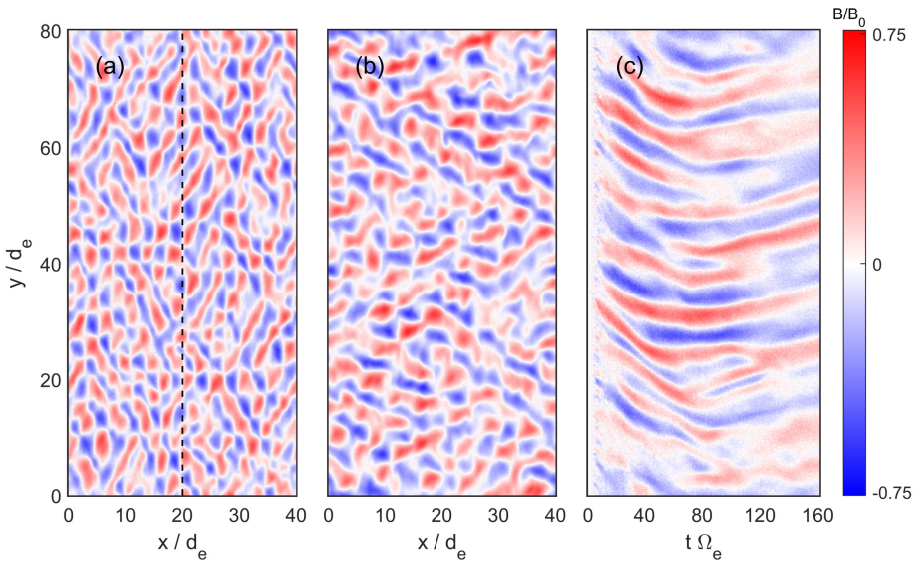


Figure 4.3: Two-dimensional plots of the out-of-plane magnetic field B_z/B_0 at (a) $t\Omega_e = 30$ and (b) $t\Omega_e = 80$. Panel (c) represents a space–time diagram taken from a cut along the y direction at $x = 20d_e$ (indicated by the vertical black dashed line in panel (a)).

Figures 4.3(a) and (b) are 2D images of the out-of-plane magnetic fluctuations, B_z/B_0, at $t\Omega_e = 30$ and 80, respectively. Figure 4.3(a) corresponds to the first peak in the amplitudes of the magnetic fluctuations. The fluctuations correspond to oblique waves with a pitch angle of approximately $60°$. The B_z component has a peak value around $0.75B_0$, while the magnitude of the B_x component (not shown here) is smaller. Averaging $\delta B^2 = B_z^2 + B_x^2$ over the entire domain, we find the mean fluctuation amplitude is $\delta B/B_0 \sim 0.1$. Figure 4.3(b) is taken during the second peak of wave activity and shows a

similar oblique mode except that the angle of propagation with respect to the ambient field is reduced to approximately $40°$. Fast Fourier Transforms (FFT) of the fluctuations shown in panels (a) and (b) (not shown) indicate the wave patterns correspond to a dominant oblique mode with a finite bandwidth. The amplitudes of the parallel modes are small.

Figure 4.3(c) is a space–time diagram taken from the vertical dashed line in Figure 4.3(a). Two major phases of wave activity are apparent: a downward-traveling wave in the time interval $20 \lesssim t\Omega_e \lesssim 60$ with a phase speed of approximately $0.3v_{Ae}$, and an upward-moving wave in the interval $70 \lesssim t\Omega_e \lesssim 160$ with a smaller phase speed of around $0.1v_{Ae}$. Whistlers traveling in different directions suggest that they are driven by different electron components. The initial downward whistler is resonant with and driven primarily by the downward-traveling beam (Equation 4.2), while the later upward whistler is driven by the energetic electrons moving in the upward (positive $v_{\|}$) direction (Equation 4.1). Further evidence for this interpretation comes from the time dependence of the electron distribution functions.

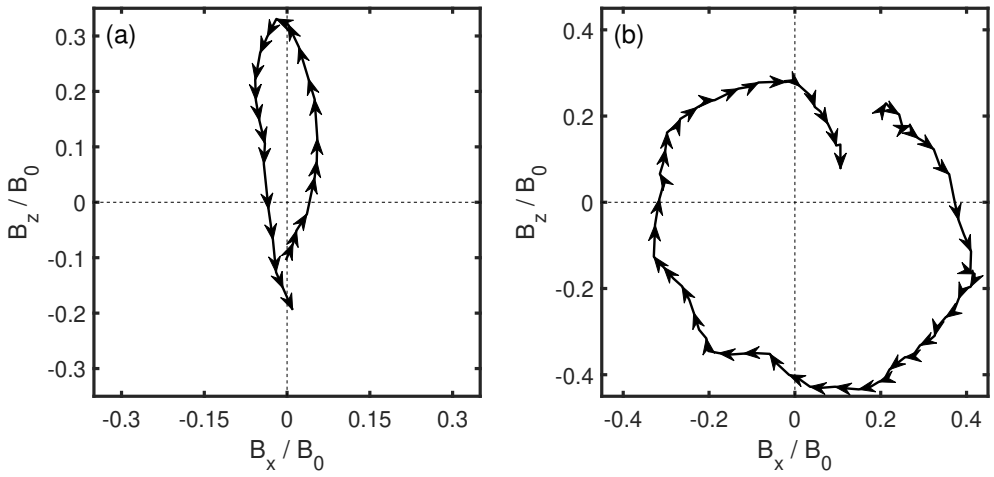


Figure 4.4: Hodogram of the magnetic field components (B_z vs. B_x) at a fixed location $x = y = 20d_e$ during the time intervals: (a) $37 \leq t\Omega_e \leq 60$ and (b)$70 \leq t\Omega_e \leq 160$. The arrows indicate the direction of rotation.

Figure 4.4 shows hodograms of the magnetic field components, B_z versus B_x, from a fixed location in the simulation domain. Figure 4.4(a) is from the time interval $37 \leq t\Omega_e \leq 60$, which approximately coincides with the period of the downward-traveling whistlers. Figure 4.4(b) is in the interval $70 \leq t\Omega_e \leq 160$, which is the upward-moving phase. Figure 4.4(a) exhibits a left-handed elliptical polarization, while Figure 4.4(b) shows a right-handed polarization. Considering the wave direction, Figure 4.4(a) is from the viewpoint of the receiver (the wave goes to the viewer), and Figure 4.4(b) is from the viewpoint of the source (the wave goes away from the viewer). Both perspectives confirm that these magnetic fluctuations exhibit right-handed polarization, and hence are consistent with being whistlers. Another perspective on the rotation of the whistler at early time is that the return current electrons are dominating the wave dynamics. In the frame of the return current, whose negative velocity ($2.12v_{Ae}$) exceeds that of the whistler ($0.1v_{Ae}$), the whistler has a right-hand rotation direction.

4.3.2 Electron Scattering Past 90 Degrees

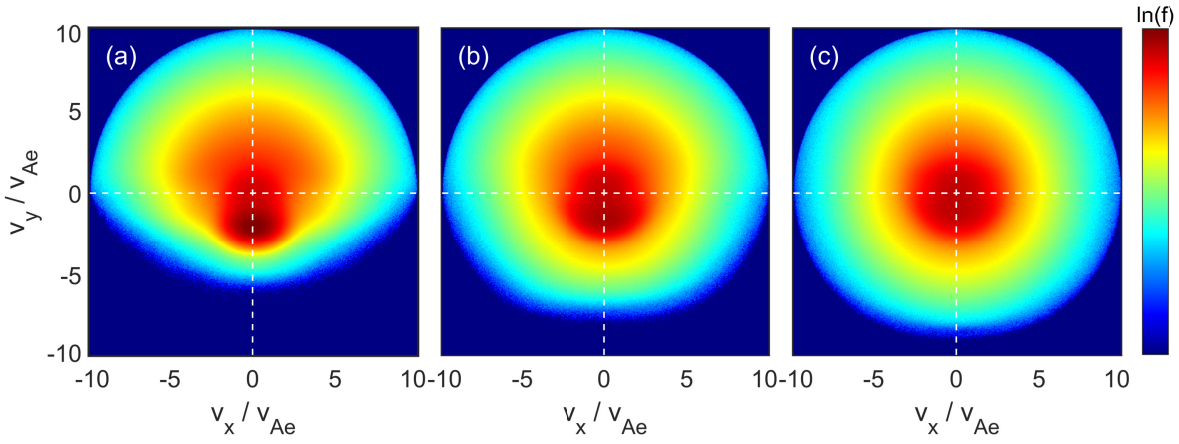


Figure 4.5: Log plot of the electron velocity distribution functions in the $v_y - v_x$ plane at (a) $t\Omega_e = 30$, (b) $t\Omega_e = 80$ and (c) $t\Omega_e = 160$. The distribution function is summed over v_z and is derived from the entire simulation domain.

Shown in Figure 4.5 are the electron velocity-space distributions at several times during the

simulation. In Figure 4.5(a) the initial gap around $v_\parallel = 0$ is filled in. A significant portion of the return current, which initially had $v_\parallel < 0$, has moved towards $v_\parallel = 0$ and into the region with $v_\parallel > 0$. Thus, the negative velocity whistler is scattering and extracting energy from the return current particles as in the normal heat flux whistler instability [172]. At the same time some $v_\parallel > 0$ electrons have moved across the $v_\parallel = 0$ boundary into the region $v_\parallel < 0$. Such particles are also potentially contributing to the growth of the downward propagating whistler, although whether they contribute net energy to the downward waves is unclear. In Figure 4.5(b), at the second peak of wave activity ($t\Omega_e = 80$), the distribution function in the negative $v_\parallel$ plane is significantly broadened, indicating a substantial number of the energetic electrons in the positive $v_\parallel$ plane scattered past the 90° barrier. This demonstrates that the pitch angle diffusion coefficient at 90° is nonzero. The diffusion of $v_\parallel > 0$ electrons towards $v_\parallel = 0$ contributes energy to the positive propagating whistler that has reached its peak amplitude at this time. Despite the strong whistler-driven scattering, there are no obvious horn-like structures in velocity space as was seen in previous simulations [172]. This is likely due to the overlap of resonance bands [181, 189]. It is noteworthy that, although the evolution of the distribution function seems to indicate a one-direction net flow from the upper plane to the lower plane, previous studies suggest, based on single particle trajectories, that many particles may have crossed the $v_\parallel = 0$ threshold multiple times [167, 170, 188].

At the end of the simulation, shown in Figure 4.5(c), the final distribution appears nearly isotropic, indicating complete scattering. A significant number of electrons passing the 90° barrier implies a substantial reduction in the parallel heat flux. This process occurred on a rapid timescale of hundreds of electron cyclotron periods, demonstrating that whistler scattering is an efficient mechanism for inhibiting heat flux and confining escaping high-energy electrons in solar flares.

Figure 4.6 shows the electron distribution function integrated over a constant-velocity phase

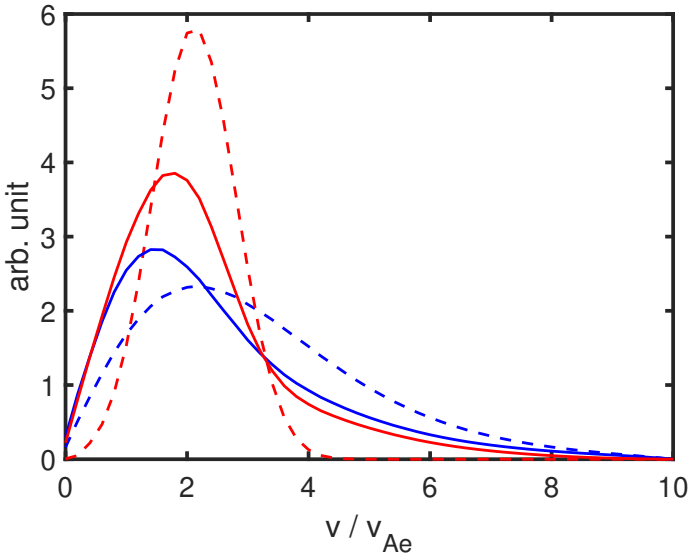


Figure 4.6: Distribution function summed over equal-velocity strips from the data in Figure 4.5 (*i.e.*, the quantity $\sum_i f(v_i)$ where $v_i = (v_{ix}^2 + v_{iy}^2)^{1/2}$ and $v_0 \leq v_i \leq v_0 + \Delta v$). The blue curve corresponds to the sum in the upper plane ($v_{iy} > 0$), and the red curve to the lower plane ($v_{iy} < 0$). The bin width is $\Delta v = 0.2 v_{Ae}$. The dashed lines correspond to the initial distribution (Figure 4.1), and the solid lines to the final distribution (Figure 4.5(c)).

space from the $v_\parallel > 0$ region (blue lines) and $v_\parallel < 0$ region (red lines). The dashed lines correspond to the initial distribution (Figure 4.1), and the solid lines to the final distribution (Figure 4.5(c)). The initial beam (red dashed line) decays and drifts to a lower velocity. The tail of the red dashed line starts at zero, as there are no energetic particles in the $v_\parallel < 0$ region initially. Due to scattering, the initial particles from the $v_\parallel > 0$ region (blue dashed line) decrease. As a result, shown by the solid blue and red lines, the high-energy tails of the final distributions are nearly equal, implying that around half of the particles from the $v_\parallel > 0$ region have been scattered to the $v_\parallel < 0$ region.

4.4 Discussion and Conclusions

Using particle-in-cell simulations, we explored electron pitch-angle scattering past 90° by oblique whistler waves in a system with an initial heat flux of energetic electrons with pitch angles less than 90°.

This distribution might result from a hypothetical barrier to electron scattering at $90°$. We demonstrated that this heat flux drives strong oblique whistler waves (with magnitude $\delta B/B_0 \sim 0.1$ and a wave vector normal angle of approximately $60°$). These waves scatter a large fraction (around 50%) past 90° into the negative parallel velocity domain, making the late-time distribution nearly isotropic. This result confirms that large-amplitude, oblique whistlers can grow during flares and efficiently inhibit heat flux transport in the corona [167, 172].

The results of earlier simulations suggested that the strong heat flux that is expected from a reconnection-driven solar flare [16] would drive oblique whistlers of sufficiently large amplitude to drive electrons past pitch angles of $90°$ [167, 172]. In other plasma environments with weaker heat fluxes and lower amplitude whistler waves the turbulence might be unable to diffuse electrons past 90°. The result might be an effective $90°$ scattering barrier. However, our simulations suggest that electron pile-up near 90° yields a system with additional free energy that drives large-amplitude, oblique waves that efficiently scatter electrons past 90°. Thus, we conclude that a scattering barrier at $90°$ can not survive in a real system. We have shown that both oblique propagation and large amplitude of whistler waves are crucial for enabling the scattering of electrons past 90°. Oblique propagation allows for a Landau resonance for electrons with $|v_\parallel/v_{the}| \ll 1$, which requires strong wave power at $kd_e \ll 1$. This condition cannot be achieved by parallel whistlers since their interaction with $|v_\parallel/v_{the}| \ll 1$ electrons is associated with waves with $kd_e \gg 1$, where the wave power is weak.

Our initial distribution was designed to model the energetic electron outflow from flares in the solar corona where the mean energetic electron flux is expected to exceed the electron Alfvén speed [16]. The electron Alfvén speed is the drift threshold for the onset of strong whistler-driven electron pitch angle scattering [167]. In the ICM, where the plasma β is around 100, typical thermal speeds are well above the electron Alfvén speed. The heat flux in the ICM is expected to develop as a result of

the magnetic-field-aligned electron temperature gradient. Suppose that there is a 90° scattering barrier in such a system. The hot plasma would penetrate into the cold region while maintaining a thermal distribution with pitch angles in the range $0 < \theta < 90^\circ$. At the same location in the absence of scattering across 90°, there would be a separate colder plasma with pitch angles $90^\circ < \theta < 180^\circ$. The consequence would be a distribution similar to that shown in Figure 4.1. The differing temperatures of the positive and negative velocity electrons would again produce discontinuities across the $v_\parallel = 0$ boundary. With increasing penetration of the hot plasma into the cold region, the resulting distribution will drive oblique whistlers that will relax the gradient across the 90° boundary.

Chapter 5: Summary and Outlook

5.1 Summary of the Main Results

This thesis has presented three related studies, whose main results are summarized below. In Chapter 2, we performed two-dimensional particle-in-cell simulations with a realistic ion–electron mass ratio to investigate the development of electron anisotropy and scattering during particle energy gain. As a side benefit, these simulations also led to new insights into the generation of out-of-plane magnetic fields within flux ropes. In the absence of a guide field, strong electron temperature anisotropy develops in the reconnection exhaust and drives the Weibel instability, which generates bipolar out-of-plane magnetic fields inside magnetic islands. These magnetic fields scatter the in-plane electron heat flux and redistribute electron energy from the parallel to the perpendicular direction. Because the energy gain associated with Fermi acceleration is proportional to a particle's parallel velocity, such scattering is expected to reduce the efficiency of electron acceleration. In the presence of a strong guide field, electron outflows from the X-line are deflected along the separatrices and form circular current loops wrapping the flux ropes. These separatrix currents generate out-of-plane magnetic fields B_z that reinforce the flux rope core field. The extended electron sheared flow can further become unstable to the electron Kelvin–Helmholtz instability, producing localized electron current vortices and enhanced regions of magnetic field B_z. Island merging helps sustain and, in some cases, further amplify the core magnetic field.

In Chapter 3, we investigated pitch-angle scattering by oblique whistler waves and Weibel-driven fluctuations as a mechanism for suppressing electron heat flux in flare loops. Energetic electrons escaping from a flare-like system excite strong oblique whistler waves, which rapidly scatter electrons on timescales of several hundred electron cyclotron periods, reduce the field-aligned heat flux, and

increase the perpendicular electron velocity. At sufficiently large drift speeds, the nonthermal electrons can also drive the Weibel instability. These scattering processes arise naturally under reconnection-driven electron energization and can significantly reduce the field-aligned electron energy flux. The increase in perpendicular velocity will also enhance magnetic mirroring, allowing energetic electrons to be more effectively trapped within the large-scale magnetic fields of the flare energy-release region.

In Chapter 4, we examined the long-standing question of whether a persistent 90° pitch-angle barrier can survive in the presence of whistler scattering. We showed that when electrons accumulate near 90°, the resulting distribution contains sufficient free energy to drive large-amplitude oblique whistler waves. These waves subsequently scatter electrons across 90°, producing a much broader and more nearly isotropic pitch-angle distribution. This result suggests that a persistent 90° barrier cannot be maintained in a self-consistent kinetic system and supports the idea that whistler waves can drive pitch angle scattering across the full range of pitch angles and therefore limit electron transport.

Although the three studies presented in this thesis address different physical problems, they are united by a common physical picture: reconnection-driven electron distributions can generate kinetic-scale instabilities that subsequently feed back on the system. Magnetic reconnection naturally produces non-Maxwellian electron distributions through processes such as Fermi acceleration, leading to temperature anisotropy, heat flux, and velocity shear. These sources of free energy drive the magnetic structures and waves examined throughout this thesis and significantly influence flux-rope structure, energetic-electron acceleration, and heat-flux transport in astrophysical plasmas. Together, these results demonstrate that electron-scale kinetic physics is an intrinsic component of magnetic reconnection.

5.2 Limitations of the Present Work

The present work is subject to several limitations. First, as in almost all particle-in-cell simulations, the spatial and temporal scales accessible to the simulations are far smaller than the characteristic scales of real astrophysical systems. As a result, the simulations presented here should be interpreted primarily as studies of local microphysical processes rather than direct models of entire astrophysical environments. Besides, the present work does not fully address the coupling between kinetic-scale scattering and global-scale transport. Although a growing body of research suggests that plasma instabilities can influence transport on astrophysically relevant scales, it remains difficult to determine quantitatively how the local kinetic processes explored here modify the global evolution of energetic particles and heat flux in macroscale systems.

Second, some aspects of the numerical setup are necessarily idealized. In the simulations presented in Chapters 3 and 4, the initial electron velocity distributions contain artificial discontinuities parallel to the ambient magnetic field near $v_y = 0$. Although these features are transient and their influence diminishes rapidly, they nevertheless reflect the simplified initial conditions adopted in the model. More generally, the use of idealized distribution functions and boundary conditions may limit the direct applicability of the results to more complex natural systems. The magnetic geometry employed in the simulations is also highly simplified compared with realistic coronal and magnetospheric configurations.

Another important limitation is that the present simulations are entirely two-dimensional. Although 2D PIC simulations capture many of the essential kinetic processes associated with magnetic reconnection and wave–particle interactions, real astrophysical plasmas are inherently three-dimensional. For example, in 3D the fastest-growing oblique modes may occupy a cone in wave-vector space rather than a single

propagation direction, allowing energetic electrons to interact simultaneously with waves spanning a range of azimuthal angles. Such interactions could increase resonance overlap, nonlinear trapping, and stochastic particle motion, potentially modifying the pitch-angle diffusion process and enhancing scattering efficiency. Future fully three-dimensional simulations will be important for assessing the significance of these effects.

5.3 Future Directions

Several important questions remain open and provide natural directions for future work. In the study of flux-rope core fields, an important next step is to determine whether the self-generation of out-of-plane magnetic fields persists in larger islands and how the underlying mechanisms evolve as islands grow to larger scales. Future kinetic simulations with larger system sizes and longer durations will be valuable for addressing these questions and establishing the scaling of the proposed mechanisms. A more quantitative model of the influence of these fields on electron scattering should be developed and tested in future work. It will also be important to verify observational reports of core magnetic fields oriented opposite to the surrounding guide field, as such observations would provide strong evidence against models based solely on guide-field compression. Extending the simulations to fully three-dimensional configurations may reveal important aspects of flux-rope evolution that cannot be captured in two-dimensional systems. As reconnection-generated flux ropes continue to grow, they may eventually become unstable to three-dimensional kink instability [260–263]. The resulting distortion of the flux ropes can generate stochastic magnetic field-line transport, allowing energetic particles to escape from otherwise well-confined flux ropes and access additional acceleration regions [260]. These three-dimensional effects are expected to substantially modify both the long-

term evolution of flux ropes and the efficiency of particle acceleration during magnetic reconnection. Finally, closer comparisons with observations and continued collaboration between simulation and observational studies will be essential for testing and constraining these ideas.

In the study of whistler-wave scattering and the 90° barrier problem, several issues also remain unresolved. The simulation domain used in Chapter 3 could be further enlarged to allow longer wave–particle interaction times. A larger domain would enable the system to evolve closer to a fully isotropic state, potentially resulting in a greater reduction of the electron heat flux. Future work should investigate how the wave spectrum evolves in fully three-dimensional systems and how such evolution influences particle transport and scattering. Developing a more complete mathematical description of turbulent transport and scattering would also be valuable. Ultimately, connecting the local kinetic processes identified in the present simulations with the large-scale evolution of solar flares remains an important challenge.

Bibliography

[1] Eugene N Parker. Sweet's mechanism for merging magnetic fields in conducting fluids. *Journal of Geophysical Research*, 62(4):509–520, 1957.

[2] PA Sweet. 14. the neutral point theory of solar flares. In *Symposium-International Astronomical Union*, volume 6, pages 123–134. Cambridge University Press, 1958.

[3] Harry E Petschek. Magnetic field annihilation. In *The Physics of Solar Flares, Proceedings of the AAS-NASA Symposium held 28-30 October, 1963 at the Goddard Space Flight Center, Greenbelt, MD. Edited by Wilmot N. Hess. Washington, DC: National Aeronautics and Space Administration, Science and Technical Information Division, 1964., p. 425*, volume 50, page 425, 1964.

[4] TG Forbes. Magnetic reconnection in solar flares. *Geophysical & Astrophysical Fluid Dynamics*, 62(1-4):15–36, 1991.

[5] Kazunari Shibata. Evidence of magnetic reconnection in solar flares and a unified model of flares. *Astrophysics and Space Science*, 264(1):129–144, 1998.

[6] James W Dungey. Interplanetary magnetic field and the auroral zones. *Physical Review Letters*, 6(2):47, 1961.

[7] Edward W Hones Jr. Magnetic reconnection in the earth's magnetotail. *Australian journal of physics*, 38(6):981–998, 1985.

[8] Tsugunobu Nagai and Shinobu Machida. Magnetic reconnection in the near-earth magnetotail. *Geophysical Monograph-American Geophysical Union*, 105:211–224, 1998.

[9] T Nagai, I Shinohara, M Fujimoto, M Hoshino, Y Saito, S Machida, and T Mukai. Geotail observations of the hall current system: Evidence of magnetic reconnection in the magnetotail. *Journal of Geophysical Research: Space Physics*, 106(A11):25929–25949, 2001.

[10] Amitava Bhattacharjee. Impulsive magnetic reconnection in the earth's magnetotail and the solar corona. *Annu. Rev. Astron. Astrophys.*, 42(1):365–384, 2004.

[11] MI Pudovkin and VS Semenov. Magnetic field reconnection theory and the solar wind—magnetosphere interaction: A review. *Space Science Reviews*, 41(1):1–89, 1985.

[12] JT Gosling, Ruth M Skoug, DJ McComas, and CW Smith. Direct evidence for magnetic reconnection in the solar wind near 1 au. *Journal of Geophysical Research: Space Physics*, 110(A1), 2005.

[13] TD Phan, JT Gosling, MS Davis, Ruth M Skoug, M Øieroset, RP Lin, RP Lepping, DJ McComas, CW Smith, H Reme, et al. A magnetic reconnection x-line extending more than 390 earth radii in the solar wind. *Nature*, 439(7073):175–178, 2006.

[14] GP l Zank, JA Le Roux, GM Webb, A Dosch, and O Khabarova. Particle acceleration via reconnection processes in the supersonic solar wind. *The Astrophysical Journal*, 797(1):28, 2014.

[15] JT Dahlin, JF Drake, and M Swisdak. The mechanisms of electron heating and acceleration during magnetic reconnection. *Physics of Plasmas*, 21(9):092304, 2014.

[16] Harry Arnold, James F Drake, Marc Swisdak, Fan Guo, Joel T Dahlin, Bin Chen, Gregory Fleishman, Lindsay Glesener, Eduard Kontar, Tai Phan, et al. Electron acceleration during macroscale magnetic reconnection. *Physical review letters*, 126(13):135101, 2021.

[17] Mitsuo Oka, Joachim Birn, Jan Egedal, Fan Guo, Robert E Ergun, Drew L Turner, Yuri Khotyaintsev, Kyoung-Joo Hwang, Ian J Cohen, and James F Drake. Particle acceleration by magnetic reconnection in geospace. *Space Science Reviews*, 219(8):75, 2023.

[18] Eo G Harris. On a plasma sheath separating regions of oppositely directed magnetic field. *Il Nuovo Cimento (1955-1965)*, 23(1):115–121, 1962.

[19] J Birn, JF Drake, MA Shay, BN Rogers, RE Denton, M Hesse, M Kuznetsova, ZW Ma, A Bhattacharjee, A Otto, et al. Geospace environmental modeling (gem) magnetic reconnection challenge. *Journal of Geophysical Research: Space Physics*, 106(A3):3715–3719, 2001.

[20] Yi-Hsin Liu, M Hesse, F Guo, W Daughton, H Li, PA Cassak, and MA Shay. Why does steady-state magnetic reconnection have a maximum local rate of order 0.1? *Physical Review Letters*, 118(8):085101, 2017.

[21] PA Sweet. Mechanisms of solar flares. *Annual Review of Astronomy and Astrophysics, vol. 7, p. 149*, 7:149, 1969.

[22] BV Somov and AI Verneta. Tearing instability of reconnecting current sheets in space plasmas. *Space science reviews*, 65(3):253–288, 1993.

[23] Q Chen, A Otto, and LC Lee. Tearing instability, kelvin-helmholtz instability, and magnetic reconnection. *Journal of Geophysical Research: Space Physics*, 102(A1):151–161, 1997.

[24] Luca Del Zanna, Emanuele Papini, Simone Landi, Matteo Bugli, and Niccolo' Bucciantini. Fast reconnection in relativistic plasmas: the magnetohydrodynamics tearing instability revisited. *Monthly Notices of the Royal Astronomical Society*, 460(4):3753–3765, 2016.

[25] Dmitri A Uzdensky and Nuno F Loureiro. Magnetic reconnection onset via disruption of a forming current sheet by the tearing instability. *Physical Review Letters*, 116(10):105003, 2016.

[26] TH Stix. Waves in plasmas (new york: American institute of physics). *and*, 26:6, 1992.

[27] Robert J Goldston. *Introduction to plasma physics*. CRC Press, 2020.

[28] José A Bittencourt. *Fundamentals of plasma physics*. Springer Science & Business Media, 2013.

[29] William A Newcomb. Motion of magnetic lines of force. *Annals of Physics*, 3(4):347–385, 1958.

[30] ME Mandt, RE Denton, and JF Drake. Transition to whistler mediated magnetic reconnection. *Geophysical Research Letters*, 21(1):73–76, 1994.

[31] Michael A Shay and James F Drake. The role of electron dissipation on the rate of collisionless magnetic reconnection. *Geophysical Research Letters*, 25(20):3759–3762, 1998.

[32] MA Shay, JF Drake, BN Rogers, and RE Denton. Alfvénic collisionless magnetic reconnection and the hall term. *Journal of Geophysical Research: Space Physics*, 106(A3):3759–3772, 2001.

[33] JF Drake, MA Shay, and M Swisdak. The hall fields and fast magnetic reconnection. *Physics of Plasmas*, 15(4), 2008.

[34] Ellen G Zweibel and Masaaki Yamada. Magnetic reconnection in astrophysical and laboratory plasmas. *Annual review of astronomy and astrophysics*, 47(1):291–332, 2009.

[35] Masaaki Yamada, Russell Kulsrud, and Hantao Ji. Magnetic reconnection. *Reviews of modern physics*, 82(1):603, 2010.

[36] DI Pontin. Three-dimensional magnetic reconnection regimes: A review. *Advances in Space Research*, 47(9):1508–1522, 2011.

[37] Fan Guo, Yi-Hsin Liu, Xiaocan Li, Hui Li, William Daughton, and Patrick Kilian. Recent progress on particle acceleration and reconnection physics during magnetic reconnection in the magnetically-dominated relativistic regime. *Physics of Plasmas*, 27(8), 2020.

[38] Valentina V Zharkova, Karpar Arzner, Arnold O Benz, Philippa Browning, Cyril Dauphin, A Gordon Emslie, Lyndsay Fletcher, Eduard P Kontar, Gottfried Mann, Marco Onofri, et al. Recent advances in understanding particle acceleration processes in solar flares. *Space science reviews*, 159(1):357, 2011.

[39] Fan Guo, Yi-Hsin Liu, Seiji Zenitani, and Masahiro Hoshino. Magnetic reconnection and associated particle acceleration in high-energy astrophysics. *Space Science Reviews*, 220(4):43, 2024.

[40] JF Drake, M Swisdak, H Che, and MA Shay. Electron acceleration from contracting magnetic islands during reconnection. *Nature*, 443(7111):553–556, 2006.

[41] JT Dahlin, JF Drake, and M Swisdak. Parallel electric fields are inefficient drivers of energetic electrons in magnetic reconnection. *Physics of Plasmas*, 23(12):120704, 2016.

[42] Xiaocan Li, Fan Guo, and Yi-Hsin Liu. The acceleration of charged particles and formation of power-law energy spectra in nonrelativistic magnetic reconnection. *Physics of Plasmas*, 28(5), 2021.

[43] JF Drake, Merav Opher, Marc Swisdak, and JN Chamoun. A magnetic reconnection mechanism for the generation of anomalous cosmic rays. *The Astrophysical Journal*, 709(2):963–974, 2010.

[44] David Burgess, PW Gingell, and Lorenzo Matteini. Multiple current sheet systems in the outer heliosphere: energy release and turbulence. *The Astrophysical Journal*, 822(1):38, 2016.

[45] Kevin M Schoeffler, JF Drake, and M Swisdak. The effects of plasma beta and anisotropy instabilities on the dynamics of reconnecting magnetic fields in the heliosheath. *The Astrophysical Journal*, 743(1):70, 2011.

[46] Colby C Haggerty, Michael A Shay, Alexandros Chasapis, Tai D Phan, James F Drake, Kittipat Malakit, Paul A Cassak, and Rungployphan Kieokaew. The reduction of magnetic reconnection outflow jets to sub-alfvénic speeds. *Physics of Plasmas*, 25(10), 2018.

[47] JF Drake, M Swisdak, and R Fermo. The power-law spectra of energetic particles during multi-island magnetic reconnection. *The Astrophysical Journal Letters*, 763(1):L5, 2013.

[48] Xiaocan Li, Fan Guo, Hui Li, Adam Stanier, and Patrick Kilian. Formation of power-law electron energy spectra in three-dimensional low-β magnetic reconnection. *The Astrophysical Journal*, 884(2):118, 2019.

[49] Masahiro Hoshino. Efficiency of nonthermal particle acceleration in magnetic reconnection. *Physics of Plasmas*, 29(4), 2022.

[50] Zhiyu Yin, James F Drake, and Marc Swisdak. Simultaneous proton and electron energization during macroscale magnetic reconnection. *The Astrophysical Journal*, 974(1):74, 2024.

[51] Säm Krucker, HS Hudson, L Glesener, SM White, S Masuda, J-P Wuelser, and RP Lin. Measurements of the coronal acceleration region of a solar flare. *The Astrophysical Journal*, 714(2):1108, 2010.

[52] M Oka, S Ishikawa, P Saint-Hilaire, S Krucker, and RP Lin. Kappa distribution model for hard x-ray coronal sources of solar flares. *The Astrophysical Journal*, 764(1):6, 2013.

[53] A Warmuth and G Mann. Constraints on energy release in solar flares from rhessi and goes x-ray observations-i. physical parameters and scalings. *Astronomy & Astrophysics*, 588:A115, 2016.

[54] Markus J Aschwanden, Amir Caspi, Christina MS Cohen, Gordon Holman, Ju Jing, Matthieu Kretzschmar, Eduard P Kontar, James M McTiernan, Richard A Mewaldt, Aidan O'Flannagain, et al. Global energetics of solar flares. v. energy closure in flares and coronal mass ejections. *The Astrophysical Journal*, 836(1):17, 2017.

[55] Lindsay Glesener, Säm Krucker, Jessie Duncan, Iain G Hannah, Brian W Grefenstette, Bin Chen, David M Smith, Stephen M White, and Hugh Hudson. Accelerated electrons observed down to¡ 7 kev in a nustar solar microflare. *The Astrophysical Journal Letters*, 891(2):L34, 2020.

[56] Takashi Sakurai, Kazunari Shibata, Kiyoshi Ichimoto, Saku Tsuneta, and Loren W Acton. Flare-related relaxation of magnetic shear as observed with the soft x-ray telescope of yohkoh and with vector magnetographs. *Publications of the Astronomical Society of Japan*, 44(5):123–127, 1992.

[57] S Masuda, T Kosugi, H Hara, S Tsuneta, and Y Ogawara. A loop-top hard x-ray source in a compact solar flare as evidence for magnetic reconnection. *Nature*, 371(6497):495–497, 1994.

[58] HS Hudson, T Kosugi, NV Nitta, and M Shimojo. Hard x-radiation from a fast coronal ejection. *The Astrophysical Journal Letters*, 561(2):L211–L214, 2001.

[59] Gregory D Fleishman, Dale E Gary, Bin Chen, Natsuha Kuroda, Sijie Yu, and Gelu M Nita. Decay of the coronal magnetic field can release sufficient energy to power a solar flare. *Science*, 367(6475):278–280, 2020.

[60] NJ Fox, MC Velli, SD Bale, R Decker, A Driesman, RA Howard, Justin C Kasper, J Kinnison, M Kusterer, D Lario, et al. The solar probe plus mission: humanity's first visit to our star. *Space Science Reviews*, 204(1):7–48, 2016.

[61] L-J Chen, A Bhattacharjee, PA Puhl-Quinn, H Yang, N Bessho, S Imada, S Mühlbachler, PW Daly, B Lefebvre, Yuri Khotyaintsev, et al. Observation of energetic electrons within magnetic islands. *Nature Physics*, 4(1):19–23, 2008.

[62] Haisheng Ji, Haimin Wang, Chang Liu, and Brian R Dennis. A hard x-ray sigmoidal structure during the initial phase of the 2003 october 29 x10 flare. *The Astrophysical Journal*, 680(1):734–739, 2008.

[63] Thomas Wiegelmann and Takashi Sakurai. Solar force-free magnetic fields. *Living Reviews in Solar Physics*, 18(1):1, 2021.

[64] Haosheng Lin, JR Kuhn, and R Coulter. Coronal magnetic field measurements. *The Astrophysical Journal Letters*, 613(2):L177–L180, 2004.

[65] Haosheng Lin, Matthew J Penn, and Steven Tomczyk. A new precise measurement of the coronal magnetic field strength. *The Astrophysical Journal Letters*, 541(2):L83–L86, 2000.

[66] Valery M Nakariakov and Leon Ofman. Determination of the coronal magnetic field by coronal loop oscillations. *Astronomy & Astrophysics*, 372(3):L53–L56, 2001.

[67] Martin D Altschuler and Gordon Newkirk Jr. Magnetic fields and the structure of the solar corona: I: Methods of calculating coronal fields. *Solar Physics*, 9(1):131–149, 1969.

[68] BC Low and YQ Lou. Modeling solar force-free magnetic fields. *Astrophysical Journal, Part 1 (ISSN 0004-637X), vol. 352, March 20, 1990, p. 343-352.*, 352:343–352, 1990.

[69] JA Slavin, RP Lepping, J Gjerloev, DH Fairfield, M Hesse, CJ Owen, MB Moldwin, T Nagai, A Ieda, and T Mukai. Geotail observations of magnetic flux ropes in the plasma sheet. *Journal of Geophysical Research: Space Physics*, 108(A1):SMP–10, 2003.

[70] JF Drake, M Swisdak, KM Schoeffler, BN Rogers, and S Kobayashi. Formation of secondary islands during magnetic reconnection. *Geophysical research letters*, 33(13), 2006.

[71] Haihong Che and GP Zank. A brief review on particle acceleration in multi-island magnetic reconnection. In *Journal of Physics: Conference Series*, volume 1332, page 012003. IOP Publishing, 2019.

[72] Rongsheng Wang, Quanming Lu, Xing Li, Can Huang, and Shui Wang. Observations of energetic electrons up to 200 kev associated with a secondary island near the center of an ion diffusion region: A cluster case study. *Journal of Geophysical Research: Space Physics*, 115(A11), 2010.

[73] Rongsheng Wang, Quanming Lu, Aimin Du, and Shui Wang. In situ observations of a secondary magnetic island in an ion diffusion region¡? format?¿ and associated energetic electrons. *Physical Review Letters*, 104(17):175003, 2010.

[74] CT Russell and RC Elphic. Initial isee magnetometer results: Magnetopause observations. *Space Science Reviews*, 22(6):681–715, 1978.

[75] G Paschmann, G Haerendel, I Papamastorakis, Nagendra Sckopke, SJ Bame, JT Gosling, and CT Russell. Plasma and magnetic field characteristics of magnetic flux transfer events. *Journal of Geophysical Research: Space Physics*, 87(A4):2159–2168, 1982.

[76] Jean Berchem and CT Russell. Magnetic field rotation through the magnetopause: Isee 1 and 2 observations. *Journal of Geophysical Research: Space Physics*, 87(A10):8139–8148, 1982.

[77] Li-Jen Chen, Naoki Bessho, Bertrand Lefebvre, Hans Vaith, Arne Asnes, Ondrej Santolik, Andrew Fazakerley, Pamela Puhl-Quinn, Amitava Bhattacharjee, Yuri Khotyaintsev, et al. Multispacecraft observations of the electron current sheet, neighboring magnetic islands, and electron acceleration during magnetotail reconnection. *Physics of Plasmas*, 16(5), 2009.

[78] SY Huang, Fouad Sahraoui, Alessandro Retinò, Olivier Le Contel, ZG Yuan, Alexandros Chasapis, Nicolas Aunai, Hugo Breuillard, XH Deng, Meng Zhou, et al. Mms observations of ion-scale magnetic island in the magnetosheath turbulent plasma. *Geophysical Research Letters*, 43(15):7850–7858, 2016.

[79] M Akhavan-Tafti, JA Slavin, G Le, JP Eastwood, RJ Strangeway, CT Russell, R Nakamura, W Baumjohann, RB Torbert, BL Giles, et al. Mms examination of ftes at the earth's subsolar magnetopause. *Journal of Geophysical Research: Space Physics*, 123(2):1224–1241, 2018.

[80] WJ Sun, JA Slavin, AM Tian, SC Bai, GK Poh, M Akhavan-Tafti, San Lu, ST Yao, G Le, R Nakamura, et al. Mms study of the structure of ion-scale flux ropes in the earth's cross-tail current sheet. *Geophysical Research Letters*, 46(12):6168–6177, 2019.

[81] M Zhou, HY Man, XH Deng, Y Pang, Y Khotyaintsev, G Lapenta, YY Yi, ZH Zhong, and WQ Ma. Observations of secondary magnetic reconnection in the turbulent reconnection outflow. *Geophysical Research Letters*, 48(4):e2020GL091215, 2021.

[82] Chaoxu Liu, Xueshang Feng, Fang Shen, Xinhua Zhao, Dingkun Zhong, Jiamei Qin, Liping Yang, Yufen Zhou, Xiaojing Liu, and Changqing Xiang. Mms observations of an active flux rope during asymmetric magnetic reconnection. *Journal of Geophysical Research: Space Physics*, 130(11):e2025JA034540, 2025.

[83] K c Shibata, S Masuda, M Shimojo, H Hara, T Yokoyama, S Tsuneta, T Kosugi, and Yohsuke Ogawara. Hot-plasma ejections associated with compact-loop solar flares. *The Astrophysical Journal Letters*, 451(2):L83–L85, 1995.

[84] Saku Tsuneta. Moving plasmoid and formation of the neutral sheet in a solar flare. *The Astrophysical Journal*, 483(1):507–514, 1997.

[85] Masamitsu Ohyama and Kazunari Shibata. Preflare heating and mass motion in a solar flare associated with hot plasma ejection: 1993 november 11 c9. 7 flare. *Publications of the Astronomical Society of Japan*, 49(2):249–261, 1997.

[86] BC Low. Coronal mass ejections, magnetic flux ropes, and solar magnetism. *Journal of Geophysical Research: Space Physics*, 106(A11):25141–25163, 2001.

[87] J Lin, Y-K Ko, L Sui, JC Raymond, GA Stenborg, Y Jiang, S Zhao, and S Mancuso. Direct observations of the magnetic reconnection site of an eruption on 2003 november 18. *The Astrophysical Journal*, 622(2):1251–1264, 2005.

[88] Jongchul Chae, Kyuhyoun Cho, Ryun-Young Kwon, and Eun-Kyung Lim. Evidence for a magnetic reconnection origin of plasma outflows along post-cme rays. *The Astrophysical Journal*, 841(1):49, 2017.

[89] NR Sheeley Jr, DD-H Lee, KP Casto, Y-M Wang, and NB Rich. The structure of streamer blobs. *The Astrophysical Journal*, 694(2):1471–1480, 2009.

[90] QM Zhang and HS Ji. Blobs in recurring extreme-ultraviolet jets. *Astronomy & Astrophysics*, 567:A11, 2014.

[91] Lei Ni, Qing-Min Zhang, Nicholas A Murphy, and Jun Lin. Blob formation and ejection in coronal jets due to the plasmoid and kelvin–helmholtz instabilities. *The Astrophysical Journal*, 841(1):27, 2017.

[92] Rui Liu. Magnetic flux ropes in the solar corona: structure and evolution toward eruption. *Research in Astronomy and Astrophysics*, 20(10):165, 2020.

[93] L Rouppe van der Voort, B De Pontieu, Göran B Scharmer, J de la Cruz Rodríguez, Juan Martínez-Sykora, Daniel Nóbrega-Siverio, LJ Guo, Shahin Jafarzadeh, TMD Pereira, VH Hansteen, et al. Intermittent reconnection and plasmoids in uv bursts in the low solar atmosphere. *The Astrophysical Journal Letters*, 851(1):L6, 2017.

[94] TD Phan, JF Drake, D Larson, M Oieroset, S Eriksson, Z Yin, B Lavraud, M Swisdak, SD Bale, R Livi, et al. Multiple subscale magnetic reconnection embedded inside a heliospheric current sheet reconnection exhaust: evidence for flux rope merging. *The Astrophysical Journal Letters*, 971(2):L42, 2024.

[95] Manfred Scholer. Magnetic flux transfer at the magnetopause based on single x line bursty reconnection. *Geophysical Research Letters*, 15(4):291–294, 1988.

[96] Manfred Scholer. Strong core magnetic fields in magnetopause flux transfer events. *Geophysical research letters*, 15(8):748–751, 1988.

[97] DJ Southwood, Charlie J Farrugia, and MA Saunders. What are flux transfer events? *Planetary and Space Science*, 36(5):503–508, 1988.

[98] H Karimabadi, D Krauss-Varban, N Omidi, and HX Vu. Magnetic structure of the reconnection layer and core field generation in plasmoids. *Journal of Geophysical Research: Space Physics*, 104(A6):12313–12326, 1999.

[99] ZW Ma, LC Lee, A Otto, and Y Shi. By enhancements in magnetospheric current sheets and magnetic flux tubes. *Physics of Space Plasmas*, page 575, 1992.

[100] ZWT Ma, A Otto, and LC Lee. Core magnetic field enhancement in single x line, multiple x line and patchy reconnection. *Journal of Geophysical Research: Space Physics*, 99(A4):6125–6136, 1994.

[101] Michael Hesse, Joachim Birn, Masha M Kuznetsova, and Jürgen Dreher. A simple model of core field generation during plasmoid evolution. *Journal of Geophysical Research: Space Physics*, 101(A5):10797–10804, 1996.

[102] Shu-Ping Jin and Hong-Ang Yang. The core field enhancement caused by pressure loss in the flux rope structures in the magnetotail. *Chinese Journal of Geophysics*, 47(2):218–226, 2004.

[103] Erich S Weibel. Spontaneously growing transverse waves in a plasma due to an anisotropic velocity distribution. *Physical Review Letters*, 2(3):83, 1959.

[104] Peter H Yoon and Ronald C Davidson. Exact analytical model of the classical weibel instability in a relativistic anisotropic plasma. *Physical Review A*, 35(6):2718, 1987.

[105] Peter H Yoon. Relativistic weibel instability. *Physics of Plasmas*, 14(2):024504, 2007.

[106] Brian Allen, V Yakimenko, M Babzien, M Fedurin, Karl Kusche, and P Muggli. Experimental study of current filamentation instability. *Physical review letters*, 109(18):185007, 2012.

[107] CM Huntington, F Fiuza, JS Ross, AB Zylstra, RP Drake, DH Froula, G Gregori, NL Kugland, CC Kuranz, MC Levy, et al. Observation of magnetic field generation via the weibel instability in interpenetrating plasma flows. *Nature Physics*, 11(2):173–176, 2015.

[108] RL Morse and CW Nielson. Numerical simulation of the weibel instability in one and two dimensions. *The Physics of Fluids*, 14(4):830–840, 1971.

[109] Ricardo A Fonseca, Luıs O Silva, John W Tonge, Warren B Mori, and John M Dawson. Three-dimensional weibel instability in astrophysical scenarios. *Physics of Plasmas*, 10(5):1979–1984, 2003.

[110] Reinhard Schlickeiser and Padma Kant Shukla. Cosmological magnetic field generation by the weibel instability. *The Astrophysical Journal*, 599(2):L57, 2003.

[111] Tan Weihan and Gu Min. Thermal flux limitation and thermal conduction inhibition in laser plasma. *Laser and Particle Beams*, 3(3):243–250, 1985.

[112] Amir Levinson and David Eichler. Inhibition of electron thermal conduction by electromagnetic instabilities. *The Astrophysical Journal*, 387:212–218, 1992.

[113] San Lu, Quanming Lu, Xi Shao, Peter H Yoon, and Shui Wang. Weibel instability and structures of magnetic island in anti-parallel collisionless magnetic reconnection. *Physics of Plasmas*, 18(7), 2011.

[114] W Baumjohann, R Nakamura, and RA Treumann. Magnetic guide field generation in collisionless current sheets. *Annales Geophysicae*, 28(3):789–793, 2010.

[115] Yi-Hsin Liu, Marc Swisdak, and James F Drake. The weibel instability inside the electron-positron harris sheet. *Physics of Plasmas*, 16(4), 2009.

[116] Seiji Zenitani and Michael Hesse. The role of the weibel instability at the reconnection jet front in relativistic pair plasma reconnection. *Physics of Plasmas*, 15(2), 2008.

[117] Akira Miura and PL Pritchett. Nonlocal stability analysis of the mhd kelvin-helmholtz instability in a compressible plasma. *Journal of Geophysical Research: Space Physics*, 87(A9):7431–7444, 1982.

[118] Jay R Johnson, Simon Wing, and Peter A Delamere. Kelvin helmholtz instability in planetary magnetospheres. *Space Science Reviews*, 184(1):1–31, 2014.

[119] H Hasegawa, M Fujimoto, T-D Phan, H Reme, A Balogh, MW Dunlop, C Hashimoto, and R TanDokoro. Transport of solar wind into earth's magnetosphere through rolled-up kelvin–helmholtz vortices. *Nature*, 430(7001):755–758, 2004.

[120] RL Fermo, JF Drake, and M Swisdak. Secondary magnetic islands generated by the kelvin-helmholtz instability¡? format?¿ in a reconnecting current sheet. *Physical review letters*, 108(25):255005, 2012.

[121] ZH Zhong, RX Tang, M Zhou, XH Deng, Y Pang, WR Paterson, BL Giles, JL Burch, RB Tobert, RE Ergun, et al. Evidence for secondary flux rope generated by the electron kelvin-helmholtz instability in a magnetic reconnection diffusion region. *Physical Review Letters*, 120(7):075101, 2018.

[122] Can Huang, Quanming Lu, Fan Guo, Mingyu Wu, Aimin Du, and Shui Wang. Magnetic islands formed due to the kelvin-helmholtz instability in the outflow region of collisionless magnetic reconnection. *Geophysical Research Letters*, 42(18):7282–7286, 2015.

[123] John C Brown. The deduction of energy spectra of non-thermal electrons in flares from the observed dynamic spectra of hard x-ray bursts. *Solar Physics*, 18(3):489–502, 1971.

[124] John C Brown. The directivity and polarisation of thick target x-ray bremsstrahlung from solar flares. *Solar Physics*, 26(2):441–459, 1972.

[125] Gordon D Holman, Markus J Aschwanden, Henry Aurass, Marina Battaglia, Paolo C Grigis, Eduard P Kontar, Wei Liu, Pascal Saint-Hilaire, and Valentina V Zharkova. Implications of x-ray observations for electron acceleration and propagation in solar flares. *Space science reviews*, 159(1):107, 2011.

[126] S Krucker, M Battaglia, PJ Cargill, L Fletcher, HS Hudson, AL MacKinnon, S Masuda, L Sui, M Tomczak, AL Veronig, et al. Hard x-ray emission from the solar corona. *The Astronomy and Astrophysics Review*, 16(3):155–208, 2008.

[127] Jingnan Guo, A Gordon Emslie, Anna Maria Massone, and Michele Piana. Properties of the acceleration regions in several loop-structured solar flares. *The Astrophysical Journal*, 755(1):32, 2012.

[128] Paulo JA Simões and Eduard P Kontar. Implications for electron acceleration and transport from non-thermal electron rates at looptop and footpoint sources in solar flares. *Astronomy & Astrophysics*, 551:A135, 2013.

[129] Gregory D Fleishman, Gelu M Nita, Bin Chen, Sijie Yu, and Dale E Gary. Solar flare accelerates nearly all electrons in a large coronal volume. *Nature*, pages 1–4, 2022.

[130] Vahé Petrosian, Timothy Q Donaghy, and James M McTiernan. Loop top hard x-ray emission in solar flares: images and statistics. *The Astrophysical Journal*, 569(1):459, 2002.

[131] R. P. Lin, S. Krucker, G. J. Hurford, D. M. Smith, H. S. Hudson, G. D. Holman, R. A. Schwartz, B. R. Dennis, G. H. Share, R. J. Murphy, A. G. Emslie, C. Johns-Krull, and N. Vilmer. Rhessi observations of particle acceleration and energy release in an intense solar gamma-ray line flare. *The Astrophysical Journal*, 595(2):L69, sep 2003.

[132] Säm Krucker, S. M. White, and R. P. Lin. Solar flare hard x-ray emission from the high corona. *The Astrophysical Journal*, 669(1):L49, oct 2007.

[133] Säm Krucker, H. S. Hudson, L. Glesener, S. M. White, S. Masuda, J.-P. Wuelser, and R. P. Lin. Measurements of the coronal acceleration region of a solar flare. *The Astrophysical Journal*, 714(2):1108, apr 2010.

[134] RP c Lin, Sam Krucker, Gordon J Hurford, DM Smith, HS Hudson, GD Holman, RA Schwartz, BR Dennis, GH Share, RJ Murphy, et al. Rhessi observations of particle acceleration and energy release in an intense solar gamma-ray line flare. *The Astrophysical Journal*, 595(2):L69, 2003.

[135] SÄM Krucker, SM White, and RP Lin. Solar flare hard x-ray emission from the high corona. *The Astrophysical Journal*, 669(1):L49, 2007.

[136] Brian R Dennis. Solar flare hard x-ray observations. *Solar physics*, 118(1):49–94, 1988.

[137] Satoshi Masuda, Takeo Kosugi, Hirohisa Hara, Taro Sakao, Kazunari Shibata, and Saku Tsuneta. Hard x-ray sources and the primary energy-release site in solar flares. *Publications of the Astronomical Society of Japan*, 47(5):677–689, 1995.

[138] CE Alissandrakis. Gyrosynchrotron emission of solar flares: Invited review. *Solar Physics*, 104(1):207–221, 1986.

[139] Mukul R Kundu, VV Grechnev, SM White, EJ Schmahl, NS Meshalkina, and LK Kashapova. High-energy emission from a solar flare in hard x-rays and microwaves. *Solar Physics*, 260(1):135–156, 2009.

[140] Alexey A Kuznetsov and Valentina V Zharkova. Manifestations of energetic electrons with anisotropic distributions in solar flares. ii. gyrosynchrotron microwave emission. *The Astrophysical Journal*, 722(2):1577–1588, 2010.

[141] VF Melnikov, K Shibasaki, and VE Reznikova. Loop-top nonthermal microwave source in extended solar flaring loops. *The Astrophysical Journal Letters*, 580(2):L185–L188, 2002.

[142] Dale E Gary, Bin Chen, Brian R Dennis, Gregory D Fleishman, Gordon J Hurford, Säm Krucker, James M McTiernan, Gelu M Nita, Albert Y Shih, Stephen M White, et al. Microwave and hard x-ray observations of the 2017 september 10 solar limb flare. *The Astrophysical Journal*, 863(1):83, 2018.

[143] LV Filatov and VF Melnikov. Microwave emission of a flare loop in the presence of whistler turbulence. *Geomagnetism and Aeronomy*, 60(8):1137–1145, 2020.

[144] Zhao Wu, Alexey Kuznetsov, Sergey Anfinogentov, Victor Melnikov, Robert Sych, Bing Wang, Ruisheng Zheng, Xiangliang Kong, Baolin Tan, Zongjun Ning, et al. A multipeak solar flare with a high turnover frequency of the gyrosynchrotron spectra from the loop-top source. *The Astrophysical Journal*, 968(1):5, 2024.

[145] Allen S Krieger. The decay of coronal loops brightened by flares and transients. *Solar Physics*, 56(1):107–120, 1978.

[146] R Moore, DL McKenzie, Z Svestka, KG Widing, KP Dere, SK Antiochos, HW Dodson-Prince, E Hiei, KR Krall, and AS Krieger. The thermal x-ray flare plasma. In *Skylab Solar Workshop II*, pages 341–409, 1980.

[147] Lyman Spitzer. *Physics of fully ionized gases*. Courier Corporation, 2006.

[148] S Kołomański, Tomasz Mrozek, and U Bak-Stślicka. Rhessi observations of long-duration flares with long-lasting x-ray loop-top sources. *Astronomy & Astrophysics*, 531:A57, 2011.

[149] Nicolas H Bian, Jonathan M Watters, Eduard P Kontar, and A Gordon Emslie. Anomalous cooling of coronal loops with turbulent suppression of thermal conduction. *The Astrophysical Journal*, 833(1):76, 2016.

[150] Daniel F Ryan, Phillip C Chamberlin, Ryan O Milligan, and Peter T Gallagher. Decay-phase cooling and inferred heating of m-and x-class solar flares. *The Astrophysical Journal*, 778(1):68, 2013.

[151] Peter J Cargill, John T Mariska, and Spiro K Antiochos. Cooling of solar flares plasmas. 1: Theoretical considerations. *The Astrophysical Journal, Part 1 (ISSN 0004-637X), vol. 439, no. 2, p. 1034-1043*, 439:1034–1043, 1995.

[152] Suguru Kamio, Hiroki Kurokawa, and Takako T Ishii. Precise determination of cooling times of post-flare loops from the detailed comparison between hα and soft x-ray images. *Solar Physics*, 215(1):127–146, 2003.

[153] Saku Tsuneta, Satoshi Masuda, Takeo Kosugi, and Jun Sato. Hot and superhot plasmas above an impulsive flare loop. *The Astrophysical Journal*, 478(2):787–798, 1997.

[154] Saku Tsuneta and Tsuguya Naito. Fermi acceleration at the fast shock in a solar flare and the impulsive loop-top hard x-ray source. *The Astrophysical Journal Letters*, 495(1):L67–L70, 1998.

[155] Dana Longcope, Jiong Qiu, and Jasmine Brewer. A reconnection-driven model of the hard x-ray loop-top source from flare 2004 february 26. *The Astrophysical Journal*, 833(2):211, 2016.

[156] Xiangliang Kong, Fan Guo, Chengcai Shen, Bin Chen, Yao Chen, Sophie Musset, Lindsay Glesener, Peera Pongkitiwanichakul, and Joe Giacalone. The acceleration and confinement of energetic electrons by a termination shock in a magnetic trap: an explanation for nonthermal loop-top sources during solar flares. *The Astrophysical Journal Letters*, 887(2):L37, 2019.

[157] TC Li, JF Drake, and M Swisdak. Suppression of energetic electron transport in flares by double layers. *The Astrophysical Journal*, 757(1):20, 2012.

[158] Tak Chu Li, James F Drake, and Marc Swisdak. Coronal electron confinement by double layers. *The Astrophysical Journal*, 778(2):144, 2013.

[159] TC Li, JF Drake, and M Swisdak. Dynamics of double layers, ion acceleration, and heat flux suppression during solar flares. *The Astrophysical Journal*, 793(1):7, 2014.

[160] PA Bespalov, VV Zaitsev, and AV Stepanov. On the origin of time delays in hard x-ray and gamma-ray emission of solar flares. *Solar physics*, 114:127–140, 1988.

[161] Eduard P Kontar, Nicolas H Bian, A Gordon Emslie, and Nicole Vilmer. Turbulent pitch-angle scattering and diffusive transport of hard x-ray-producing electrons in flaring coronal loops. *The Astrophysical Journal*, 780(2):176, 2013.

[162] Nicolas Bian, A Gordon Emslie, Duncan Horne, and Eduard P Kontar. Heating and cooling of coronal loops with turbulent suppression of parallel heat conduction. *The Astrophysical Journal*, 852(2):127, 2018.

[163] Alex Lazarian. Enhancement and suppression of heat transfer by mhd turbulence. *The Astrophysical Journal Letters*, 645(1):L25–L28, 2006.

[164] Alex Lazarian, G Eyink, E Vishniac, and Grzegorz Kowal. Turbulent reconnection and its implications. *Philosophical Transactions of the Royal Society A: Mathematical, Physical and Engineering Sciences*, 373(2041), 2015.

[165] Charles F Kennel and HE Petschek. Limit on stably trapped particle fluxes. *Journal of Geophysical Research*, 71(1):1–28, 1966.

[166] Yuri V Khotyaintsev, Daniel B Graham, Cecilia Norgren, and Andris Vaivads. Collisionless magnetic reconnection and waves: Progress review. *Frontiers in Astronomy and Space Sciences*, 6:70, 2019.

[167] Hanqing Ma, James F Drake, and Marc Swisdak. Wave generation and energetic electron scattering in solar flares. *The Astrophysical Journal*, 954(1):21, 2023.

[168] Daniel B Graham, G Cozzani, Yu V Khotyaintsev, VD Wilder, Justin Craig Holmes, TKM Nakamura, J Büchner, K Dokgo, Louis Richard, K Steinvall, et al. The role of kinetic instabilities and waves in collisionless magnetic reconnection. *Space Science Reviews*, 221(1):20, 2025.

[169] Gareth Talbot Roberg-Clark, JF Drake, CS Reynolds, and M Swisdak. Suppression of electron thermal conduction in the high β intracluster medium of galaxy clusters. *The Astrophysical Journal Letters*, 830(1):L9, 2016.

[170] GT Roberg-Clark, JF Drake, CS Reynolds, and M Swisdak. Suppression of electron thermal conduction by whistler turbulence in a sustained thermal gradient. *Physical Review Letters*, 120(3):035101, 2018.

[171] GT Roberg-Clark, James Frederick Drake, Michael Swisdak, and CS Reynolds. Wave generation and heat flux suppression in astrophysical plasma systems. *The Astrophysical Journal*, 867(2):154, 2018.

[172] GT Roberg-Clark, Oleksiy Agapitov, James F Drake, and Marc Swisdak. Scattering of energetic electrons by heat-flux-driven whistlers in flares. *The Astrophysical Journal*, 887(2):190, 2019.

[173] S Peter Gary. *Theory of space plasma microinstabilities*. Number 7. Cambridge university press, 1993.

[174] Robert A Helliwell. *Whistlers and related ionospheric phenomena*. Courier Corporation, 2014.

[175] GP Chernov. Whistlers in the solar corona and their relevance to fine structures of type iv radio emission. *Solar physics*, 130:75–82, 1990.

[176] XH Deng and H Matsumoto. Rapid magnetic reconnection in the earth's magnetosphere mediated by whistler waves. *Nature*, 410(6828):557–560, 2001.

[177] Catherine Lacombe, Olga Alexandrova, Lorenzo Matteini, Ondrej Santolík, Nicole Cornilleau-Wehrlin, Anne Mangeney, Yvonne de Conchy, and Milan Maksimovic. Whistler mode waves and the electron heat flux in the solar wind: Cluster observations. *The Astrophysical Journal*, 796(1):5, 2014.

[178] Yuguang Tong, Ivan Y Vasko, Anton V Artemyev, Stuart D Bale, and Forrest S Mozer. Statistical study of whistler waves in the solar wind at 1 au. *The Astrophysical Journal*, 878(1):41, 2019.

[179] JF Drake, C Pfrommer, CS Reynolds, M Ruszkowski, M Swisdak, A Einarsson, T Thomas, AB Hassam, and GT Roberg-Clark. Whistler-regulated magnetohydrodynamics: transport equations for electron thermal conduction in the high-β intracluster medium of galaxy clusters. *The Astrophysical Journal*, 923(2):245, 2021.

[180] S Peter Gary and WC Feldman. Solar wind heat flux regulation by the whistler instability. *Journal of Geophysical Research*, 82(7):1087–1094, 1977.

[181] H Karimabadi, D Krauss-Varban, and T Terasawa. Physics of pitch angle scattering and velocity diffusion, 1. theory. *Journal of Geophysical Research: Space Physics*, 97(A9):13853–13864, 1992.

[182] W Li, D Mourenas, AV Artemyev, OV Agapitov, J Bortnik, JM Albert, RM Thorne, B Ni, CA Kletzing, WS Kurth, et al. Evidence of stronger pitch angle scattering loss caused by oblique whistler-mode waves as compared with quasi-parallel waves. *Geophysical Research Letters*, 41(17):6063–6070, 2014.

[183] S Komarov, AA Schekochihin, E Churazov, and Anatoly Spitkovsky. Self-inhibiting thermal conduction in a high-, whistler-unstable plasma. *Journal of Plasma Physics*, 84(3):905840305, 2018.

[184] N Kitamura, T Amano, Y Omura, SA Boardsen, DJ Gershman, Y Miyoshi, M Kitahara, Y Katoh, H Kojima, S Nakamura, et al. Direct observations of energy transfer from resonant electrons to whistler-mode waves in magnetosheath of earth. *Nature Communications*, 13(1):6259, 2022.

[185] Nicholas A Krall and Alvin W Trivelpiece. Principles of plasma physics. *American Journal of Physics*, 41(12):1380–1381, 1973.

[186] Daniel Verscharen, Benjamin DG Chandran, Seong-Yeop Jeong, Chadi S Salem, Marc P Pulupa, and Stuart D Bale. Self-induced scattering of strahl electrons in the solar wind. *The Astrophysical Journal*, 886(2):136, 2019.

[187] Tien Vo. Utilizing the hamiltonian dynamics to study resonant interactions of whistler-mode waves and electrons in the solar wind. *arXiv preprint arXiv:2105.02265*, 2021.

[188] C Krafft, A Volokitin, and A Zaslavsky. Saturation of the fan instability: Nonlinear merging of resonances. *Physics of plasmas*, 12(11), 2005.

[189] Tien Vo, Robert Lysak, and Cynthia Cattell. Stochastic diffusion of electrons interacting with whistler-mode waves in the solar wind. *Physics of Plasmas*, 29(1):012904, 2022.

[190] Evan L Yerger, Matthew W Kunz, Archie FA Bott, and Anatoly Spitkovsky. Collisionless conduction in a high-beta plasma: a collision operator for whistler turbulence. *arXiv preprint arXiv:2405.06481*, 2024.

[191] Milan Maksimovic, I Zouganelis, J-Y Chaufray, K Issautier, EE Scime, JE Littleton, Eckart Marsch, DJ McComas, C Salem, RP Lin, et al. Radial evolution of the electron distribution functions in the fast solar wind between 0.3 and 1.5 au. *Journal of Geophysical Research: Space Physics*, 110(A9), 2005.

[192] GA Graham, IJ Rae, CJ Owen, AP Walsh, CS Arridge, L Gilbert, GR Lewis, GH Jones, C Forsyth, AJ Coates, et al. The evolution of solar wind strahl with heliospheric distance. *Journal of Geophysical Research: Space Physics*, 122(4):3858–3874, 2017.

[193] Štěpán Štverák, Milan Maksimovic, Pavel M Trávníček, Eckart Marsch, Andrew N Fazakerley, and Earl E Scime. Radial evolution of nonthermal electron populations in the low-latitude solar wind: Helios, cluster, and ulysses observations. *Journal of Geophysical Research: Space Physics*, 114(A5), 2009.

[194] Seong-Yeop Jeong, Joel B Abraham, Daniel Verscharen, Laura Berčič, David Stansby, Georgios Nicolaou, Christopher J Owen, Robert T Wicks, Andrew N Fazakerley, Jeffersson A Agudelo Rueda, et al. The stability of the electron strahl against the oblique fast-magnetosonic/whistler instability in the inner heliosphere. *The Astrophysical Journal Letters*, 926(2):L26, 2022.

[195] Joel B Abraham, Christopher J Owen, Daniel Verscharen, Mayur Bakrania, David Stansby, Robert T Wicks, Georgios Nicolaou, Phyllis L Whittlesey, Jeffersson A Agudelo Rueda, Seong-Yeop Jeong, et al. Radial evolution of thermal and suprathermal electron populations in the slow solar wind from 0.13 to 0.5 au: Parker solar probe observations. *The Astrophysical Journal*, 931(2):118, 2022.

[196] Konstantinos Horaites and Stanislav Boldyrev. The heliospheric ambipolar potential inferred from sunward-propagating halo electrons. *Monthly Notices of the Royal Astronomical Society*, 515(4):5135–5144, 2022.

[197] Alfredo Micera, Andrei Zhukov, Rodrigo Alvaro Lopez, Elisabetta Boella, Miaria Elena Innocenti, Marian Lazar, and Giovanni Lapenta. Particle-in-cell simulations of the oblique whistler heat flux instability. scattering of the strahl electrons into the halo and heat flux regulation in the solar wind near the sun. In *APS Division of Plasma Physics Meeting Abstracts*, volume 2020, pages TO16–010, 2020.

[198] IY Vasko, Vladimir Krasnoselskikh, Y Tong, SD Bale, JW Bonnell, and FS Mozer. Whistler fan instability driven by strahl electrons in the solar wind. *The Astrophysical Journal Letters*, 871(2):L29, 2019.

[199] BB Kadomtsev and OP Pogutse. Electric conductivity of a plasma in a strong magnetic field. *Sov. Phys. JETP*, 26:1146, 1968.

[200] VV Parail and OP Pogutse. The kinetic theory of runaway electron beam instability in a tokamak. *Nuclear Fusion*, 18(3):303, 1978.

[201] CF Kennel and F Engelmann. Velocity space diffusion from weak plasma turbulence in a magnetic field. *Physics of Fluids*, 9(12):2377, 1966.

[202] Jo R Jokipii. Cosmic-ray propagation. i. charged particles in a random magnetic field. *Astrophysical Journal, vol. 146, p. 480*, 146:480, 1966.

[203] Andreas Shalchi, John William Bieber, William H Matthaeus, and Gang Qin. Nonlinear parallel and perpendicular diffusion of charged cosmic rays in weak turbulence. *The Astrophysical Journal*, 616(1):617–629, 2004.

[204] Frank C Jones, Thomas J Birmingham, and Thomas B Kaiser. Partially averaged field approach to cosmic ray diffusion. *The Physics of Fluids*, 21(3):347–360, 1978.

[205] Melvyn L Goldstein. A nonlinear theory of cosmic ray pitch angle diffusion in homogeneous magnetostatic turbulence. Technical report, 1975.

[206] Takasuke Sakai and Masahito Kato. Pitch-angle-scattering diffusion coefficient for particles with pitch angle near 90 in simulated magnetic field fluctuations. *Journal of geomagnetism and geoelectricity*, 36(1):33–44, 1984.

[207] Gian Marco Felice and RM Kulsrud. Cosmic-ray pitch-angle scattering through 90. *The Astrophysical Journal*, 553(1):198, 2001.

[208] Mitsuo Oka, Fumiko Otsuka, Shuichi Matsukiyo, Lynn B Wilson, MR Argall, Takanobu Amano, TD Phan, M Hoshino, Olivier Le Contel, Daniel J Gershman, et al. Electron scattering by low-frequency whistler waves at earth's bow shock. *The Astrophysical Journal*, 886(1):53, 2019.

[209] KR Lorentzen, MP McCarthy, GK Parks, JE Foat, RM Millan, DM Smith, RP Lin, and JP Treilhou. Precipitation of relativistic electrons by interaction with electromagnetic ion cyclotron waves. *Journal of Geophysical Research: Space Physics*, 105(A3):5381–5389, 2000.

[210] Craig J Rodger, Tero Raita, Mark A Clilverd, Annika Seppälä, Sarah Dietrich, Neil R Thomson, and Thomas Ulich. Observations of relativistic electron precipitation from the radiation belts driven by emic waves. *Geophysical Research Letters*, 35(16), 2008.

[211] Y Miyoshi, K Sakaguchi, K Shiokawa, D Evans, J Albert, M Connors, and Vhttps Jordanova. Precipitation of radiation belt electrons by emic waves, observed from ground and space. *Geophysical Research Letters*, 35(23), 2008.

[212] Xin An, Anton Artemyev, Vassilis Angelopoulos, Xiaojia Zhang, Didier Mourenas, and Jacob Bortnik. Nonresonant scattering of relativistic electrons by electromagnetic ion cyclotron waves in earth's radiation belts. *Physical Review Letters*, 129(13):135101, 2022.

[213] Dae-Young Lee, Kyung-Chan Kim, and Cheong-Rim Choi. Nonlinear scattering of 90 pitch angle electrons in the outer radiation belt by large-amplitude emic waves. *Geophysical Research Letters*, 47(4):e2019GL086738, 2020.

[214] Charles K Birdsall. Particle-in-cell charged-particle simulations, plus monte carlo collisions with neutral atoms, pic-mcc. *IEEE Transactions on plasma science*, 19(2):65–85, 2002.

[215] John P Verboncoeur. Particle simulation of plasmas: review and advances. *Plasma Physics and Controlled Fusion*, 47(5A):A231–A260, 2005.

[216] Tony D Arber, Keith Bennett, Christopher S Brady, Alistair Lawrence-Douglas, MG Ramsay, Nathan John Sircombe, Paddy Gillies, Roger G Evans, Holger Schmitz, Anthony R Bell, et al. Contemporary particle-in-cell approach to laser-plasma modelling. *Plasma Physics and Controlled Fusion*, 57(11):113001, 2015.

[217] Roger W Hockney and James W Eastwood. *Computer simulation using particles*. crc Press, 2021.

[218] A Zeiler, D Biskamp, JF Drake, BN Rogers, MA Shay, and M Scholer. Three-dimensional particle simulations of collisionless magnetic reconnection. *Journal of Geophysical Research: Space Physics*, 107(A9):SMP–6, 2002.

[219] RM Kulsrud. Mhd description of plasma: Handbook of plasma physics. Technical report, Princeton Univ., NJ (USA). Plasma Physics Lab., 1980.

[220] Johan P Goedbloed, Rony Keppens, and Stefaan Poedts. *Advanced magnetohydrodynamics: with applications to laboratory and astrophysical plasmas*. Cambridge University Press, 2010.

[221] David I Pontin and Eric R Priest. Magnetic reconnection: Mhd theory and modelling. *Living Reviews in Solar Physics*, 19(1):1, 2022.

[222] Hanqing Ma, JF Drake, and M Swisdak. Whistler wave scattering of energetic electrons past 90°. *Physics of Plasmas*, 31(10), 2024.

[223] Hanqing Ma, JF Drake, and M Swisdak. The self-generation of core fields and electron scattering in flux ropes during magnetic reconnection. *The Astrophysical Journal*, 1003(2):139, 2026.

[224] W-L Teh, M Abdullah, and AM Hasbi. Evidence for the core field polarity of magnetic flux ropes against the reconnection guide field. *Journal of Geophysical Research: Space Physics*, 119(11):8979–8983, 2014.

[225] Burton D Fried. On the mechanism for instability of transverse plasma waves. Technical report, 1959.

[226] EP Alves, Thomas Grismayer, SF Martins, F Fiúza, RA Fonseca, and LO Silva. Large-scale magnetic field generation via the kinetic kelvin–helmholtz instability in unmagnetized scenarios. *The Astrophysical Journal Letters*, 746(2):L14, 2012.

[227] E P Alves, Thomas Grismayer, R A Fonseca, and L O Silva. Electron-scale shear instabilities: Magnetic field generation and particle acceleration in astrophysical jets. *New Journal of Physics*, 16(3):035007, 2014.

[228] K-I Nishikawa, P Hardee, B Zhang, I Duţan, M Medvedev, Eun Jin Choi, KyoungWook Min, J Niemiec, Y Mizuno, Ake Nordlund, et al. Magnetic field generation in a jet-sheath plasma via the kinetic kelvin-helmholtz instability. In *Annales Geophysicae*, volume 31, pages 1535–1541. Copernicus Publications Göttingen, Germany, 2013.

[229] K-I Nishikawa, PE Hardee, I Duţan, J Niemiec, M Medvedev, Y Mizuno, Athina Meli, H Sol, B Zhang, M Pohl, et al. Magnetic field generation in core-sheath jets via the kinetic kelvin–helmholtz instability. *The Astrophysical Journal*, 793(1):60, 2014.

[230] RL Morse and CW Nielson. Numerical simulation of the weibel instability in one and two dimensions. Technical report, Los Alamos Scientific Lab., N. Mex., 1969.

[231] Anne Stockem, Mark Eric Dieckmann, and Reinhard Schlickeiser. Pic simulations of the thermal anisotropy-driven weibel instability: field growth and phase space evolution upon saturation. *Plasma Physics and Controlled Fusion*, 51(7):075014, 2009.

[232] JF Drake, M Swisdak, and R Fermo. The power-law spectra of energetic particles during multi-island magnetic reconnection. *The Astrophysical Journal Letters*, 763(1):L5, 2012.

[233] Meng Zhou, Ye Pang, Xiaohua Deng, Shiyong Huang, and Xiangsheng Lai. Plasma physics of magnetic island coalescence during magnetic reconnection. *Journal of Geophysical Research: Space Physics*, 119(8):6177–6189, 2014.

[234] JD Huba. Hall magnetic reconnection: Guide field dependence. *Physics of plasmas*, 12(1), 2005.

[235] Weigang Wan, Giovanni Lapenta, Gian Luca Delzanno, and Jan Egedal. Electron acceleration during guide field magnetic reconnection. *Physics of Plasmas*, 15(3), 2008.

[236] JT Dahlin, JF Drake, and M Swisdak. Electron acceleration in three-dimensional magnetic reconnection with a guide field. *Physics of Plasmas*, 22(10), 2015.

[237] M Oka, M Fujimoto, I Shinohara, and TD Phan. "island surfing" mechanism of electron acceleration during magnetic reconnection. *Journal of Geophysical Research: Space Physics*, 115(A8), 2010.

[238] Zhiyu Yin, Harry Arnold, James F Drake, and Marc Swisdak. The maximum particle energy gain during magnetic reconnection. *The Astrophysical Journal Letters*, 998(1):L12, 2026.

[239] Mark B Moldwin and W Jeffrey Hughes. Observations of earthward and tailward propagating flux rope plasmoids: Expanding the plasmoid model of geomagnetic substorms. *Journal of Geophysical Research: Space Physics*, 99(A1):183–198, 1994.

[240] SA Kiehas, V Angelopoulos, A Runov, MB Moldwin, and C Möstl. On the formation of tilted flux ropes in the earth's magnetotail observed with artemis. *Journal of Geophysical Research: Space Physics*, 117(A5), 2012.

[241] TD Phan, Jonathan P Eastwood, MA Shay, JF Drake, BU Ö Sonnerup, Masaki Fujimoto, PA Cassak, M Øieroset, JL Burch, RB Torbert, et al. Electron magnetic reconnection without ion coupling in earth's turbulent magnetosheath. *Nature*, 557(7704):202–206, 2018.

[242] RB Torbert, JL Burch, TD Phan, M Hesse, MR Argall, J Shuster, RE Ergun, Love Alm, R Nakamura, KJ Genestreti, et al. Electron-scale dynamics of the diffusion region during symmetric magnetic reconnection in space. *Science*, 362(6421):1391–1395, 2018.

[243] M Hubbert, CT Russell, Yi Qi, S Lu, JL Burch, BL Giles, and TE Moore. Electron-only reconnection as a transition phase from quiet magnetotail current sheets to traditional magnetotail reconnection. *Journal of Geophysical Research: Space Physics*, 127(3):e2021JA029584, 2022.

[244] S Peter Gary and Hui Li. Whistler heat flux instability at high beta. *The Astrophysical Journal*, 529(2):1131, 2000.

[245] Ivan Y Vasko, Ilya V Kuzichev, Anton V Artemyev, Stuart D Bale, John W Bonnell, and Forrest S Mozer. On quasi-parallel whistler waves in the solar wind. *Physics of Plasmas*, 27(8):082902, 2020.

[246] JT Dahlin, JF Drake, and M Swisdak. The role of three-dimensional transport in driving enhanced electron acceleration during magnetic reconnection. *Physics of Plasmas*, 24(9), 2017.

[247] AG Emslie, H Kucharek, BR Dennis, N Gopalswamy, GD Holman, GH Share, A Vourlidas, TG Forbes, PT Gallagher, GM Mason, et al. Energy partition in two solar flare/cme events. *Journal of Geophysical Research: Space Physics*, 109(A10), 2004.

[248] S Peter Gary, Lin Yin, and Dan Winske. Electromagnetic proton cyclotron anisotropy instability: Wave-particle scattering rate. *Geophysical research letters*, 27(16):2457–2459, 2000.

[249] S Hamasaki and NA Krall. Relaxation of anisotropic collisionless plasma. *The Physics of Fluids*, 16(1):145–149, 1973.

[250] Kazumi Nishimura, S Peter Gary, and Hui Li. Whistler anisotropy instability: Wave-particle scattering rate. *Journal of Geophysical Research: Space Physics*, 107(A11):SMP–18, 2002.

[251] GS Bisnovatyi-Kogan and AA Ruzmaikin. The accretion of matter by a collapsing star in the presence of a magnetic field. ii. selfconsistent stationary picture. *Astrophysics and Space Science*, 42:401–424, 1976.

[252] EPT Liang and Richard H Price. Accretion disk coronae and cygnus x-1. *The Astrophysical Journal*, 218:247–252, 1977.

[253] Dmitri A Uzdensky and Jeremy Goodman. Statistical description of a magnetized corona above a turbulent accretion disk. *The Astrophysical Journal*, 682(1):608, 2008.

[254] Stanislav Boldyrev and Konstantinos Horaites. Kinetic theory of the electron strahl in the solar wind. *Monthly Notices of the Royal Astronomical Society*, 489(3):3412–3419, 2019.

[255] P Kajdič, O Alexandrova, M Maksimovic, C Lacombe, and AN Fazakerley. Suprathermal electron strahl widths in the presence of narrow-band whistler waves in the solar wind. *The Astrophysical Journal*, 833(2):172, 2016.

[256] Aaron Breneman, C Cattell, S Schreiner, K Kersten, LB Wilson III, P Kellogg, K Goetz, and LK Jian. Observations of large-amplitude, narrowband whistlers at stream interaction regions. *Journal of Geophysical Research: Space Physics*, 115(A8), 2010.

[257] CA Cattell, B Short, AW Breneman, and P Grul. Narrowband large amplitude whistler-mode waves in the solar wind and their association with electrons: Stereo waveform capture observations. *The Astrophysical Journal*, 897(2):126, 2020.

[258] PJ Kellogg, CA Cattell, K Goetz, SJ Monson, and LB Wilson III. Large amplitude whistlers in the magnetosphere observed with wind-waves. *Journal of Geophysical Research: Space Physics*, 116(A9), 2011.

[259] SY Huang, HS Fu, ZG Yuan, Andris Vaivads, Yuri V Khotyaintsev, Alessandro Retino, M Zhou, Daniel B Graham, K Fujimoto, Fouad Sahraoui, et al. Two types of whistler waves in the hall reconnection region. *Journal of Geophysical Research: Space Physics*, 121(7):6639–6646, 2016.

[260] Qile Zhang, Fan Guo, William Daughton, Hui Li, and Xiaocan Li. Efficient nonthermal ion and electron acceleration enabled by the flux-rope kink instability in 3d nonrelativistic magnetic reconnection. *Physical Review Letters*, 127(18):185101, 2021.

[261] Jong Yoon Park, June Young Kim, Seongcheol Kim, EC Jung, and YS Hwang. Identification of kink instability in 3d helical flux ropes at vest. *Physics of Plasmas*, 29(5), 2022.

[262] T Török and Bernhard Kliem. Confined and ejective eruptions of kink-unstable flux ropes. *The Astrophysical Journal Letters*, 630(1):L97–L100, 2005.

[263] E Oz, CE Myers, M Yamada, H Ji, RM Kulsrud, and J Xie. Experimental verification of the kruskal-shafranov stability limit in line-tied partial-toroidal plasmas. *Physics of Plasmas*, 18(10), 2011.